Optical Sensors Based on Dedicated Diffractive Optical Elements

Kitchen, Steven Richard

Publication date:
2003

Document Version
Publisher's PDF, also known as Version of record

Ph.D. Thesis

Optical Sensors Based on Dedicated Diffractive Optical Elements

STEVEN RICHARD KITCHEN

Kamstrup A/S
Optics and Fluid Dynamics Department, Risø National Laboratory
Mikroelektronikcentret, Technical University of Denmark
Bourdon-Haenni A/S
Industrial Ph.D. Project EF 793, April 2003

—
2nd ed.
—
This document was compiled and typeset
13th June 2003
using the MIKTEX2 distribution of LATEX 2_ε
—
ISBN 87-550-3154-4
ISBN 87-550-3155-2 (Internet)
ISBN 0106-2840
—
Published by Risø National Laboratory, Roskilde, Denmark, April 2003
Print: Pitney Bowes Management Serviced Denmark A/S, 2003

Abstract

This thesis deals with the development of optical sensors based on laser diodes and dedicated diffractive optical elements. The thesis is divided into two parts. The first part of the thesis deals with development of interferometrically based displacement sensors intended for use in pressure transducers. For the purpose of probing the deflection of the diaphragm in a pressure transducer, a novel common-path interferometer has been developed. The central part of the common-path interferometer is a multi-functional holographic optical element (HOE) that handles function like beam splitting and focusing of the light. The HOE works as both transmitter and receiver in the common-path setup. This means that the stability is inherent in the HOE and the system is self-aligning, which makes the sensor very robust. There has also been devised a new technique to extend the unambiguous measurement range of differential displacements. This technique is based on probing three points on the object surface simultaneously and utilises the quadrature phase signals that are automatically provided by the specially designed HOE. During the project, there has also been developed a new tool for conceiving new types of common-path interferometers by placing a specially designed HOE in the Fourier plane of a 4-f setup. The surface structure for the Fourier filter can be calculated by Fourier transforming the desired impulse response function of the system. Thereby, the system can be designed to probe a specific type of surface displacement. The second part of the project deals with development of optical flow sensor systems. Firstly, a new beam splitter system based on two linear gratings has been devised. The beam splitter is intended for use in laser Doppler anemometry systems, where the fringe spacing in the measurement volume is directly proportional to the wavelength of the light source. This is compensated by the beam splitter system by letting the closing angle of the two probe beams be wavelength dependent. Secondly, a new laser time-of-flight sensor has been developed. The sensor is intended for in-situ calibration of other types of flow sensors, which are permanently installed in large flow installations. The system is designed so that the transmitter and receiver functions are implemented in a single HOE plane. This makes the LTV sensor self-aligning and robust. The multi-functional HOE is additionally designed so that the LTV sensor to a first degree is wavelength independent. All the diffractive structures are implemented as surface relief structures in photoresist. These structures have the advantage that they can be replicated using for instance injection moulding. Thereby one can mass-produce the structures at low cost, which makes it possible to manufacture a cheap optical sensor.

Dansk Resumé

Denne afhandling omhandler udviklingen af optiske sensorer baseret på brugen af laser dioder og dedikerede diffraktive optiske elementer. Afhandlingen er delt i to dele. Den første del omhandler udviklingen af interferometrisk baserede forskydningssensorer, som er tiltænkt brug i tryktransducere. Et nyt common-path interferometer er blevet udviklet med henblik på aftastning af afbøjningen af en membran i en tryktransducer. Den centrale del af common-path inteferometeret er et multifunktionelt holografisk optisk element (HOE), som varetager funktioner så som stråledeling og fokusering af lyset. Hologrammet virker som både sender og modtager i common-path systemet. Dette betyder, at stabiliteten af systemet sikres af hologrammet og at systemet er selvindstillende, hvilket gør sensoren meget robust. Der er også blevet udviklet en ny teknik til at udvide det utvetydige måleområde for differentielle forskydninger. Denne teknik er baseret på den samtidige aftastning af tre målepunkter på objektet og udnytter desuden de fase-kvadratur signaler, som automatisk genereres af det specialudviklede hologram. I løbet af projektet er der også blevet lavet et nyt værktøj til at udvikle nye typer common-path interferometre ved at placere et specialdesignet hologram i Fourier planet af en 4-f opstilling. Overfladestrukturen for Fourier filtret kan udregnes ved at Fourier transformere den ønskede impuls respons funktion for systemet. Derved kan systemet designes til at aftaste en bestemt type overfladeforskydning. Den anden del af afhandlingen omhandler udviklingen af optisk baserede flow sensor systemer. For det første, er der blevet udviklet et stråledeler system baseret på to lineære gitre. Stråledeler systemet er tiltænkt brug i laser Doppler anemometri systemer, hvor stribeafstanden i målevolumenet er proportional med den anvendte bølgelængde. Dette er kompenseret af stråledeler systemet ved at gøre vinklen mellem de to anvendte laserstråler bølgelængdeafhængig. For det andet, er der udviklet en ny laser time-of-flight (LTV) sensor. Denne sensor er tiltænkt som kalibreringsværktøj for andre typer flow sensorer, som er permanent installeret i store flow installationer. Sensoren er designet sådan, at sender og modtager funktionerne er implementeret i et hologram-lag. Dette gør sensoren selvindstillende og robust. Det multi-funktionelle hologram er desuden designet sådan, at LTV sensoren er tilnærmelsesvis bølgelængde-uafhængig. Alle de diffraktive strukturer er implementeret som overflade relief strukturer i fotoresist. Disse strukturer har den fordel, at de kan blive replikeret ved for eksempel sprøjtestøbning. Derved kan strukturen masseproduceres ved lave omkostninger, hvilket muliggør fremstillingen af en billig optisk sensor.

Preface

This thesis presents work carried out in the period October 1999 - March 2003 and is submitted in partial fulfilment of the requirements for the Ph.D. degree at the Technical University of Denmark (DTU). The work has been performed under the Industrial Research Education Ph.D. program (erhvervsforskeruddannelsen) and has been jointly financed by the Danish Academy of Technical Sciences (ATV), Kamstrup A/S and Bourdon-Haenni A/S.

The project was originally entitled “Optical Pressure Transducer” and was started in 1999 on the initiative of Kamstrup A/S and the Optics and Fluid Dynamics department (OFD) at Risø National Laboratory, while enrolling at Mikroelektronik Centret (MIC) at DTU. The project stems from an earlier industrial post-doc project, which was an industrial collaboration project (EPD 009/Risø) between Kamstrup A/S and OFD. This project was focused on the development of optical flow sensor techniques for use in heat meters. The intention of the industrial Ph.D. project was to strengthen the ongoing research on optical technologies, but with the focus on the development of optical techniques for use in pressure transducers. The industrial Ph.D. fellow was therefore employed in the process division of Kamstrup A/S. The composition of the project, however, was soon redefined due to the following events. In January 2000, the process division was bought up by the Swiss investment company, CGS Management, which also bought the process companies, Haenni Instruments in France and Bourdon-Sedeme from Switzerland. In 2001 the three companies merged, and the Danish limited company was called Bourdon-Haenni A/S. Due to a change of objective from the owners of Bourdon-Haenni, it was chosen to discontinue the Ph.D. project. Kamstrup A/S chose to continue the project, and thereby got an opportunity to intensify the already existing research program. From August 1st 2001, the Ph.D. fellow has been employed by Kamstrup A/S and working with optical flow sensors. Bourdon-Haenni A/S became fourth party in the project, which received the new working title: “Optical Sensors”.

Due to the above-mentioned events, this thesis deals with both development of optical displacement sensors and optical flow sensors. However, the systems bear much resemblance since both are based on the combination of laser diodes and dedicated diffractive optical elements.

Acknowledgments

There are many people, to whom I owe thanks for helping out in my project in one way or another.

First of all, I would like to give thanks to my supervisors from DTU, Aric K. Menon, and my supervisor from Bourdon-Haenni A/S, Lars Jakob Nielsen. You have always been helpful when I have needed it. I also owe thanks to my supervisor from Risø National Laboratory, Steen G.

Hanson, who has always given me a beating in scientific discussions, but in return has taken an equally big beating on the badminton court. Finally, but not the least, I owe much to my supervisor and colleague from Kamstrup A/S, Carsten Dam-Hansen. You have not only been an entrusted colleague, but have also been an impeccable friend throughout the project. You have always gone well beyond your duties as a supervisor, helping out with both technical and administrative tasks. Had it not been for you, this thesis would never have been written.

A great many thanks go to Kamstrup A/S for picking me up when things looked dark, and especially managing director, Poul Erik Schou-Pedersen, without whose enthusiasm for research, this project would never had been completed. Also a special thank-you to technical manager, Anders Skallebæk, who has always helped out when needed.

I also owe many thanks to my friends amongst the young people at Risø National Laboratory: Frederik Nielsen, Niels Kjærgaard, Bo Toftmann Christensen, Eva Samsøe, Peter Lodahl, Morten Bache, Thomas Nikolajsen, and Sussie Juul Jensen. You have not only been helpful in scientific discussion, but also in social discussions and off-hours activities. You have made my time at Risø National Laboratory an enjoyable one, and the table soccer matches will be greatly missed. A special thank-you goes to my friend, Kim G. Jespersen, with whom I have shared an office these past three years. It has been a blast, matey.

There are also a few more people, who have helped out one way or another during my project. I would like to express my thanks to Michael Linde Jakobsen, Henrik C. Pedersen, Peter E. Andersen, and Per Michael Johansen; also many thanks to my father, who has proof-read parts of the thesis. Finally, I owe much to my wife, who has always been supportive of me and put up with my shifting working hours (and hours spent on the golf course) - “Terimah kasih banyak, Sayangku, saya cinta kamu”.

STEVEN RICHARD KITCHEN
April 2003

List of Publications

During the period of the project, the PhD fellow has contributed to the following publications on which the present thesis is based:

Patents

1. S.R. Kitchen, C. Dam-Hansen and M.L. Jakobsen, Diffractive beam splitter for wavelength compensation of laser Doppler anemometry systems, pending US Patent No. 60/393,585

Articles

1. C. Dam-Hansen and S.R. Kitchen, Diffractive Laser Time-of-Flight Flow Sensor, in preparation
2. S.R. Kitchen, C. Dam-Hansen and M.L. Jakobsen, Diffractive beam splitter for wavelength compensation of laser Doppler anemometry systems, submitted to Applied Optics (OT-018662), November 2002
3. M.L. Jakobsen, S. Osten, S.R. Kitchen, C. Dam-Hansen and S.G. Hanson, Multiple beam time-of-flight sensor based on a VCSEL array, Measurement Science and Technology 14, March 2003, 329-335
4. S.R. Kitchen and C. Dam-Hansen, Holographic common-path interferometer for angular displacement measurements with spatial phase stepping and extended measurement range, Applied Optics 42, January 2003, p. 51-59
5. S.R. Kitchen, S.G. Hanson and R.S. Hansen, Introduction of the impulse response function in common-path interferometers with Fourier plane filters, Opt. Rev. (2001) 8, 378-381

Additionally, the PhD fellow has contributed to the following conference proceedings:

Proceedings

1. S.R. Kitchen, C. Dam-Hansen and M.L. Jakobsen, Diffractive beam splitter for use in laser Doppler anemometry systems based on laser diodes. In: Book of abstracts. DOPS annual meeting, Risø (DK), 21-22 Nov 2002. (Dansk Optisk Selskab; Forskningscenter Risø, Roskilde, 2002) 2 p.
2. C. Dam-Hansen and S.R. Kitchen, Holographic laser time-of-flight velocimeter. In: Book of abstracts. DOPS annual meeting, Risø (DK), 21-22 Nov 2002. (Dansk Optisk Selskab; Forskningscenter Risø, Roskilde, 2002) 2 p.

3. S.R. Kitchen and C. Dam-Hansen, Holographic common-path interferometer with extended measurement range for differential displacement measurements. In: Book of abstracts. DOPS annual meeting, Risø (DK), 21-22 Nov 2002. (Dansk Optisk Selskab; Forskningscenter Risø, Roskilde, 2002) 2 p.

4. S.G. Hanson, M.L. Jakobsen, S.R. Kitchen and S. Osten, Compact optically based systems for linear and angular displacement sensing. In: Proceedings. Part 2. 7. International symposium on laser metrology applied to science, industry, and everyday life, Novosibirsk (RU), 9-13 Sep 2002. Chugui, Y.V.; Bagayev, S.N.; Weckenmann, A.; Osanna, P.H. (eds.), (The International Society for Optical Engineering, Bellingham, WA, 2002) (SPIE Proceedings Series, 4900) p. 863-872

5. S.G. Hanson, S.R. Kitchen and R.S. Hansen, Impulse response function for common-path interferometers. In: Proceedings. 5. International conference on vibration measurements by laser techniques: Advances and applications, Ancona (IT), 18-21 Jun 2002. Tomasini, E.P. (ed.), (SPIE Proceedings Series, 4827) p. 323-330

6. S.R. Kitchen and C. Dam-Hansen, Holographic common-path interferometer for measuring tilt or vibrations utilising a spatial heterodyne principle. In: Proceedings. 5. International conference on vibration measurements by laser techniques: Advances and applications, Ancona (IT), 18-21 Jun 2002. Tomasini, E.P. (ed.), (SPIE Proceedings Series, 4827) p. 112-122

7. S.R. Kitchen and C. Dam-Hansen, Enlargement of the dynamic range for interferometric displacement measurements (poster). In: Programme. Abstracts. List of participants. Danish Physical Society annual meeting 2002, Nyborg (DK), 30-31 May 2002. (HCØ Tryk, Copenhagen, 2002) FF20P

8. S.R. Kitchen, S.G. Hanson and R.S. Hansen, Fourier plane filters and common path interferometry in vibrometers and electronic speckle interferometers. In: Optical engineering for sensing and nanotechnology. 2001 International conference on optical engineering for sensing and nanotechnology (ICOSN 2001), Yokohama (JP), 6-8 Jun 2001. Iwata, K. (ed.), (The International Society for Optical Engineering, Bellingham, WA, 2001) (SPIE Proceedings Series, 4416) p. 108-111

9. S.R. Kitchen, C. Dam-Hansen and S.G. Hanson, Optical displacement sensor based on common-path interferometry for industrial purposes. In: Program and summaries of contributions. Northern optics 2000, Uppsala (SE), 6-8 Jun 2000. Biedermann, K.; Olin, U. (eds.), (Swedish Optical Society, Stockholm, 2000) p. 134

Contents

1

Introduction

Never express yourself more clearly than you think.

Niels Bohr (1885-1962)

Since the invention of the laser, numerous optical metrology methods have been devised. Many of these optical systems, although proven to work in laboratory environments, still have to prove their applicability in industrial environments. Those systems that do take the step into commercial systems are often bulky and expensive.

Advances within especially the CD/DVD player and telecommunication industries have made laser diodes affordable. Combined with holographic or diffractive optical elements (HOEs/DOEs), laser diodes can provide cheap, robust, and compact systems that show promise for use in industrial environments. The advantages of using HOEs are that they can be constructed to maintain several optical functions of the system, such as beam splitting, focusing, and phase shifting. However, taking this step is not trivial. This is mainly due to the fact that the characteristics of laser diodes are sensitive to environmental changes, such as temperature. Since many industrial sensors require being functional in systems with changing environmental conditions, this introduces problems that need to be dealt with. An obvious step is to temperature stabilise the laser diode. However, even temperature stabilised laser diodes are undefined within 1-3 longitudinal modes. Since the diffraction angle of HOEs is wavelength dependent, this unavoidably introduces wavelength dependencies to the systems. However, in systems that have other wavelength dependencies, the dependency from the HOE can sometimes be designed so that they cancel out, yielding a system that is wavelength independent.

This thesis deals with the development of optical sensors based on laser diodes and dedicated diffractive optical elements. More precisely it deals with two types of sensors, viz. flow sensors and displacement sensors. The HOEs are written in positive photoresist using an analogue writing setup. The resulting holograms (after development) are surface relief holograms . There are other ways to implement the HOEs, such as volume holograms using dichromatic gelatine or amplitude holograms . The phase holograms (surface relief and volume holograms) have the advantage

compared to amplitude holograms that they are lossless. However, the surface structures can be replicated through for instance injection moulding using polymer materials, which is not possible with volume holograms. This means that the HOEs can be mass-produced at low cost, which is an important step in commercialising the sensor.

In many respects, it would be better to implement the diffractive structures in glass such as BK7 in the sense that glass is harder, more durable, more temperature stable, and resistant to humidity. However, the fabrication methods such as hot embossing and moulding yield unique possibilities for the use of polymers. For instance, injection moulding allows for a very high volume production and the unit cost can be very low. This is especially useful in the production of disposable optical sensors, for instance, for use in medical or biological applications. It is thus possible to make sophisticated diffractive structures in polymers, which is difficult or uneconomical using glass. It is also possible to make unique designs such as lens arrays or multifunctional holographic optical elements. The planar technology of replication makes it possible to integrate several pre-aligned structures on a single substrate. These planar substrates can be used in combination in a stacked planar optical structure, for instance, as suggested in Ref. [1]. Moreover, the diffractive structures can be produced with a very consistent quality, since they are all made from the same mould tool. This is especially important, if the alignment and stability of the system is inherent in the HOE.

Displacement Sensors (Pressure Sensing)

In the process industry, there is a tradition for measuring the pressure of a medium by probing the deflection of a thin diaphragm that faces this medium. The majority of the commercial pressure transmitters are either built from mechanical, piezo resistive, or capacitive principles. The mechanical manometer principles provide relatively simple systems [2], but has the disadvantage that they are attached to the diaphragm and consequently oppose the deflection of the diaphragm. This can of course introduce limitations to the measurement precision and the resolution of the system is also relatively low. Resistive methods such as strain gauges provides better resolutions, but have the same restraint as the manometer, since the strain gauge has to be attached to the diaphragm [3–5]. More recently, pressure sensors based on capacitive principles have been commercialised. The capacitive sensors provide excellent accuracy and are additionally characterised by being non-intrusive [6–9]. These are the same qualities that make optical sensor methods attractive.

The purpose of the first part of the thesis is to synthesise and describe new methods for pressure sensing based on optical measurement techniques. The potential methods are to be examined both theoretically and experimentally. As described previously, the final system must be compact and robust and it must be feasible to mass-produce the sensor at low cost. Optical methods are characterised by being non-intrusive and have the potential of a high measurement precision and resolution compared to the other probing methods mentioned.

The project was initiated with the intent to explore to what degree the implementation of optical methods in pressure sensors could improve the measurement precision as well as the possibilities of achieving a mechanical construction, which was simpler than that of the existing products. The ambition was to end up having an unique sensor technology with superior performance compared to the technologies used in products made by the competitors.

There are several optical methods that can be used to probe the deflection of the diaphragm. For instance, whole field illumination of the diaphragm can be used with the combination of a diffractive structure on the surface of the diaphragm, so that the reflected light is focused. An optical fibre collects the focused light, and as the diaphragm deflects, the wavelength that is focused onto the fibre end changes. By detecting the wavelength of the collected light, the deflection of the diaphragm and consequently the pressure can be calculated. One can also attach an optical fibre to the surface of the diaphragm. The light that is sent through the fibre will change its characteristics as the diaphragm deflects, and this can be used to calculate the deflection [10, 11]. However, this method has the disadvantage that the fibre has to be attached to the diaphragm, which can be both inexpedient with regards to measurement accuracy and production methods. Finally, there are also interferometric methods. For instance, the end of a fibre and the centre of the diaphragm can constitute the cavity of a low-finesse Fabry-Perot interferometer [12–14]. In this project it has been chosen to focus on the use of common-path interferometers. This choice has been determined by two factors. First of all, interferometry was chosen because of the potential high resolution this technique provides. Secondly, since it has been chosen to focus on the use of multifunctional holographic optical elements, the choice of common-path interferometry was an obvious one, since the beam splitting and focusing are easy to achieve, at the same time getting a system that is insensitive to common translations of the diaphragm, which is not the case for the Fabry-Perot interferometer.

Flow Sensor

An important part of energy meters for the district heating industry is a flow sensor that measures the flow in pipes. There exist numerous examples of fluid meters based on mechanical, differential pressure, magnetic inductive, ultrasound, or optical methods, just to name a few [15].

Mechanical methods such as rotating propellers to estimate the volume flow have a simple construction and are cheap to produce, but have a relatively low accuracy and the propeller is easily exposed to small threads and the like that are carried with the flow. These can stick to the propeller and change the mechanical properties and consequently the precision of the system. Furthermore, since the propeller has to be inserted into the flow, this can alter the properties of the flow by for instance introducing turbulence, which of course is inexpedient. Commercial heat meters based on ultrasound sensors provide excellent measurement accuracy of about 1-3% as well as a simple construction [15, 16]. The sensors in the ULTRAFLOW® series are based on ultrasound pulses sent along and against the flow. Based on the time difference between these pulses, the volume flow can be estimated. However, since the pulses are sent along the flow direction, this means that two mirrors are inserted into the flow. These obstruct the flow and can influence the measurement accuracy. In large flow pipe installations, the ultrasound transducers are implemented so that the measurements are performed across the flow pipe (with a component along/against the flow direction) and do not obstruct the flow. However, the area over which the ultrasound measurements is based is small compared to the entire cross-section, which can introduce large uncertainties.

The purpose of the second part of the project is to explore the possibilities of implementing optical technologies in these heat meters. Optical flow sensors are interesting, since a potentially high accuracy, as well as high acquisition rates can be achieved. The optical sensor also makes it possible to obtain flow measurements over a broad range from only a few mm/s to supersonic. Additionally,

optical methods are characterised by being insensitive to electromagnetic radiation. Furthermore, the optical methods have the advantage that they are non-intrusive, since only light has to be sent the point of interest. Another advantage of optical systems is that they have a very high spatial resolution, which means that one can obtain very accurate information about the flow characteristics. This is especially applicable in turbulent flows. However, the high spatial resolution is also a disadvantage, since one is often interested in measuring the volume flow, which is also the case for heat meters. This means that the volume flow in principle has to be calculated by integrating measurements over the entire cross-section of the pipe - a process that can be tedious and time consuming. However, there are techniques to simplify this process, where velocity measurements are taken at certain radii of the pipe. These techniques make it possible to obtain a relative accurate flow measurement from only 5-10 measurements of the local flow [17–19]. Another disadvantage of optical systems is that optical access is essential, necessitating the installation of a window in the flow pipe. These windows can in time be smudged by matter carried in the flow, which can influence the functionality of the sensor.

The most common used optical flow measurement principles are laser Doppler anemometry or velocimetry (LDA/LDV) and laser time-of-flight velocimetry (LTV). These are also the methods that are pursued in this part of the project. The purpose is to verify the applicability of these methods in industrial environments. The initial ambition is to end up with a sensor system that can be used for on-site re-calibration or re-verification of other types of flow meters permanently installed in large flow meter systems that are very difficult to disassemble. In the long run, the ambition is to end up with an optical sensor technology that can directly be implemented in the heat meter products.

Reader's Guide

The thesis is divided into five chapters (of which this introduction is the first) and one appendix. Chapter 2 gives a brief introduction to the different steps involved in the production of holographic optical elements. The chapter also describes how we have produced the HOEs used in the displacement and flow sensors. Chapter 3 describes the work on the development of interferometrically based sensor systems for probing differential displacements of an object, for instance the deflection of a diaphragm as used in pressure sensors. The chapter, amongst other things, describes a new method for extending the range of differential measurements. The work is described theoretically and verified experimentally.

The work on the development of optical flow sensor systems based on laser diodes and HOEs is described in Chap. 4. The work has been focused on two systems. Firstly, a novel beam splitter system for use in LDA probes has been devised. Secondly, an LTV sensor intended for in-situ calibration of other flow sensors permanently installed in the field has been developed. The systems are described theoretically and verified experimentally. Additionally, the systems are compared with a novel multiple laser time-of-flight sensor based on a VCSEL array.

Finally, the results from the project are summarised in Chap. 5 and some concluding remarks will be given. App. A describes the measurement of the wavelength dependency on the ambient temperature. This is a measurement that will be referred to several times throughout the report.

2

Holographic Optical Elements

The Colour of the World is changing day by day.

Victor Hugo (1802-1885),
Les Miserables

This chapter is intended as a brief description of the processes involved in the production of holographic optical elements (HOEs). The work of this thesis does not focus on the optimisation of the manufacturing process nor on the prediction of the surface structure of the HOEs. The processes have rather been used as a tool, which are used in order to get the desired performance. This chapter is thus not intended as a thorough analysis of the manufacturing process. However, in order to reproduce the results that are presented throughout the thesis, it is important to know the manufacturing process that we have used.

There are various ways to implement the HOEs, for instance as volume holograms in dichromatic gelatine or as amplitude holograms . The method we pursue is through surface relief holograms. This type is chosen due to the lossless nature of phase holograms (in contrast to amplitude holograms) and the fact that the surface relief structures can be written in photoresist and later replicated at low cost through for instance injection moulding, which is not possible with volume holograms.

If the interested reader would like to know more about the different processes, we would like them to refer to Refs. [20] for the chemistry processes of photoresist, Refs. [21, 22] for information on how to simulate and predict the profile of the surface structure, Refs. [23–26] for the aberration optimisation of HOEs, and Refs. [27, 28] for methods for replication of surface structures and injection moulding.

Reader's Guide

This chapter starts with a brief description of imaging holography . Subsequently, a basic description of the processes involved in writing in positive photoresist is given. Following, a short

description of aberrations in holograms is given and how the writing of holograms can be optimised through aberration balancing. Subsequently, the production method we have followed is described, and finally, a description of various replication techniques is given.

2.1 Imaging Holography

In 1948, Dennis Gabor suggested a new two-step, lensless imaging process, which we today know as holography [29]. Gabor realised that when a suitable coherent reference wave is present at the same time as light is diffracted or scattered from an object, then information about both amplitude and phase of the light from this object will be recorded, even if the recording medium is only sensitive to light intensity.

The fundamental problem in holography is that of recording and later reconstructing both amplitude and phase from an optical wave originating from an coherently illuminated object. In imaging holography, which we explore here, the object is a point source. Since it is coherent wavefronts that are to be reconstructed, it is necessary to record information of both amplitude and phase of the wave. Since the recording medium is only sensitive to intensity, it is necessary to somehow convert the phase and amplitude to intensity. A tool to achieve this is interferometry, where another wavefront, which is mutually coherent, but with known phase and amplitude, is added to the unknown wavefront. This recording of a pattern between an object wave and reference wave is what may be regarded as a hologram (see Fig 2.1 (a)).

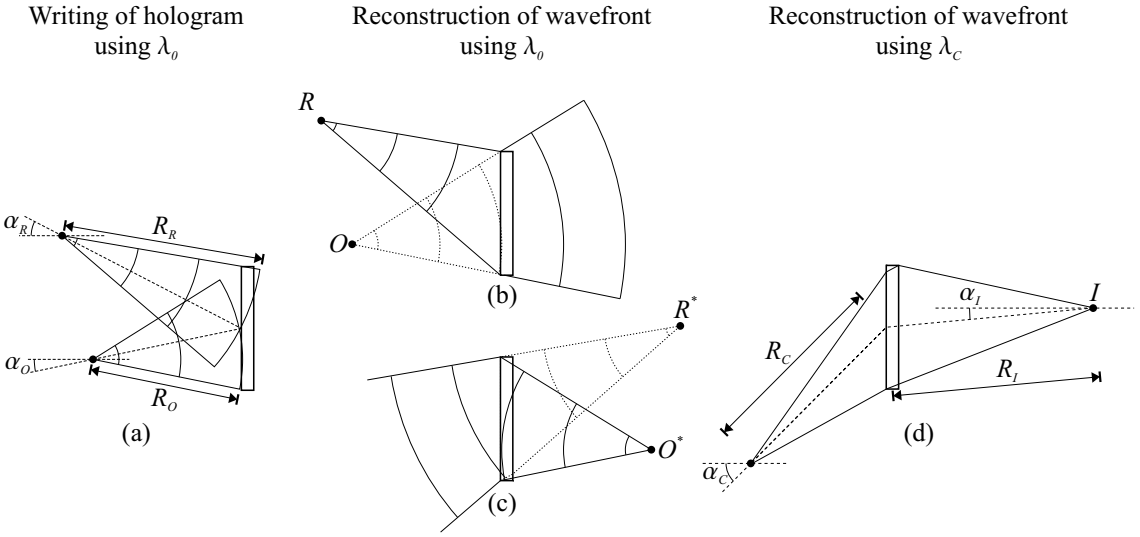

Figure 2.1: The basic steps in imaging holography. (a) shows the recording of the hologram using the object wave and reference wave, (b) shows the reconstruction of the original wavefront (virtual image) using an exact duplicate of the reference wave, (c) shows the reconstruction of the real image using the conjugate of the reference wave, and (d) shows the imaging using a reconstruction wave having a wavelength other than the writing beams.

When the amplitude and phase information about the object wave have been recorded, then it re-

mains to reconstruct this wave. If one uses a reconstruction beam, which is the exact duplicate of the reference wave, then a wave emerges that to a multiplicative factor is the duplicate of the original wavefront (see also Fig. 2.1 (b)). Similarly, if one uses the conjugate of the original reference wave as a reconstruction wave, then one obtains a wavefront that is proportional to the conjugate of the original wavefront (see also Fig. 2.1 (c)). In imaging holography, it should be mentioned that if the reference wave is used as reconstruction wave, then one obtains a wave that can be regarded as a virtual image of the original object. Similarly, if the conjugate of the original reference wave is used, one obtains a real image, where an actual focusing of the light occurs.

It should be noted that the only way to achieve aberration-free imaging is to use the exact reference wave or its conjugate in the reconstruction process. If it is not possible to use the same light source (or wavelength) for reconstruction of the wavefront, then one unavoidably introduces aberrations in the imaging. In this case, it is necessary to reduce the aberration using for instance an aberration balancing scheme, where the different types of aberrations introduced cancel each other out as described in Sec. 2.3. The important parameters to optimise are the radius of curvature, R, and angle of incidence, α, for the object and reference wave (denoted with subscripts O and R in Fig. 2.1 (a), respectively). These are determined by the desired radius of curvature and angle of incidence for the reconstruction and image waves (denoted with subscripts, C and I, in Fig. 2.1 (d), respectively). This optimisation has to be performed with the change in wavelength from the writing setup to the applied wavelength in the reconstruction setup taken into account.

2.2 Positive Photoresist

Positive photoresist basically works in the following way. One illuminates the photoresist with a certain intensity pattern. In the following development process, resist is removed in the areas where the resist has been illuminated, thereby leaving a positive image of the intensity pattern. In the following, a brief outline will be given on the different procedures involved in the production of surface relief holograms in positive photoresist and superficially describe the factors that have an influence on the shape of the surface structure.

Diazonaphthoquinone (DNQ) based positive photoresist consists of three different compounds: A resin (a novolak), a volatile solvent, and a photoactive compound (PAC) [20]. The dissolution rate of the pure novolak is significantly reduced when adding unexposed PAC. The photoactive compound is therefore often referred to as *the inhibitor*. As the resist is irradiated with wavelengths from 300 to 460 nm, which is the normal absorption band for DNQ based resist, the inhibitor absorbs photons and the diazo group of the PAC is split off by photolysis. As a result, the dissolution rate of the resist in the development process is increased.

The resist has a non-zero rate of dissolution, even when the PAC is unexposed. This results in film thickness loss even for finite development time. This is called *dark film loss* or *dark erosion*. Between the values of unexposed and fully exposed PAC, the dissolution rate increases in a non-linear manner as a function of the irradiation dose [20]. The dissolution rate for the unexposed PAC is a few Å/s and can be as high as a few hundreds nm/s for the exposed PAC [22].

The surface relief structure essentially depends on many features such as the exposure energy

variation across the resist, development time, the laser wavelength, developer concentration, and the refractive index of the substrate. However, there are many characteristics for the resist that have an influence on the final appearance of the photoresist and which should be taking into account if one wants to simulate or predict the shape of the final relief structure. First of all, the resist has a sensitivity threshold, which is the exposure value for which the dissolution rate is relatively unchanged. This usually means that the surface profile will get flat regions after development when exposed with a sinusoidal intensity pattern. This effect can be removed by using an uniform pre-exposure of the resist. However, this reduces the fringe contrast of the surface structure. A typical fringe contrast curve for positive resist is plotted in Fig. 2.2 [20]. In order to remove the flat regions, the resist must be exposed uniformly with a dose that is so high that the minimum film thickness becomes lower than the dark erosion height.

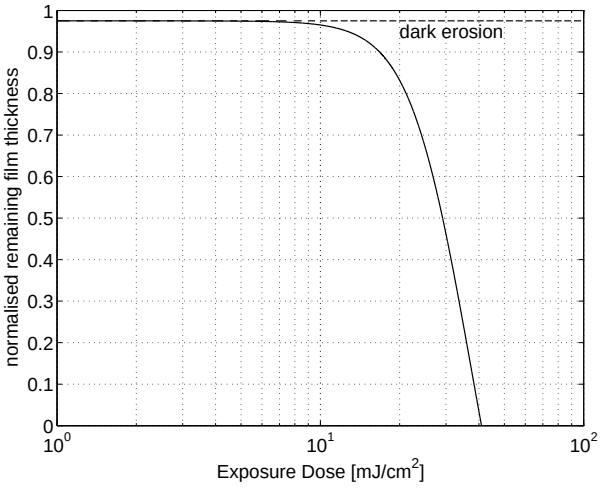

Figure 2.2: A typical contrast curve for positive resist. The film thickness normalised to the film thickness before immersion into the developer.

Another thing one should keep in mind, when wanting to simulate the profile is the so-called *bleaching* of the photoresist. When starting to expose the resist, the resist has a certain absorption coefficient. However, the photo products of the PAC have a lower absorption coefficient, which means that the resist is bleached during exposure. The last thing that should be taken into account is the fact that one often observes a reduction of the development rate near the air-resist interface, which can be attributed to the loss of solvent close to the photoresist surface [21]. These are all small non-linearities, which might explain the surface relief structures that are observed, especially in the case of making multi-exposed holograms (see also Sec. 3.2).

2.3 Writing of holograms and Aberration Balancing

When using holographic optical elements for purposes such as imagery or collimation, it is important to address aberration problems. The short analysis of these problems follows the procedure in Refs. [23–26].

Holograms show the classical Seidel image aberrations for lenses. However, the aberrations in holograms occur due to a mismatch between the wavefronts from the reference, object, and recon-

struction beams. Additionally, aberrations are introduced from the change in wavelength from the writing beams to the reconstruction beam. In fact, the only way to eliminate all types of aberration simultaneously, is to exactly duplicate one of the construction beams or its conjugate in the reconstruction phase. This will not normally be possible and is impossible in this case, where the photoresist is sensitive to blue wavelengths and the affordable laser diodes used in this project are red or near-infrared.

For the holograms constructed during this project, all point sources and focal points are in the same plane. This simplifies the expressions for the different types of aberrations, which also can be reduced to those of a rotational symmetric system. The Gaussian image properties of the holograms are also simplified and can be summed up in the following expressions:

$$\frac{1}{R_I} = \frac{1}{R_C} + p\mu\left(\frac{1}{R_0} - \frac{1}{R_R}\right) \tag{2.1}$$

$$\sin\alpha_I = \sin\alpha_C + p\mu\left(\sin\alpha_0 - \sin\alpha_R\right), \tag{2.2}$$

where μ is the ratio between the reconstruction wavelength, λ_C, and writing wavelength, λ_0, $p = -1$ denotes the real image, and $p = 1$ denotes the virtual image. The second term of the expression above is the focal length of the hologram (found by letting $R_C = \infty$).

The total wavefront deviation for the Gaussian sphere along the width of the hologram is given by the following expression:

$$\Delta_T = \Delta_S + \Delta_C + \Delta_A, \tag{2.3}$$

where the third order terms are assumed to give a sufficient description,

$$\Delta_S = -\frac{1}{8\lambda_C}x^4\left(\frac{1}{R_C^3} - \frac{1}{R_I^3} + p\mu\left(\frac{1}{R_0^3} - \frac{1}{R_R^3}\right)\right) \tag{2.4}$$

$$\Delta_C = \frac{1}{2\lambda_C}x^3\left(\frac{\sin\alpha_C}{R_C^2} - \frac{\sin\alpha_I}{R_I^2} + p\mu\left(\frac{\sin\alpha_0}{R_0^2} - \frac{\sin\alpha_R}{R_R^2}\right)\right) \tag{2.5}$$

$$\Delta_A = -\frac{1}{2\lambda_C}x^2\left(\frac{\sin^2\alpha_C}{R_C} - \frac{\sin^2\alpha_I}{R_I} + p\mu\left(\frac{\sin^2\alpha_0}{R_0} - \frac{\sin^2\alpha_R}{R_R}\right)\right), \tag{2.6}$$

where x is the lateral distance from the centre of the hologram, and the subscripts S, C, and A denote spherical, comatic, and astigmatic aberrations, respectively.

The aberration expressions as well as the Gaussian image properties are used to find the positions of the point sources for the two construction beams, giving the optimum grating period distribution across the hologram for given desired design properties. Since the parameters for the reconstruction and image beams are known, one is left with four unknown variables, and since there are five expressions, these parameters can be found.

In order to minimise the aberrations, the different types of aberration have to cancel each other out. First of all, the comatic aberrations are set to be zero for all values of x ($\Delta_C = 0$). Secondly, the spherical and astigmatic aberrations are set to cancel each other at the edges of the hologram aperture ($\Delta_S = -\Delta_A$). This leaves one with four expressions that are solved to find the four parameters for the construction beams. This yields four different solutions, where some of these can be ruled out, since they are complex.

2.4 The Writing Setup and Manufacturing Procedure

The manufacturing procedure of the holographic optical elements is described in the following. The positive photoresist is of the type, Shipley Microposist S2828. 4 ml of the photoresist is deposited on a glass substrate by spin coating for 30 seconds at 4000 revolutions per minute. The photoresist is thereafter soft baked at 90 degrees Celcius for 30 minutes. The resulting substrates are approximately 2.4 μm thick. The other side of the glass substrate is coated with an index-matched absorber, such that internal reflections in the writing setup do not ruin the desired structures. The entire resist is pre-exposed for 1.0-1.4 seconds with a mercury lamp or equivalently with an exposure dose of approximately 100 mJ/cm^2, corresponding to the threshold sensitivity of the resist.

The resist is now prepared for the writing process. The writing setup is depicted in Fig. 2.3.

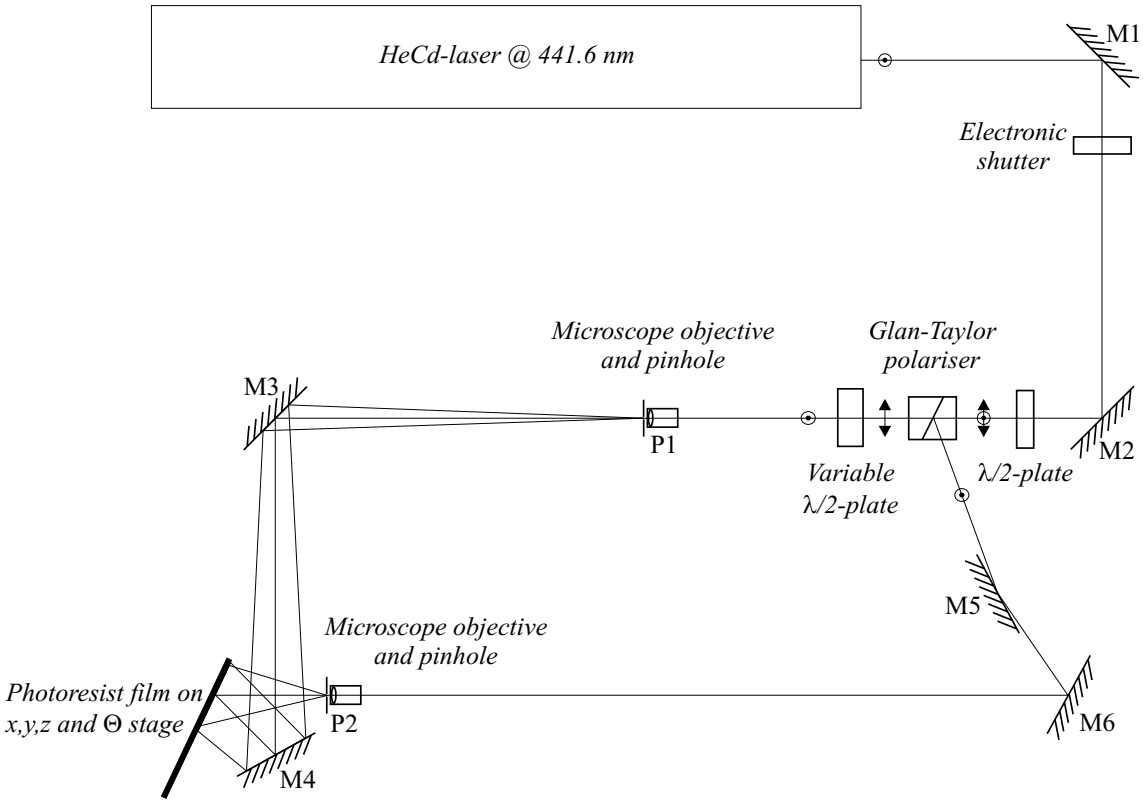

Figure 2.3: The writing setup for making the dedicated holographic optical elements.

The writing setup utilises a HeCd laser operating at 441.6 nm at 180 mW. The laser beam is sent through an electronic shutter, which can be set to obtain the desired exposure time. The laser beam is then sent through a halfwave plate, which can be set so that equal intensities for the two writing beams is achieved in the film plane. The beam then passes a Glan-Taylor polariser, which splits the laser beam into a vertical and a horisontal linearly polarised beam, which have equal power. The horisontal linearly polarised beam is sent through a variable halfwave plate that rotates the po-

larisation so that there are identical polarisations in the two laser beams and a high modulation can be obtained in the interference pattern, when the two beams are later mixed. Writing beam W1 is sent through a microscope objective with 20 times magnification and a pinhole, P1. Writing beam W2 is similarly sent through a microscope objective and a pinhole, P2, with the exception that the objective has 40 times magnification. The position of the pinholes can be adjusted to obtain the desired distances to the photoresist film. The angle of the film compared to the propagation direction from P2 can be set to the desired value, while the mirror, M4, ensures that the angle of the writing beam, W1, is set to the desired angle of incidence to the normal of the film plane.

There are several things one should keep in mind, when setting up the analogue writing setup. First of all, it is important that polarisation for the two writing beams is identical. Secondly, the optical path length of the two writing beams must be identical, since the coherence length for the isotope HeCd laser is only about 10 cm. Finally, all optical components should be screened such that one does not introduce diffraction effects to the film. Therefore, the setup is constructed with pinholes rather than lenses, which can introduce edge diffractions.

When writing the holograms, the procedure is as follows. First, a series of holograms is written. The exposure times for the different holograms are changed in (relatively large) fixed steps. After development, the different holograms are tested, and the one having the characteristics that are closest to those desired is identified. Subsequently, a new series of holograms is produced, where the exposure times are changed in small steps around the previously identified exposure time in order to achieve the optimum diffraction efficiency. Eventually, the most suited of the produced HOEs with respect to imaging properties and diffraction efficiency is chosen for the setup or replication.

For the development process, Shipley Microposit 351 Developer is used. The developer is diluted to 15% in demineralised water. The resist is developed for 3 minutes under agitation. The substrate is placed with the resist side upwards so that the removed resist flows to the surface of the developer. Agitation ensures that new developer is continually in contact with the resist, achieving even development over the entire hologram. After 3 minutes, the substrate is removed from the developer and is rinsed in demineralised water and is subsequently air-dried.

2.5 Replication of Diffractive Structures

The replication process basically involves making a copy of the original diffractive structure (the master) onto a metal tool called *the shim* or *the stamper* and subsequently copying this structure to workable material such as polymers.

Tools for Replication

In order to obtain a high quality replica of the diffractive structures, it is necessary to make a metal preform of the original diffractive structure. This preform is called a shim or a stamper and must be the negative of the desired diffractive structure. The shim can be manufactured using diamond turning in metal or through electroforming of the original diffractive structure. This so-called master can for instance be a surface relief grating implemented in photoresist. This master can be produced via E-beam writing or direct laser writing by computer generated structures, but also via

an analogue writing setup by using the interference between two coherent laser beams as used in this thesis.

The procedure for fabricating the shim is illustrated in Fig. 2.4

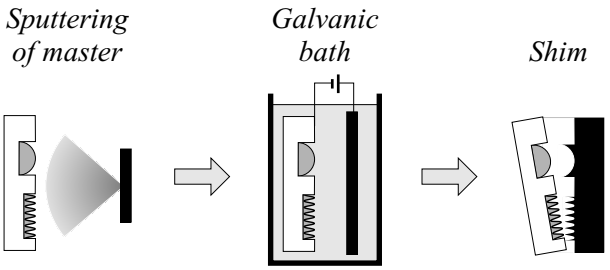

Figure 2.4: Fabrication of a shim from the master with the surface relief structure that are to replicated.

The fabrication method requires application of a thin layer of conducting material on the surface of the master. This can for instance be applied via ion-sputtering of for example gold, silver, or nickel. The electroforming of the shim is performed by lowering the master into a galvanic bath, where for instance nickel ions can be deposited on the master. Thereby one obtains a nickel shim that is a few hundreds microns thick, which is sufficient to enable the replication of diffractive elements having a surface relief depth of up to a few microns.

Replication Methods

There are various methods by which the replication of the shim can be performed. The choice for the proper method depends on the surface structure of the master and the shim. Here three common methods for replication will be briefly described, viz. hot embossing, injection moulding, and casting. The three methods are illustrated in Fig. 2.5.

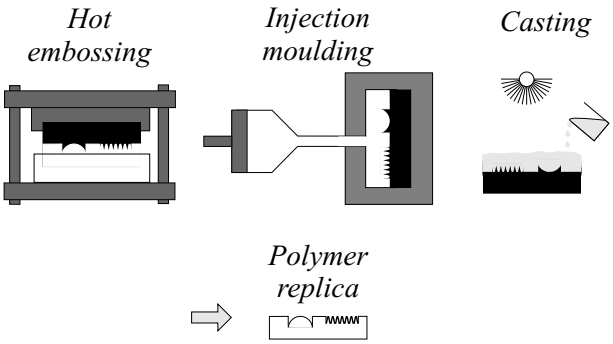

Figure 2.5: Three different replication processes for making a polymer replica.

In hot embossing, the shim is heated to a temperature above the softening temperature of the polymer and is pressed down into a flat polymer substrate. The result is that the surface structure of the shim is moulded into the top layer of the polymer. After cooling, the polymer replica is separated from the shim. This can be a crucial process, where it can be necessary to have pre-coated the

shim with a thin film. Low aspect ratios (depth to period ratios less than 1) can easily be replicated. Higher aspect ratios usually demand a higher degree of control, especially in the separation process. Furthermore, they demand a larger cycle time. For more information on the production of high aspect ratio structures via hot embossing, see for instance Ref. [30].

Injection moulding is widely used in the mass-production of plastic products. In connection with optics, injection moulding is, amongst other things, used for the production of collimation lenses for laser diodes, low-cost camera lenses, and compact discs. The polymer material is injected as a liquid resin into a temperature controlled mould with the shim inside. The liquid polymer fills the entire space in the cavity and is subsequently cooled and solidifies in the mould before the replica is removed. Injection moulding allows for very short duty cycle times (seconds) in connection with compact disc production. Injection moulding can in principle be used to produce sub-micron structures with depths exceeding 1 micron, i.e. high aspect ratios. However, this procedure is not trivial and it can be necessary to use special variations such as compression injection moulding, where the cavity is clamped after the liquid polymers have been injected.

For the casting process, a curable resin is poured in liquid state onto the shim. Depending on the choice of material, the resin can be cured either by heating or UV radiation. After curing, the replica can be separated from the shim. In order to obtain an optically flat obverse of the replica, a glass substrate can be used.

materials

The most common materials suited for replication of diffractive structures are thermoplastic polymers such as polycarbonate. The choice of material depends, amongst other things, on the desired optical properties of the polymer. Other important parameters to consider are the environmental properties such as water absorption.

A very important property of the polymers to consider is the shrinkage factor. The polymers can shrink as much as 0.7% after the moulding, which means that the shim has to be constructed with this in mind. The proper adjustments thus have to be made in the writing process, where the gratings periods of the diffractive structure have to be proportionally larger compared to the shrinkage factor.

The photo in Fig. 2.6 shows the first attempt of making a replica of the holograms used for the laser time-of-flight sensor described in Sec. 4.2.

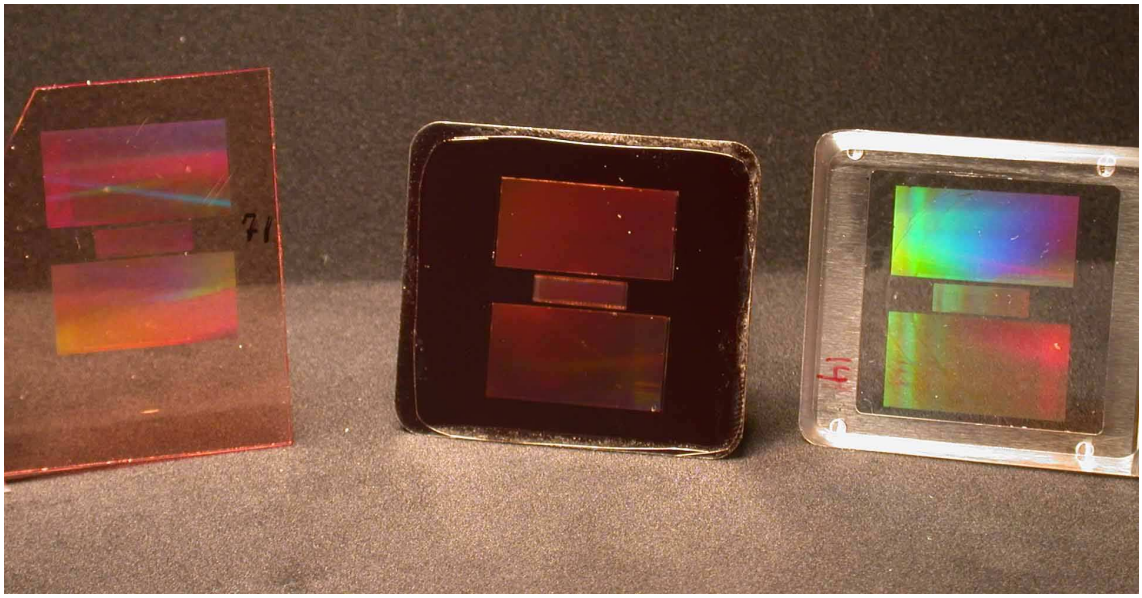

Figure 2.6: Photo showing from the left, the HOE for the laser time-of-flight sensor written in photoresist, the Nickel master, and the replica manufactured in polycarbonate via compression injection moulding.

3

Displacement Sensors Based on Common-Path Interferometry

The most exciting phrase to hear in science, the one that heralds new discoveries, is not "Eureka!" (I found it) but "That's funny..."

Isaac Asimov

When starting on the design of the optical pressure sensor, it was chosen to explore interferometric methods to probe the deflection of the diaphragm, due to the high sensitivity of these methods. However, it was soon realised that in order to achieve the goal of a dynamic range of 1:10,000 some sort of rough assessment of the deflection was necessary. It was also decided to explore the use of holographic optical elements for maintaining the optical functions of the system in an attempt to construct a compact and robust sensor and making it possible to mass-produce the system at low cost.

There are given numerous examples of optical methods for making differential measurements of surface displacements or deformations in the literature. For angular displacements alone, the methods are varied, such as feedback in laser diodes [31], the internal-reflection effect at an air-glass boundary [32], and interferometric methods [33, 34].

Interferometric methods to probe displacements, vibrations or deformations [35–37] have advantages with regards to high sensitivity. However, interferometric techniques usually have a limited range in which an absolute measurement can be made, and the results can be directionally ambiguous. Phase stepping techniques can remove this ambiguity and extend the dynamic range for absolute measurements to one wavelength. However, in order to implement the phase stepping technique, several polarising optical elements or an active element are often needed. Other methods for introducing the phase step utilises diffraction gratings or dedicated holographic elements together with interferometric techniques [38–40].

In order to increase the measurement range beyond one wavelength, techniques such as two-wavelength interferometry may be used [37, 41–43]. Other well-known methods for extending the measurement range are for instance phase unwrapping techniques [44] or sub-Nyquist interferometry [45, 46].

Common-path interferometers are advantageous compared with other types of interferometers with respect to sturdiness, since they are insensitive to common object translations and only require a limited coherence length of the light source.

We propose a new type of common-path interferometer that extends the measurement range and where phase stepped signals are spatially provided by a specially designed HOE (see Sec. 3.3). The system expands upon an earlier differential displacement sensor [47] and an earlier vibrometer system [35]. The former of these systems is described in Sec. 3.1. Common to both of these systems as well as to the new common-path interferometer is that they are based on laser diodes and the optical functions such as beam splitting and focusing are implemented in a single HOE. The system described in Sec. 3.1 can probe differential displacements between two points on a specular surface with a resolution of 0.5 nm. The new system extends upon this system by introducing a third probing point, thereby providing a second interference signal having a different spatial frequency. At the same time the new system utilises the three spatially phase stepped signals, which are automatically provided by the HOE as shown in the measurements in Sec. 3.2.

The new method for extending the measurement range works similarly to two-wavelength interferometry, since the system provides two interference signals having different spatial frequencies. However, an advantage of the system that we propose is that it only uses one wavelength and the measurement range is determined by choosing the proper distances between the probing points. The method is demonstrated by measuring the angular displacement of a mirror. It is shown that the system can probe the angular change with a ratio between the sensitivity and the measurement range of approximately 1:14,000. We believe that the system is best suited to measure this type of object displacement, and the insensitivity to external perturbations as well as the spatially provided phase stepped signals gives the system great potential for measurements of dynamic angular displacement of mirror-like surfaces. However, the technique, as we will also indicate, is not necessarily restricted to this application and can easily be modified to probe other types of surface displacements as for instance the deflection of a circular diaphragm in a pressure transducer.

Additionally, a new tool for conceiving new types of common-path interferometers by placing a specially designed HOE in the Fourier plane of a 4-f setup has been devised. The surface structure of this HOE can be calculated by Fourier transforming the desired impulse response function of the system. Thereby, the system can be designed to probe a desired type of surface deflection. The tool is described in Sec. 3.4.

3.1 Initial Optical Displacement Sensor

The objective of the system first constructed was to explore how high a resolution or sensitivity could be achieved. This was necessary in order to estimate the measurement range needed

to achieve a dynamic range of 1:10,000. The results presented here were first published at the Northern Optics Conference 2000 [47].

3.1.1 The Constructed System

In a typical common-path interferometer, a laser beam is split up into two beams, which are sent to and reflected or scattered by an object. The two reflected light beams are mixed and the interference signal is observed, making it possible to detect differential displacements between the two probing points on the object surface.

The central part of the constructed differential displacement sensor is a holographic optical element (HOE), which works both as transmitter and receiver in the system. The HOE had originally been devised for use in a laser time-of-flight velocimeter [48] (one of the early prototypes of the sensor described in Sec. 4.2). However, in contrast to the use in the displacement sensor, the LTV system utilised a second dedicated HOE to collect the backscattered light, thereby imaging the light from the two probe beams onto two detectors. By using the same HOE as both transmitter and receiver in the system, the light reflected from the object surface is mixed and an interference signal can be measured on a detector.

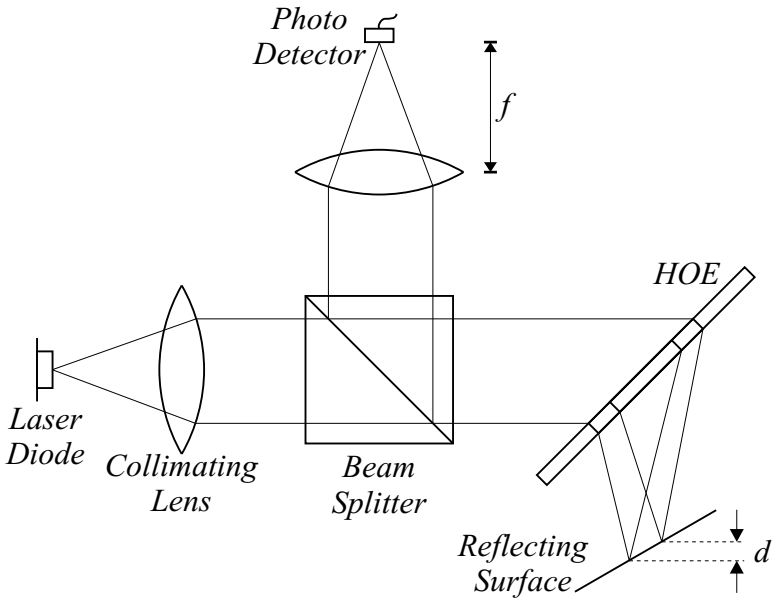

Figure 3.1: The setup for the differential displacement sensor.

The differential displacement sensor was constructed as shown in Fig. 3.1. The collimated light from a laser diode (Sharp LD021MD) operating at $\lambda = 785$ nm and $P = 7.8$ mW is focused onto two spots on the object surface having a spacing of 650 μm. The focal lengths of the lens elements are such that the focal points are 37 mm from the centre of the HOE. The required optical functions in the sensor such as beam splitting, focusing, recombination and collimation of scattered and reflected light are combined into a single HOE. This enables the construction of a compact and robust sensor.

The HOE consists of two partially overlapping lens elements. The large diffraction angle (the light is deflected 90 degrees) ensures that a high overall diffraction efficiency of approximately 40% of the incoming light is obtained. The displacement of the lens elements in the writing process determines the spacing between the foci. This is to a first degree independent of small changes in the operation wavelength of the laser diode.

As the two interfering beams follow the same path, both to the target and to the photo detector, the interference term or the AC-part of the detector signal will be determined by the axial displacement, d, between the two probe beams on the object surface (see Fig. 3.1),

$$i \propto \cos\left(\frac{4\pi}{\lambda}d + \varphi\right), \tag{3.1}$$

where λ is the operation wavelength and φ is a constant phase term. It can be seen that the phase of the detector signal is insensitive to any collective translation of the object.

The objective for the construction of the system was to explore the resolution or sensitivity obtainable by the system. The resolution is determined by how many intervals the interference signal can be divided into and is thus determined by the peak-to-peak voltage, V_{pp}, and the standard deviation, σ, of the measurements, or in other words the signal-to-noise ratio. Knowing that there is a $\lambda/2$ distance between two peaks of the interference signal due to the reflection setup, the resolution will approximately be given by:

$$R = \frac{\lambda/4}{V_{pp}/\sigma} \tag{3.2}$$

In the following section, the measurements of the resolution for displacement measurements on mirror-like surfaces as well as rough surfaces will be explored.

3.1.2 Measurements

The measurements were performed by using a gimbal mirror mount as shown in Fig. 3.2.

The rotation of the stage induces an axial displacement, d, between the two probing points on the object surface. The rough adjustment of the displacement is handled by a micrometer screw while a piezo transducer handles the fine and touch-free adjustment.

The measurements were performed by translating the piezo transducer in fixed steps. For each position, data was collected over 1 second, and the mean detector output and standard deviation of the static measurement were calculated. The measurements were performed with two different piezo transducers having a total deflection of 15 and 90 μm, respectively. The stepwise introduced axial displacement between the two probing points was 3.6 nm and 18 nm, respectively.

Mirror as Object Surface

The measurements that were carried out using a specular object surface (a mirror) are shown in Fig. 3.3.

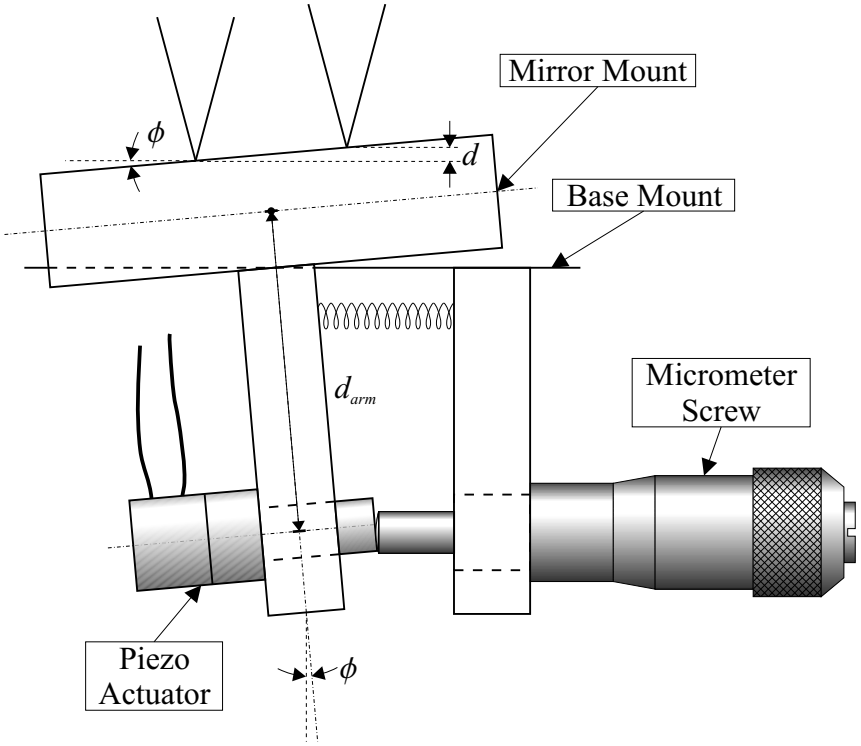

Figure 3.2: Illustration of how the axial displacement between the two probing point is obtained by rotating a mirror on a gimbal mount.

The measurements performed with the 15 μm piezo transducer showed a modulation depth of 69% with a peak-to-peak detector output of 9.98 V. The maximum measured standard deviation was 39.0 mV while the average was 10.4 mV (see Fig. 3.3 (a)). Using Eq. (3.2) this gives an average sensitivity of 0.2 nm and in the worst case 0.77 nm.

A similar measurement was carried out with the 90 μm piezo transducer. Although having a decreased modulation depth (51%), the measurements show better resolution due to less noise. The measurements show an average resolution of 0.15 nm and a worst case resolution of 0.52 nm.

Ceramic Disk as Object Surface

Similar measurements was performed with a gold-covered ceramic disk as target, which had a roughness, *Ra*, of approximately 500 nm. The measurements are shown in Fig. 3.4.

The measurements distinctively show interference, although with a much lower peak-to-peak voltage of 100 mV and a modulation depth of only 25% (see Fig. 3.4 (b)). The maximum and standard deviations are 1.23 mV and 0.91 mV, respectively. This gives a resolution of approximately 2 nm, although only over a short displacement range.

The measurements over a larger displacement range clearly show variations in the modulation,

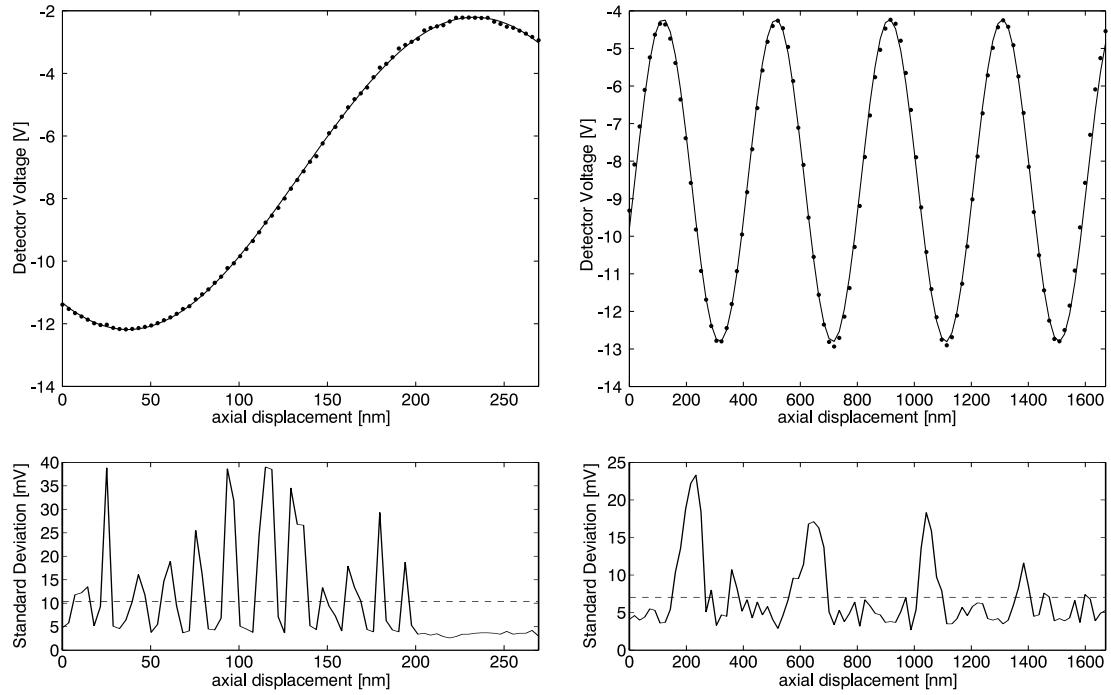

Figure 3.3: The measurements when measuring differential displacements on a mirror. The dashed line shows the average standard deviation for the entire measurement range.

which must mainly be caused by speckle noise.

3.1.3 Summary

There was much experience gained from the construction of – and measurements on – the initial displacement sensor. Firstly, it was demonstrated that a high resolution was obtainable using dedicated HOEs to handle the optical functions in the system, i.e. approximately 0.5 nm on specular surfaces and 2 nm on rough surfaces. Moreover, it was found that the system was inherently stable due to the common-path concept and the use of the HOE as both transmitter and receiver in the system. The system was thus insensitive to common vibrations of the object, at least within the confocal parameter, which was approximately 0.5 mm. The optical alignment was embedded in the HOE, which reduced the need for alignment during assembly and use of the system.

However, the measurements also showed that a lot of improvements to the system could be obtained. First of all, a general optimisation of the system was necessary, especially for the case of measuring the displacement of rough surfaces. It could also be seen that the resolution of the system was lower around the deflection tangents of the interference signal. It was therefore evident that the quadrature phase signal of the interference signal was needed in order to obtain a high resolution over the entire displacement range. It was also clear that it was necessary to find a method to determine the phase of the interference signal. Finally, it was also made clear that the unambiguous measurement range for the system should be extended in order to achieve the desired

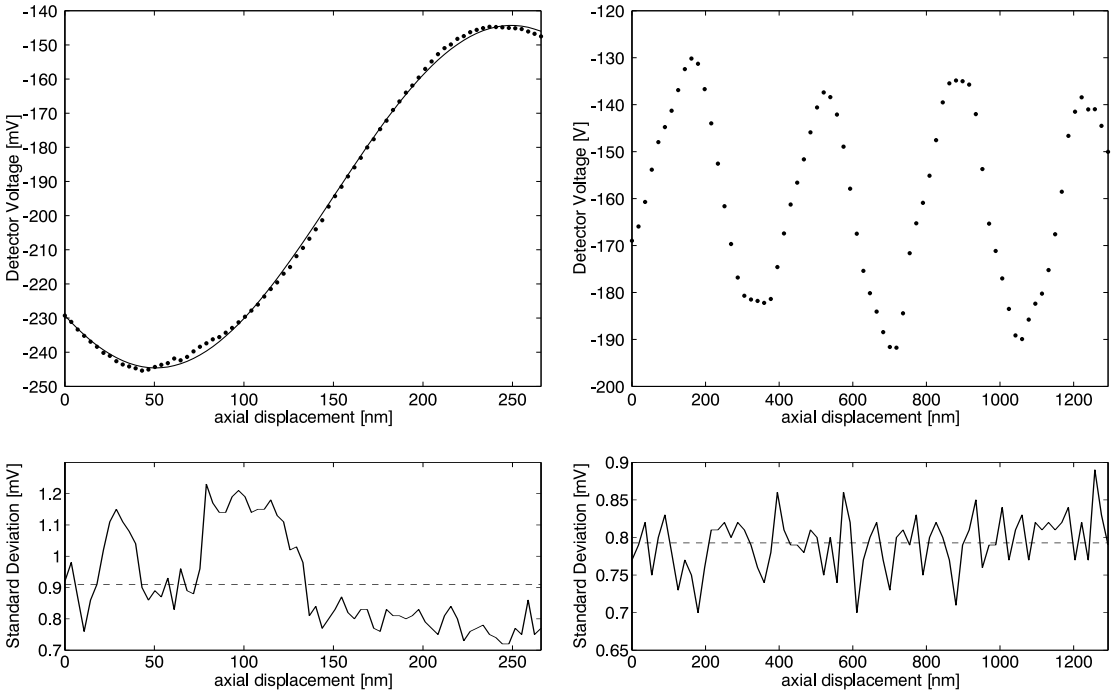

Figure 3.4: The measurements when measuring differential displacements on a rough surface. The dashed line shows the average standard deviation for the entire measurement range.

dynamic range, since only a dynamic range of approximately 1:1,000 was obtainable, even if the quadrature phase signal was provided in the system. Therefore, some sort of coarse measurement of the deflection had to be implemented.

3.2 New Displacement Sensor with Quadrature Phase Signals

After the experience with the initial displacement sensor, there was a number of changes we wanted to apply to the system. One of these changes was to change the diffraction angle so that the angle of incidence to the normal of the HOE plane was 45 degrees and the diffraction angle perpendicular to the HOE plane. This would simplify the writing process of the HOE, since the lens elements should have the same focal length. It would also simplify the alignment of the system, since the HOE would be parallel to the object surface.

Furthermore, it was chosen to construct some HOEs that introduced a third probe beam in an attempt to extend the range for unambiguous measurements (see more about this in Sec. 3.3). When the HOEs were written, a number of 2-lens HOEs and 3-lens HOEs were produced. The exposure time for the different HOEs was varied in order to obtain the optimum diffraction efficiency in the desired diffraction order. At the time of production, the problem with obtaining the quadrature phase signal was not solved.

The introduction of the third probe beam made it somewhat more difficult to distinguish the dif-

ferent interference signals. It was therefore chosen to observe the intensity profile in the detector plane using a photo diode array without the use of a focusing lens in order to get a clearer picture of the interference. We were immediately surprised to observe interference at several positions in the array. Even more surprisingly, it turned out that two quadrature phase signals were provided automatically by the HOE, the two signals being shifted ± 90 degrees from the main diffraction order. On further examination, it became clear that the quadrature phase signals were also present for the 2-lens HOEs. This fact ensures that high resolution is obtainable for the entire displacement range and it also enables the use of several methods to determine the phase of the interference signal.

3.2.1 The System

The optical displacement sensor with quadrature phase signals consists of a collimated laser diode operating at 785 nm, a multi-functional HOE, and a photo diode array as illustrated in Fig. 3.5.

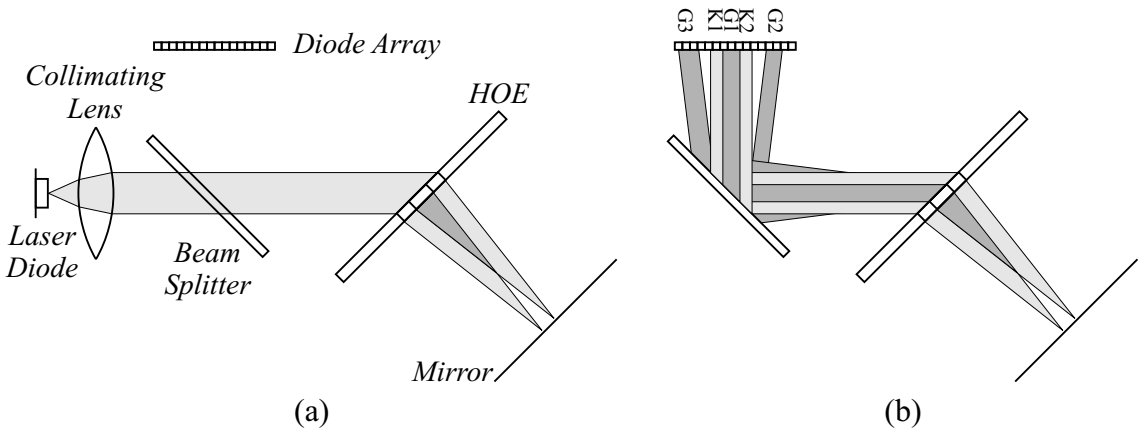

Figure 3.5: The setup for the common-path interferometer showing (a) the HOE when operating as transmitter in the system and (b) the HOE operating as receiver in the system.

The central part of the constructed common-path interferometer is the HOE, which operates as both transmitter and receiver in the system. For the sake of clarity, we will describe these two functions separately.

Figure 3.5 (a) illustrates the function of the HOE when operating as a transmitter. The collimated light from a laser diode, operating at 785 nm, is sent to the HOE at an angle of incidence of 45 degrees to the normal of the HOE plane and the observed diffraction order is diffracted normal to the HOE plane. The HOE is written as two partially overlapping lens elements, which are written sequentially using a 3.8 mm wide aperture. Between the two exposures, the film was displaced 1.2 mm, making the total width of the HOE 5 mm. The focal length of the lens elements is 35 mm for the operation wavelength. This yields a full width at half maximum width (FWHM) of 8 μm in the focal plane and the confocal parameter is 0.5 mm. The light from the 0th order reflection can easily be removed due to the large angular separation between diffraction orders. The applied diffraction order contains 40% of the total transmitted power. In order to obtain the focusing effect, the grating period must vary across the aperture of the lens elements, so that the

diffraction angles will also vary across the aperture. Due to the writing process in which the film is displaced between recordings, the overlap area of two adjacent lens elements will consist of two gratings having different grating constants. As a consequence, a beat between the two gratings or a *difference grating* will appear in the overlap area. The grating constant of the difference grating will be approximately constant across the overlap area. The difference grating has an important effect when the HOE is used as a receiver in the system (see more about this later in this section).

Figure 3.5 (b) illustrates the function of the HOE, when operating as a receiver in the system. The light reflected from the two points on the object surface is collected by the HOE and diffracted in the opposite direction to the incoming laser beam (see also Fig. 3.5 (a)). Provided that the object is in the focal plane of the HOE lenses, the reflected or scattered light will be re-collimated by both of the two lens elements and is sent to the detector array via the beam splitter as parallel beams. Therefore, the area of the HOE where the lens elements are overlapping will cause co-propagating overlapping beams originating from the two points on the object. Thereby, interference between the light reflected from these two points on the object surface can be measured. The interference that can be observed from the dark grey tinted area, G1, on the diode array stems from mixing of the reflected light from the two points on the object surface. In the light grey tinted areas, K1 and K2, the signal intensity does not change as the displacement between the two points on the object surface is changed. The light in these areas stems from the outer part of the HOE, where only one lens element is written and therefore no interference is observed here. The co-propagating beams ensures a good modulation depth of the interference signals and since the HOE both operates as transmitter and receiver, the system is self-aligning and the stability of the system is thus inherent in the HOE.

However, the difference grating that arise in the overlap area will also cause the light to be diffracted in slightly higher and lower angles than the main diffraction. These so-called sidebands will be observed on the detector array at positions G2 and G3, respectively. More importantly, the interference signals in the sidebands are shifted $\pm\pi/2$ in phase from the signal in the main diffraction order. Thereby, the HOE automatically provides three phase stepped signals needed for determining the phase of the interference signal.

3.2.2 Surface Profile for the Holographic Optical Element

As already mentioned, the grating period must vary across the apertures of the lens elements in order to obtain the focusing effect. Since the desired diffraction angle and focal length of the lens elements are known, the grating period Λ_c as a function of the lateral position of the HOE can be calculated using the following expression:

$$\Lambda_c(x) = \frac{\lambda_c}{\sin\theta_c - \frac{x_i - x}{\sqrt{(x_i - x)^2 + z_i^2}}} \tag{3.3}$$

where λ_c is the applied wavelength, θ_c is the angle of incidence, (x_i, z_i) is the coordinate for the focal point, and x is the lateral position in the HOE plane (see also Fig. 3.6). In the derivation of the expression it is assumed that the HOE is illuminated by a plane wave.

We choose to let the origin of the system of coordinates be the centre of the HOE. In the current setup, where the focal length of the lens elements is 35 mm and the lens elements are separated

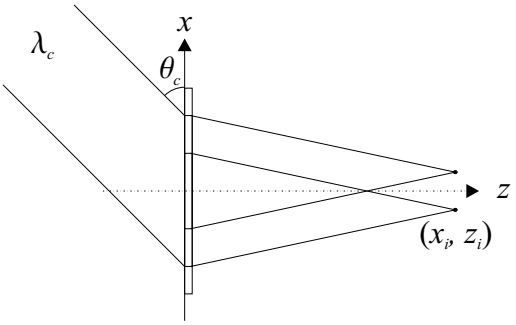

Figure 3.6: Illustration of construction and image beam and parameters for calculating grating period.

by 1.2 mm, this means that the positions of the focal points are $(-0.6,35)$ and $(0.6,35)$ mm, respectively. Inserting these parameters into Eq. 3.3. gives the grating period distributions as illustrated in Fig. 3.7. The grating period varies from 1.031 μm to 1.202 μm across the aperture of the lens element.

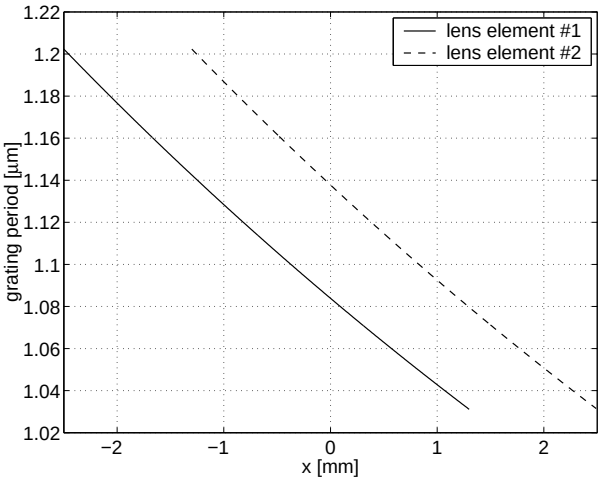

Figure 3.7: The grating periods for the two lens elements across the HOE.

As it can be seen from Fig. 3.7, the grating periods of the two lens elements differ for a given position on the HOE. This means that a beat between the two gratings will appear in the surface structure. The *k*-vector for this difference grating or envelope, which arises due to the double exposed HOE, is given as the difference between the *k*-vectors, k_1 and k_2, of the individual gratings,

$$k_{diff}(x) = k_1(x) - k_2(x) = \frac{2\pi}{\Lambda_{C1}(x)} - \frac{2\pi}{\Lambda_{C2}(x)}\,, \tag{3.4}$$

where Λ_{C1} and Λ_{C2} are the grating periods for the two individual lens elements, respectively. The period for the difference grating is easily calculated using $\Lambda_{diff} = 2\pi/k_{diff}$. The period for the difference grating is plotted in Fig. 3.8.

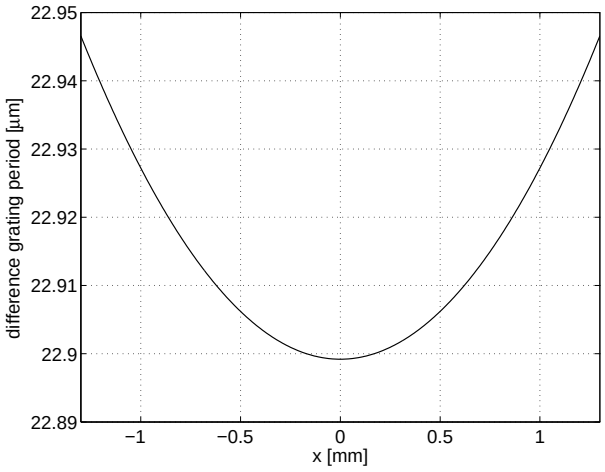

Figure 3.8: The period of the difference grating as a function of the lateral position on the HOE.

It is seen that the period of the envelope to the surface profile is approximately 20 times greater than the grating period of the lens elements.

The surface profile about the centre of the HOE should have the following expression (observing only a small part of the HOE):

$$h(x) = h_0 + h_1 \cos\left(\frac{2\pi}{\Lambda_{C1}(0)}x\right) + h_2 \cos\left(\frac{2\pi}{\Lambda_{C2}(0)}x\right) , \tag{3.5}$$

where h_0 is the average thickness of the phase grating and h_1 and h_2 are the amplitudes for the two overlapping gratings, respectively. The shape for $h_1 = h_2$ is therefore expected to be similar to the shape plotted in Fig. 3.9 (a).

Although one can easily observe the beating between the two gratings, only the two gratings are present. However, small non-linearities in the resist depth with respect to the exposure intensity, exposure time and the development process can make the surface profile appear more *flat* (see also Sec. 2.2), as would be the case if the difference grating manifested itself as a third grating,

$$h(x) = h_0 + h_1 \cos\left(\frac{2\pi}{\Lambda_{C1}(0)}x\right) + h_2 \cos\left(\frac{2\pi}{\Lambda_{C2}(0)}x\right) + h_3 \cos\left(\frac{2\pi}{\Lambda_{diff}(0)}x\right) , \tag{3.6}$$

where h_3 is the amplitude for the difference grating (see Fig. 3.9 (b)). The scanning electron microscope (SEM) scans do show that the envelope to the surface of the HOE in the area where two gratings have been written is in fact flatter than the envelope of the *ditches*, although the profile of the grating is more saw-toothed shaped rather than sinusoidal (See Fig. 3.10).

3.2.3 Calculation of Diffraction Angles and Phase

This section will give an overview of the diffraction angles obtained from illuminating the HOE and the phases of the different diffraction orders. The analysis will be performed both with and without treating the difference grating as a third grating in the overlap area of the HOE.

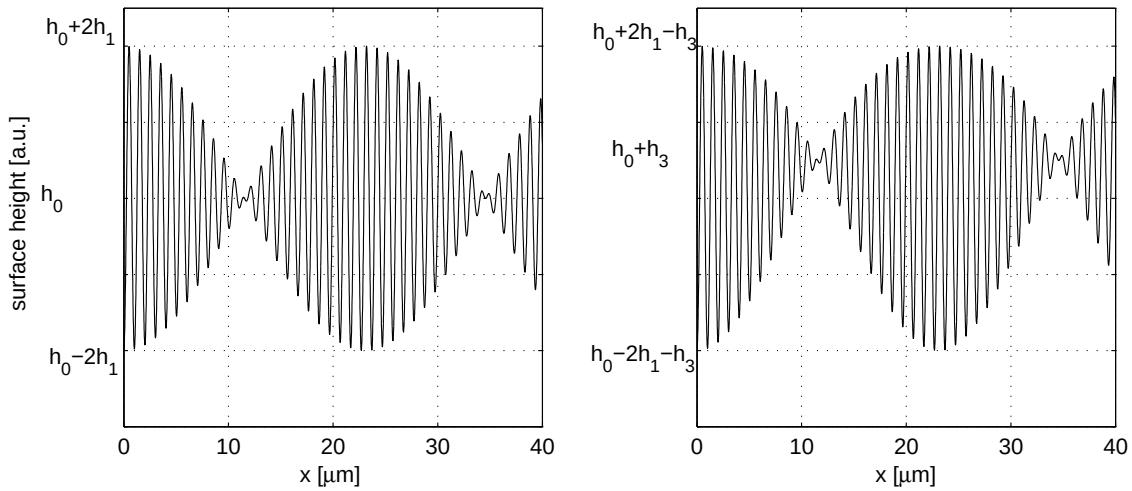

Figure 3.9: Illustration of surface profile for double exposed HOE when (a) only the two grating components are present in the structure and (b) when the difference grating appears as a third grating.

We assume a lossless grating ($\left|\vec{t}(x)\right| = 1$) with a complex transmittance [49],

$$\vec{t}(x) = \exp[-i\phi(x)]\,, \tag{3.7}$$

where ϕ is the phase function for the grating.

Single Exposed Holographic Optical Element

In order to keep the explanation simple, we will treat the case where only one sinusoidal grating has been written. Assuming that the phase shift introduced by the grating is linear proportional

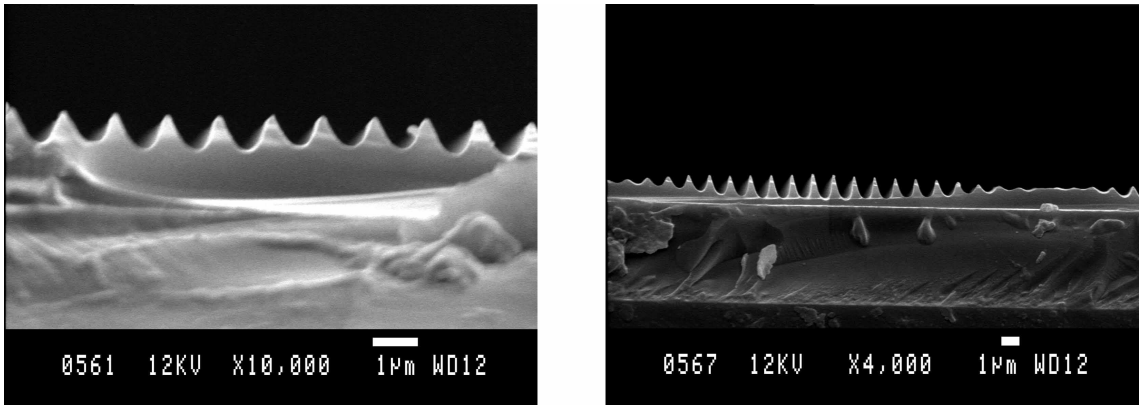

Figure 3.10: SEM scans of the HOE in (a) the area where only one grating has been written and (b) where two gratings have been written.

to the intensity profile of the holographic writing setup, the phase and transmittance function take the following form:

$$\phi(x) = \phi_0 + \phi_1 \cos(kx) \tag{3.8}$$

$$\Downarrow$$

$$t(x) = \exp[-i\phi_0] \exp[-i\phi_1 \cos(kx)] , \tag{3.9}$$

where k is the grating vector. Expanding the transmission function yields the following expression:

$$\begin{aligned} t(x) &= \exp[-i\phi_0] \sum_{n=-\infty}^{\infty} i^n J_n(\phi_1) \exp[inkx] \\ &= \exp[-i\phi_0] \left(J_0(\phi_1) + 2 \sum_{n=1}^{\infty} i^n J_n(\phi_1) \cos[nkx] \right) , \end{aligned} \tag{3.10}$$

Where J_n is the nth order Bessel-function. From here on, we neglect the constant phase term, $\exp[-i\phi_0]$, and assume that a second order expansion of the above term is sufficient for the analysis of the diffraction angles,

$$t(x) \approx -2J_2(\phi_1)\cos(2kx) + 2iJ_1(\phi_1)\cos(kx) + J_0(\phi_1) . \tag{3.11}$$

Assuming that the angle of incidence is either 0° or 45°, then only 3 diffraction orders will be observed as depicted in Fig. 3.11 with their respective phase shifts compared to the 0th order diffraction. It is also seen from Eq. 3.11 that the difference in phase shift between two adjacent diffraction orders is 90 degrees.

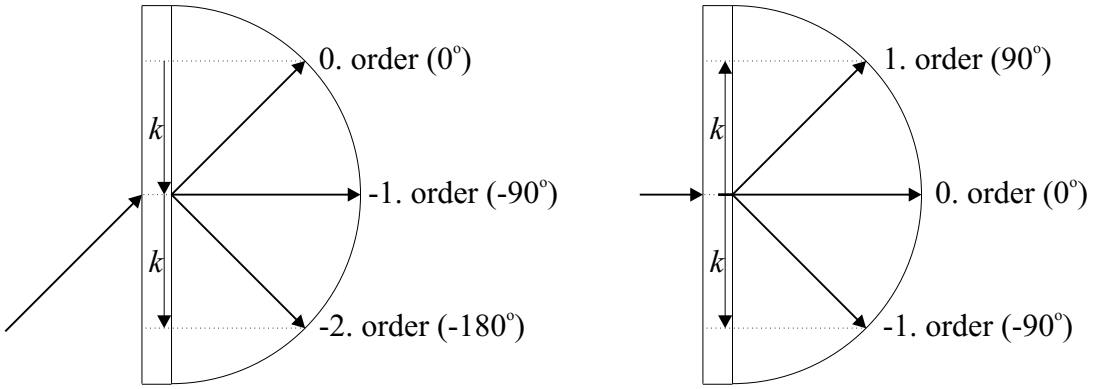

Figure 3.11: Observed diffraction orders and corresponding phase shifts at the centre of the lens element when the angle of incidence is (a) 45 degrees and (b) 0 degrees.

3.2.4 Double Exposed Holographic Optical Element

Here, the same approach as for the single exposed HOE is followed. However, it is assumed that the surface profile and phase function take the form of Eq. 3.5, which therefore yields the

following transmission function:

$$\begin{aligned} t(x) &= \exp[-i\phi_0]\exp[-i\phi_1\cos(k_1x)]\exp[-i\phi_2\cos(k_2x)] \\ &= \exp[-i\phi_0]\sum_{n=-\infty}^{\infty} i^n J_n(\phi_1)\exp[ink_1x]\sum_{m=-\infty}^{\infty} i^m J_m(\phi_2)\exp[imk_2x] \end{aligned} \quad (3.12)$$

Again assuming that expanding up to the second order is sufficient and using the trigonometrical relation, $\cos A\cos B = \frac{1}{2}[\cos(A-B)\cos(A+B)]$, yields an expression where diffraction angles, efficiencies, and phase shifts can be derived from,

$$\begin{aligned} t(x) \approx\ & 2J_2(\phi_1)J_2(\phi_2)\left[\cos\left(2(k_1-k_2)x\right)+\cos\left(2(k_1+k_2)x\right)\right] \\ -\ & 2iJ_2(\phi_1)J_1(\phi_2)\left[\cos\left((2k_1-k_2)x\right)+\cos\left((2k_1+k_2)x\right)\right] \\ -\ & 2iJ_1(\phi_1)J_2(\phi_2)\left[\cos\left((k_1-2k_2)x\right)+\cos\left((k_1+2k_2)x\right)\right] \\ -\ & 2J_1(\phi_1)J_1(\phi_2)\left[\cos\left((k_1-k_2)x\right)+\cos\left((k_1+k_2)x\right)\right] \\ -\ & 2J_2(\phi_1)J_0(\phi_2)\cos(2k_1x) - 2J_0(\phi_1)J_2(\phi_2)\cos(2k_2x) \\ +\ & 2iJ_1(\phi_1)J_0(\phi_2)\cos(k_1x) + 2iJ_0(\phi_1)J_1(\phi_2)\cos(k_2x) \\ +\ & J_0(\phi_1)J_0(\phi_2)\,. \end{aligned} \quad (3.13)$$

The diffraction angles and corresponding phase shifts are found from the expression above and are depicted in Fig. 3.12.

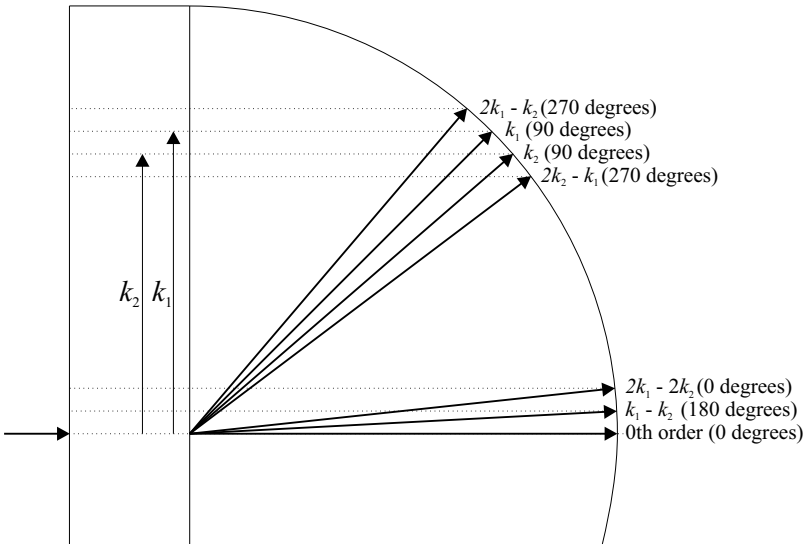

Figure 3.12: Expected diffraction orders and phase shifts for the double exposed HOE showing two main diffraction orders and two sidebands.

With the two different beams being diffracted in the HOE, one can observe interference in three points around the main diffraction order (see Fig. 3.14). It is seen from Fig. 3.12 and Eq. 3.13 that the interference signals from adjacent diffraction orders are expected to be 180 degrees shifted from each other. In other words, this does not explain what is actually observed. Therefore, we pursue a method in the following, where a third grating can introduce the quadrature phase signals.

3.2.5 Holographic Optical Element with Three Overlapping Gratings

We here pursue the hypothesis that small non-linearities in the manufacturing process of the HOE make the difference grating appear as a third grating as described in Eq. 3.6. In this case, the transmission function takes the following form:

$$\begin{aligned} t(x) &= \exp[-i\phi_0]\exp[-i\phi_1\cos(k_1x)]\exp[-i\phi_2\cos(k_2x)]\exp[-i\phi_3\cos(k_3x)] \\ &= \exp[-i\phi_0]\sum_{n=-\infty}^{\infty} i^n J_n(\phi_1)\exp[ink_1x]\sum_{m=-\infty}^{\infty} i^m J_m(\phi_2)\exp[imk_2x] \\ &\quad \sum_{l=-\infty}^{\infty} i^l J_l(\phi_3)\exp[ilk_3x]\,, \end{aligned} \tag{3.14}$$

where k_3 represents the difference grating. If making a second order expansion, and expanding the multiplied cosine-terms, a somewhat complicated expression with approximately 75 terms will result. However, only looking at the terms that will produce the same diffraction angles as shown in Fig. 3.12, then the transmittance function will be given by:

$$\begin{aligned} t(x) \approx\ & -2i\,J_2(\phi_1)J_1(\phi_2)J_0(\phi_3)\,(\cos((2k_1-k_2)x)+\cos((2k_1+k_2)x)) \\ & -\ 2J_1(\phi_1)J_0(\phi_2)J_1(\phi_3)\,(\cos((k_1+k_3)x)+\cos((k_1-k_3)x)) \\ & +\ 2i\,J_0(\phi_3)\,[J_1(\phi_1)J_0(\phi_2)\cos(k_1x)+J_0(\phi_1)J_1(\phi_2)\cos(k_2x)] \\ & -\ 2J_0(\phi_1)J_1(\phi_2)J_1(\phi_3)\,(\cos((k_2-k_3)x)+\cos((k_2+k_3)x)) \\ & -\ 2i\,J_1(\phi_1)J_2(\phi_2)J_0(\phi_3)\,(\cos((2k_2-k_1)x)+\cos((k_1+2k_2)x)) \\ & +\ 2J_2(\phi_1)J_2(\phi_2)J_0(\phi_3)\,(\cos(2(k_1-k_2)x)+\cos(2(k_1+k_2)x)) \\ & -\ 2i\,J_0(\phi_1)J_0(\phi_2)J_2(\phi_3)\cos(2k_3x) \\ & -\ 2J_1(\phi_1)J_0(\phi_2)J_0(\phi_3)\,(\cos((k_1-k_2)x)+\cos((k_1+k_2)x)) \\ & +\ 2i\,J_0(\phi_1)J_0(\phi_2)J_1(\phi_3)\cos(k_3x) \\ & +\ J_0(\phi_1)J_0(\phi_2)J_0(\phi_3)+\ldots \end{aligned} \tag{3.15}$$

The diffraction angles and phase shifts are depicted in Fig. 3.13.

It is seen that if the proper diffraction term is dominant then the adjacent diffraction beams can be shifted 90 degrees. That is, we would like the k_1+k_3, k_1, k_2, and k_2-k_3 orders to be dominant. Since the difference in incident angles for the light reflected from the two points of the object is matched with the difference grating, the four adjacent diffraction orders shown in Fig. 3.13 will cause interference at three position as shown in Fig. 3.14 and Fig. 3.5 (b).

As can be seen from Eq. 3.15 and Fig. 3.13, there will be two diffraction orders overlapping for every diffraction angle. The overlying diffraction orders are shifted 90 degrees in phase compared to each other. The measured phase will therefore depend on both diffraction orders and the phase will be biased towards the stronger of the two diffraction orders as can be seen from the following expression:

$$C_1\sin\theta + C_2\cos\theta = \sqrt{C_1^2+C_2^2}\,\sin\left(\theta+\arctan\frac{C_2}{C_1}\right)\,, \tag{3.16}$$

where C_1 and C_2 are the amplitudes of the two quadrature phase signals.

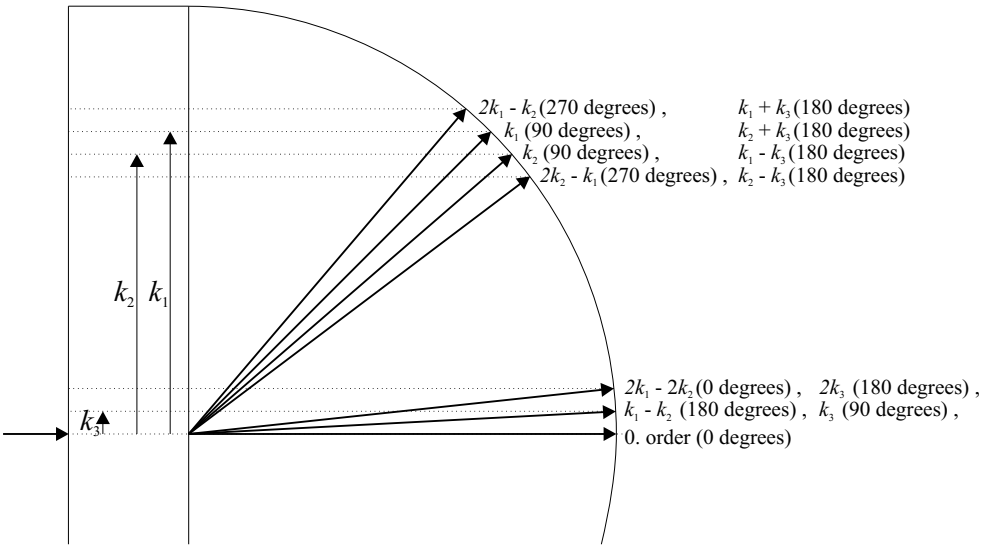

Figure 3.13: Expected diffraction orders and phase shifts if using the alternative approach to analysing the double exposed HOE.

3.2.6 Measurements

The purpose of these measurements is to estimate the sensitivity of the new system as well as determining the phase difference between the observed diffraction orders. The diffraction efficiencies of the 0th, 1st and 2nd order diffractions for the produced HOEs were measured with a

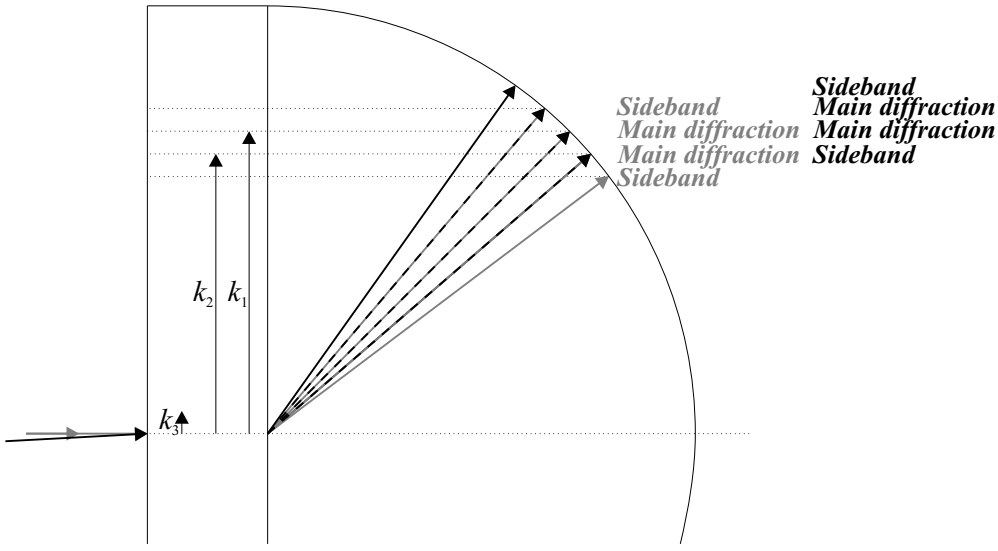

Figure 3.14: The main diffraction orders and sidebands for the two reflected beams will cause observable interference at three points in the observation plane.

power meter and by illuminating the HOEs with a collimated light source at an incident angle of 45 degrees at the design wavelength. The measured data can be seen in Tab. 3.1.

HOE no.	E_{max} [mJ/cm^2]	η_0 [%]	η_1 [%]	η_2 [%]
D.01	40	52.9	34.6	12.5
D.02	50	44.9	37.3	17.8
D.03	60	39.6	41.4	19.0

Table 3.1: The exposure energy and the corresponding measured relative diffraction efficiencies.

The sensitivity of the system is estimated by following the same procedure as described in Sec. 3.1. The sensitivity measured in the central diffraction order (see area G1 in Fig. 3.5) is measured to be approximately 0.3 nm for all the HOEs.

The measurements for estimating the phase difference between the observed interference signals were carried out in the following way. The interference signals are observed in three positions of the detector array (see Fig. 3.5 (b)). The object was tilted in fixed steps using the gimbal mirror mount, as described in Sec. 3.1. For each position, the average detector output of areas G1, G2, and G3, respectively, was calculated. The measurements all showed similar results to those depicted in Fig. 3.15.

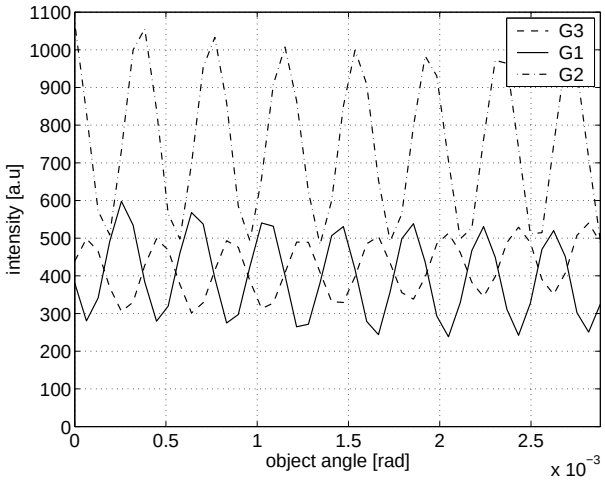

Figure 3.15: The measurements on D.02. using a mirror on a gimbal mount to introduce the angular displacement.

The measurements based on the different interference signals from hologram D.02 clearly show that the two sidebands, G2 and G3, are in anti-phase and that they are shifted ± 90 degrees from the central diffraction.

A sinusoidal fit was used on the measured interference signals in order to find the phase difference between the interference signals. The measurements for all the HOEs all showed that there is approximately a 90 degree phase shift between adjacent orders. The results are summed up in Tab.

3.2.

HOE no.	detector distance from beam splitter	$\Delta\phi_1$ [deg]	$\Delta\phi_2$ [deg]
D.01	2 cm	-88	95
D.01	3 cm	-90	85
D.01	4 cm	-89	85
D.02	3 cm	-90	90
D.03	3 cm	-94	91

Table 3.2: The constructed holograms and the corresponding measured phase differences from the centre interference signals, G1.

These results substantiate the hypothesis that the difference grating in fact does manifest itself as a third grating. In any case, the automatically provided quadrature signal ensures that a high sensitivity is obtained for the entire displacement range and also enables the use of some simple methods for determining the phase including the sign of the interference signal.

3.3 Displacement Sensor with Extended Measurement Range

This section describes a novel method that was devised in order to extend the measurement range of the differential displacement measurements. The results presented in the section was first presented in Ref. [50].

3.3.1 Measurement Range Extension Technique

The idea behind the measurement range extension technique utilises a common-path interferometer scheme. In fact, the technique we propose here utilises two common-path interferometers, since a laser beam is split into three beams and directed onto three points on an object surface; the 3 points being positioned on a straight line. The distances between probing points are denoted d_1 and d_2 as illustrated in Fig. 3.16, and the light beams reflected from two adjacent points are to be mixed and observed. The centre beam acts as a reference beam for the two adjacent beams, and the observed interference signals will consequently be a function of the optical path length difference between the centre beam and the two peripheral beams, respectively.

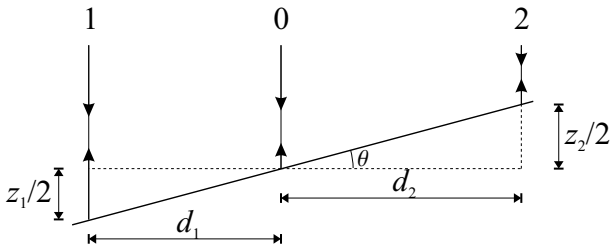

Figure 3.16: The common-path interferometer implemented to probe the angular displacement of mirror-like surfaces.

The measured interference signals, S_1 (obtained by mixing the reflected beams 1 and 0) and S_2 (obtained by mixing the reflected beams 2 and 0), will vary in the following way:

$$S_1 \propto \cos\left(\frac{2\pi}{\lambda} z_1 + \phi_{k1}\right) \approx \cos\left(\frac{4\pi}{\lambda}\theta d_1 + \phi_{k1}\right) \tag{3.17}$$

$$S_2 \propto \cos\left(\frac{2\pi}{\lambda} z_2 + \phi_{k2}\right) \approx \cos\left(\frac{4\pi}{\lambda}\theta d_2 + \phi_{k2}\right) \tag{3.18}$$

where z_1 and z_2 are the differences in optical path length between the reference beam and beam 1 and 2, respectively, λ is the wavelength, θ is the angular displacement of the object, and ϕ_{k1} and ϕ_{k2} are constant but arbitrary phase terms, which can be ignored in the following analysis. We will also introduce a parameter, M, that is simply the ratio between the optical path lengths z_2 and z_1,

$$M = \frac{z_2}{z_1}. \tag{3.19}$$

Fig. 3.16 shows an obvious application for the technique, namely the measurement of angular deflections of a mirror-like surface. In this application, one can see that the ratio M is given by the ratio between the distances, d_2 and d_1, between the probing points ($M = d_2/d_1$). If d_1 and d_2 are made slightly different, it is recognised that the two interference signals will change with different spatial frequency as shown in Fig. 3.17.

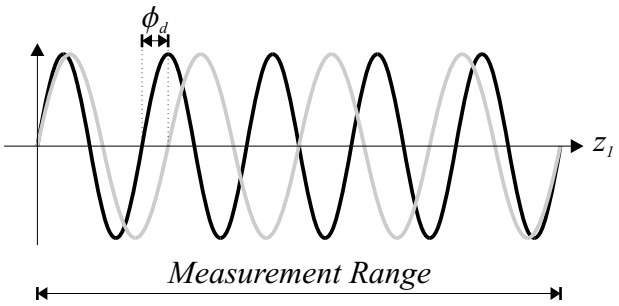

Figure 3.17: The obtained interference signals with different spatial frequencies. The fringe number can be calculated using the phase difference between the two signals, and the measurement range is defined as the range for which the phase difference between the two interference signals goes from 0 to 2π.

The phase difference between the two interference signals can then be used to make a rough assessment of the angular deflection, while the individual interference signals will provide the fine assessment. The phase difference, ϕ_d, between the two interference signals is found using Eq. (3.17)-(3.19) and is given by the following expression:

$$\phi_d = \frac{2\pi}{\lambda}|z_2 - z_1| = \frac{2\pi}{\lambda}|M - 1|z_1\,, \tag{3.20}$$

having neglected the constant phase terms. The obtained phase difference, ϕ_d, modulo 2π is equal to the phase that would have been obtained from a system using a wavelength Λ_{eff}. This in turn corresponds to the effective wavelength of the system, which is the range for which unambiguous measurements of the displacement can be performed. The effective wavelength can be found using

Eq. 3.20,

$$\begin{aligned} \frac{2\pi}{\Lambda_{eff}} z_1 &= \frac{2\pi}{\lambda} |M-1| z_1 \\ \Downarrow & \\ \Lambda_{eff} &= \frac{1}{|M-1|} \lambda \,. \end{aligned} \tag{3.21}$$

As mentioned above, the ratio, M, between z_2 and z_1 is given by $M = d_2/d_1$, yielding the following expression for the effective wavelength of the system for measuring angular deflections,

$$\Lambda_{eff} = \frac{d_1}{|d_1 - d_2|} \lambda \,. \tag{3.22}$$

Provided that the common-path interferometer can probe axial displacements between two points with a given sensitivity, then one can design the system to have a desired angular sensitivity and dynamic range, by fairly simple means. Increasing either d_1 or d_2 will increase the angular sensitivity, while the range for unambiguous measurements can be designed by changing the ratio between d_1 and d_2.

The technique is not necessarily restricted to the measurement of angular deflections alone and can easily be modified to probe other types of surface deflections as long as the ratio M can be properly defined, see Eq. (3.19) and (3.21).

Pressure Sensing

Consider for instance the case of pressure sensing, where the bending of a diaphragm depends on the magnitude of the lateral pressure, see Fig. 3.18. The deflection, z, of a circular diaphragm with fixed edges loaded with a uniform pressure is [51]:

$$z = z_0 \left(1 - \left(\frac{r}{a} \right)^2 \right)^2 \tag{3.23}$$

where a is the radius of the diaphragm, r the radial distance from the centre, and z_0 is the maximum deflection that occurs at the centre where $r = 0$.

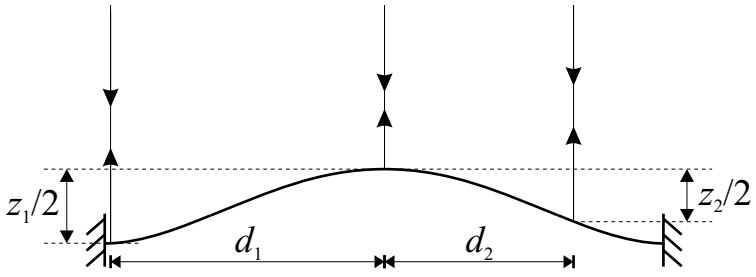

Figure 3.18: The technique applied to probing the deflection of a circular diaphragm.

The deflection of the diaphragm can be probed by using the common-path interferometer by for instance letting the reference beam probe the centre of the diaphragm, one of the peripheral beams

probing the rim of the diaphragm (at distance $r = d_1$) and the last beam probing a point somewhere between the centre and the rim (at distance $r = d_2$). By observing Fig. 3.18 and using Eq. (3.23) one can easily find the path lengths z_1 and z_2,

$$z_1 = z_0 \tag{3.24}$$

$$z_2 = z_0 - z_0\left(1 - \left(\frac{d_2}{d_1}\right)^2\right)^2 \tag{3.25}$$

From here it is straightforward to find the effective wavelength for this application, by inserting in Eq. 3.19 and 3.21,

$$\Lambda_{eff} = \frac{1}{\left(1 - \left(\frac{d_2}{d_1}\right)^2\right)^2}\,\lambda\,. \tag{3.26}$$

Two-wavelength Interferometry

A widely used method for making interferometric displacement measurements with displacements exceeding one wavelength is a two-wavelength Michelson interferometer.

The new method that we have devised has many resemblances to two-wavelength interferomfetry. Therefore, the new method is compared with this conventional method, in order to throw light on advantages and disadvantages of the method that we have devised.

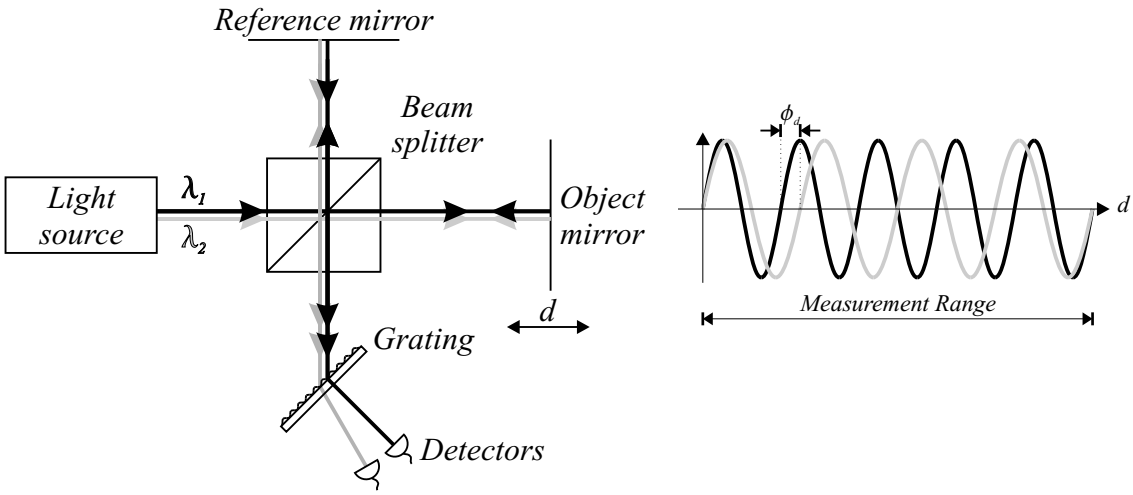

Figure 3.19: Two-wavelength interferometry based on a Michelson interferometer.

Similar to the approach that we have chosen, the phase difference between the two obtained interference signals obtained as the object is displaced with distance, d, can be used to make a rough estimate of the displacement while the individual interference signals can be used to make the fine estimation. The ratio between the obtained spatial frequencies of the interference signals will be given by the ratio between the applied wavelengths ($M = \lambda_1/\lambda_2$) and assuming an operating

wavelength $\lambda = \lambda_1$ then one obtains the following expression for the effective wavelength by inserting in the general expressing in Eq. 3.21,

$$\Lambda_{eff} = \frac{\lambda_1 \lambda_2}{|\lambda_1 - \lambda_2|} . \tag{3.27}$$

This is the well-known expression for the effective wavelength of two-wavelength interferometric systems [41]. If one wishes to design the system to a specific effective wavelength, then it is seen from Eq. 3.27 that one has to find two suitable wavelengths, which in some cases may prove difficult. It is thus more difficult to design a two-wavelength interferometer to have a desired sensitivity and measurement range compared to the method we propose, where only one wavelength is used and the sensitivity and measurement range is determined by the chosen geometry.

Objectives

Our objective is to verify the proposed technique for extending the measurement range of interferometric displacement measurements. In order to minimise uncertainties in the measurement technique, we therefore choose to implement the technique for measuring angular displacements, where the exact position of the reference beam is not as important as in the measurement of diaphragm deflections. We also choose to measure on specular surfaces (a mirror), so that uncertainties from surface variations are minimised.

The aim is to achieve a dynamic range of 1:10,000. Since the prior constructed common-path interferometer could probe differential displacements with a sensitivity of 0.5 nm (see Sec. 3.1), we choose to construct the system so that it can make an unambiguous measurement of differential displacements up to 5 μm. Due to the reflection setup, this means that the effective wavelength of the system has to be 10 μm.

The system uses an operational wavelength of 785 nm. This means that the desired range can be achieved by making the distances between two adjacent beams $d_1 = 1.2$ mm and $d_2 = 1.3$ mm, respectively, using Eq. (3.26).

3.3.2 The Optical System

An optical system was constructed in order to demonstrate the new measurement principle with the desired dynamic range. The optical system consists of a collimated laser diode, a multi-functional holographic optical element (HOE), and a photo diode array as shown in Fig. 3.20. The system expands upon the system described in Sec. 3.2 by introducing a third probing point (see also Fig. 3.5).

Once again, the central part of the constructed common-path interferometer is the HOE, which operates as both transmitter and receiver in the system. As for the case of the previous system, these two functions will be described separately.

Figure 3.20 (a) illustrates the function of the HOE, when operating as a transmitter. The laser light is collimated and illuminates the HOE at an angle of 45°. The only difference from the system described in Sec. 3.2 is that the HOE splits and focuses the light onto three point (instead of two) on the object surface.

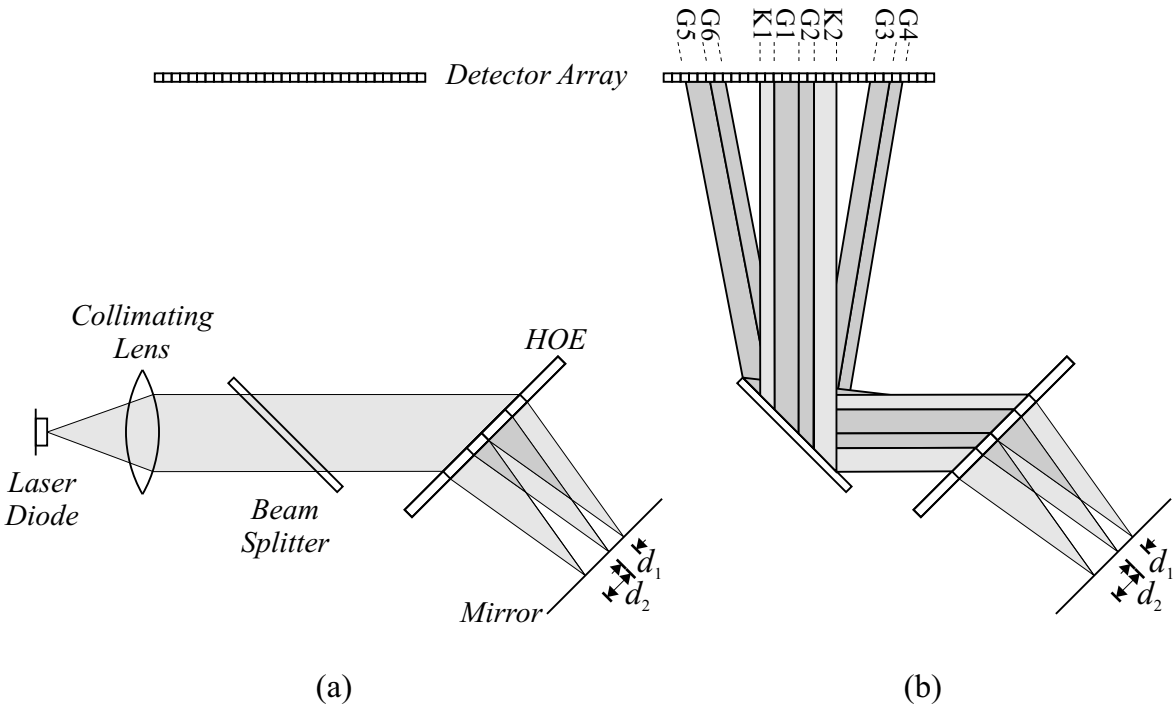

Figure 3.20: The setup for the common-path interferometer showing (a) the HOE when operating as transmitter in the system and (b) the HOE operating as receiver in the system.

The hologram is written as three partially overlapping lens elements, which are written sequentially using a 2.5 mm wide aperture. The focal length of the lens elements is 35 mm for the operation wavelength yielding a full width half maximum diameter of 8 μm in the focal plane (see also Fig. 3.21). Between the three exposures, the film is displaced 1.2 mm and 1.3 mm,

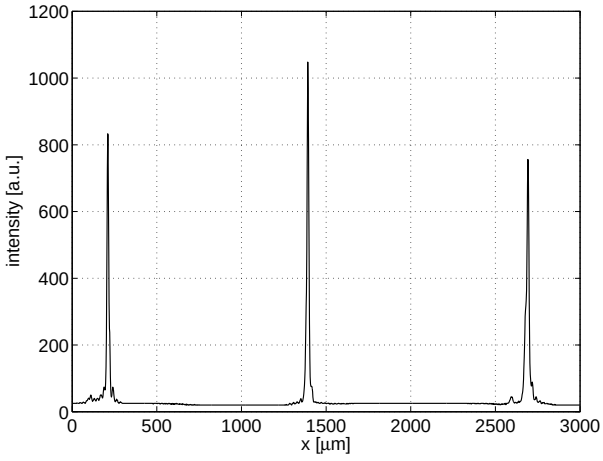

Figure 3.21: A beamscan of the measurement volume for the angular displacement sensor.

respectively. The total width of the HOE is therefore 5 mm. The angle of incidence is 45° and the diffracted beams are orthogonal to the HOE plane. Thereby, the alignment of the system as well as the writing process of the HOE are simplified, since the HOE and object plane should be parallel and all the lens elements have the same focal length. The light that is not diffracted by the HOE can easily be removed due to the large angular separation between diffraction orders. Additionally, the large diffraction angle ensures a high diffraction efficiency for the surface relief hologram. The applied diffraction order contains 44% of the total transmitted power.

Figure 3.20 (b) illustrates the function of the HOE, when operating as a receiver in the system. The light reflected from the three points on the object surface is collected by the HOE and diffracted in the opposite direction to the incoming laser beam (see also Fig. 3.20 (a)). Provided that the object is in the focal plane of the HOE lenses, the reflected or scattered light will be re-collimated by each of the three lens elements and via the beam splitter is sent to the detector array as parallel beams. Therefore, areas of the HOE where the lens elements are overlapping will cause co-propagating overlapping beams originating from adjacent points on the object surface. However, since there are two areas (as opposed to the system described in Sec. 3.2) where the lens elements are overlapping, one observes two different interference signals. Additionally, the phase quadrature signals from the sidebands that are automatically provided by the HOE are observed, which means that interference can be observed at six different areas on the detector array (see Fig. 3.20 (b)). The interference signals G5, G1, and G3 stem from the points separated by distance d_1 and G6, G2, and G4 stem from the points separated by distance d_2. The co-propagating beams ensure a good modulation depth of the interference signals and since the HOE both operates as transmitter and receiver, the system is self-aligning and stability is thus inherent in the HOE.

The test object (a mirror) is mounted on a gimbal mirror mount as described in Sec. 3.1. The rotation of the mirror induces an axial displacement between the adjacent points on the surface, and this displacement is probed by the common-path interferometer.

3.3.3 Measurements and Signal Processing

The system for the experimental verification of the tilt sensor concept is as illustrated in Fig. 3.20. The measurements were performed as static measurements for different angular positions of the mirror. The mirror was rotated in steps of 1.6×10^{-5} rad and in total 3.9×10^{-3} rad by translating a piezo transducer. For each step a detector scan was made with a linear detector array having 512 detectors with a centre distance of 25 μm, and from this scan the tilt angle of the object was calculated after a calibration of the system. The gimbal mirror mount was positioned so that the probing beams were close to the rotation axis. However, since the total range for the angular displacements for the measurement series is relatively small compared to the confocal parameter, which is measured to be 0.5 mm, the exact position does not have to be very accurate.

As already mentioned, there are six different areas (G1-G6) on the detector array where interference signals can be found. The intensities from these six areas are calculated as the mean value of the output from the detector pixels in the respective areas. The physical extent of the six areas varies from 0.75 mm to 1.3 mm. For instance, the two centre interference areas cover 0.85 mm and 0.93 mm (34 and 37 pixels), respectively. These sizes are as expected, considering the size of the overlap areas of the HOE and the diffraction angle. The areas are located at the same pixels

when the angle of the object is changed - at least within the angular displacement range of the presented measurements.

Changing the position of the detector array along the propagation path does not change the physical extent of the six areas; it merely changes the separation between the three diffraction groups, neither does the phase difference between the interference signals change. This shows that the beams are well collimated and that the object is placed in the focal plane of the three beams.

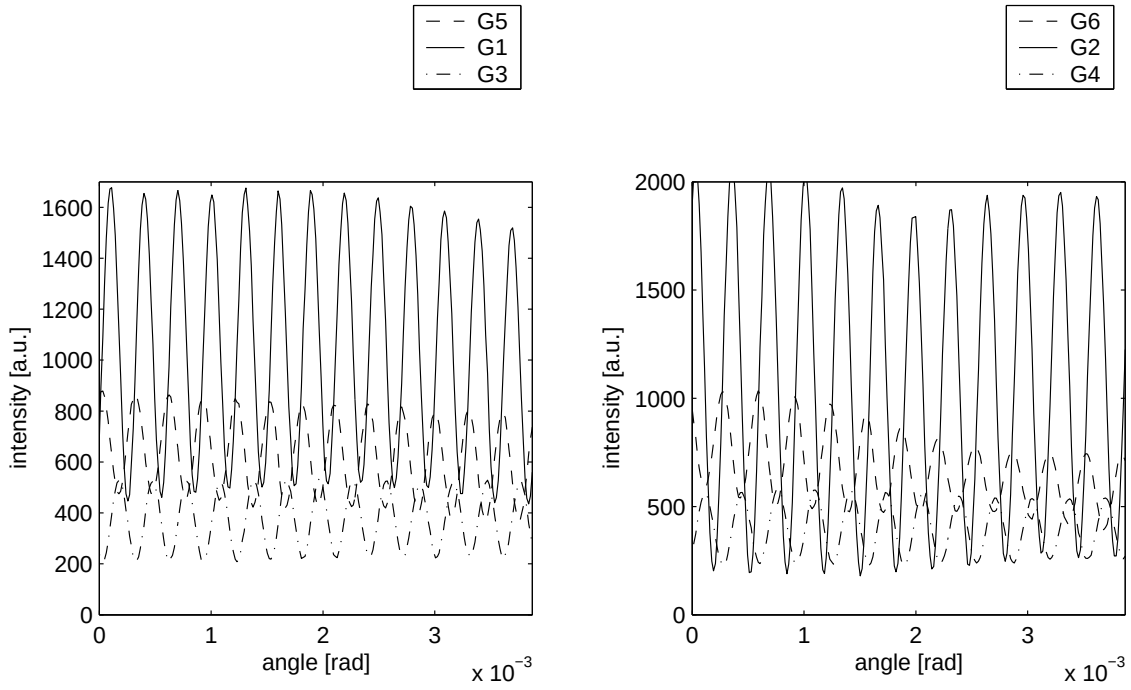

Figure 3.22: The measurements showing the mean detector output value of the three interference areas that are obtained by mixing the two beams separated by (a) distance d_1 and (b) d_2, respectively, as a function of the object angle.

Figure 3.22 (a) shows the mean detector output value of the three interference areas G1, G3, and G5 as a function of the object angle. These are the three interference signals obtained from mixing of the two beams separated by distance d_1. This plot shows the three phase shifted signals, however, it is seen that the system needs to be calibrated beforehand, since the interference signals do not have the same modulation depths and average intensities. Therefore, in the calibration process, the DC offset and scaling factor, which make the interference signals comparable in amplitude and average intensity, are found.

Figure 3.23 (a) illustrates the effect of this calibration. It shows that there is a $\pi/2$ phase difference between the signals, the interference signals from the two sidebands (G3 and G5) being shifted $\pm\pi/2$ from the centre signal (G1). It is seen from Fig. 3.23 (b) that similar graphs are obtained when plotting the interference signals from G2, G4, and G6. However, the spatial frequency of these interference signals are different, since these signals arise from mixing of the beams sepa-

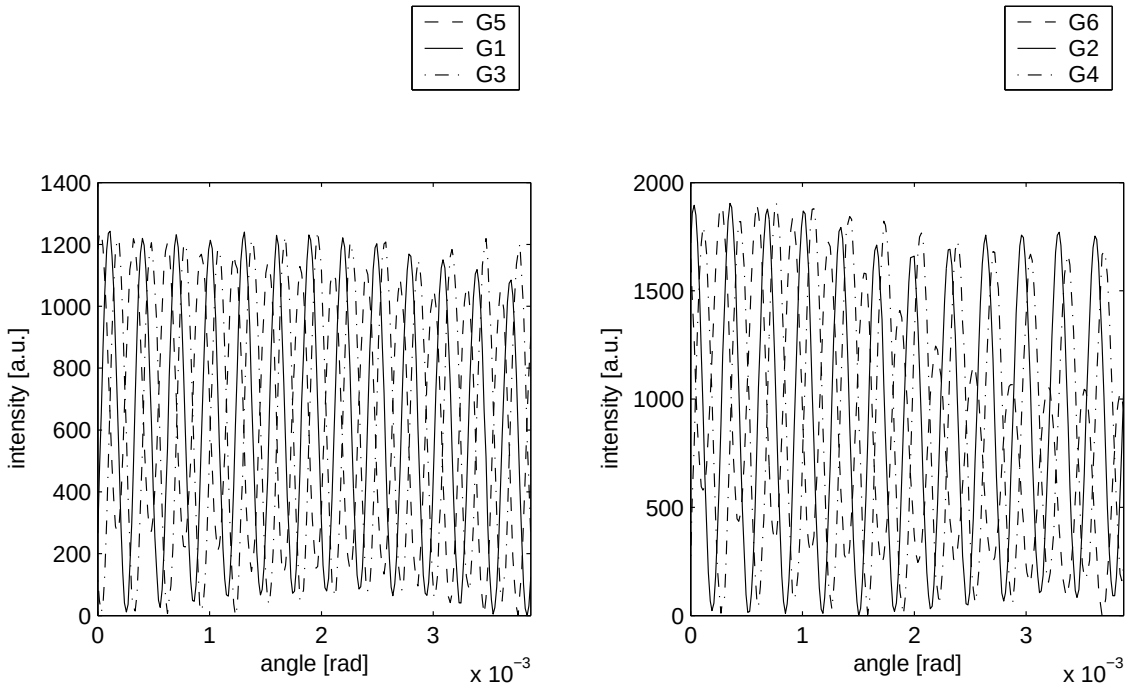

Figure 3.23: The interference signals after subtracting and scaling showing the effect of the calibration routine.

rated by distance d_2, which of course is desired.

In order to calculate the angular displacement, one needs to determine the phases of the two centre interference signals (G1 and G2). We use the phase of signal G1 as the fine estimation of the displacement, but one might as well have chosen to use G2. Since the interference signal has three unknown variables, namely the average intensity I_0, the modulation depth γ, and the phase ϕ_1, we need three phase shifted signals in order to make the calculation, which luckily is automatically provided by the HOE. Ideally, the three signals belonging to the interfocal distance, d_1, would have identical average intensities and modulation depths,

$$\begin{aligned} I_{G1} &= I_0\,(1+\gamma\cos\phi_1) \\ I_{G3} &= I_0\,(1+\gamma\cos(\phi_1+\pi/2)) \\ I_{G5} &= I_0\,(1+\gamma\cos(\phi_1-\pi/2))\ , \end{aligned} \tag{3.28}$$

by which conventional techniques such as the *3-bucket technique* could be used to determine the phase [52]. However, if one observes Fig. 3.23 (b), it is seen for instance that the modulation depth of G6 varies significantly over the range displayed. Using this signal could therefore introduce an error, when making the phase calculation. Therefore, we instead deploy a variation of the *2+1 algorithm* [53], where only two of the interference signals are used. The phase is then given by:

$$\phi_1 = \arctan\left(\frac{I_{G1}-I_{G3}}{(I_{G1}+I_{G3}-2I_0)\tan(\varphi/2)}\right)\ , \tag{3.29}$$

where $I_0 = (\overline{I_{G1}} + \overline{I_{G3}})/2$ is the average intensity, the overline denoting the average intensity over the entire dynamic range, and φ is the phase difference between the two applied interference signals. The average intensity, I_0, is found during the afore-mentioned calibration routine. By making simple observations of the sign of the nominator and denominator of Eq. (3.29), a modulo 2π phase calculation can easily be made. A similar calculation of the phase, ϕ_2, using the signals I_{G2} and I_{G4} is made. The calculated phases of the two interference signal groups are shown in Fig. 3.24 and it can be seen that the slopes of the two phases as a function of the angular displacement differ, as is desired.

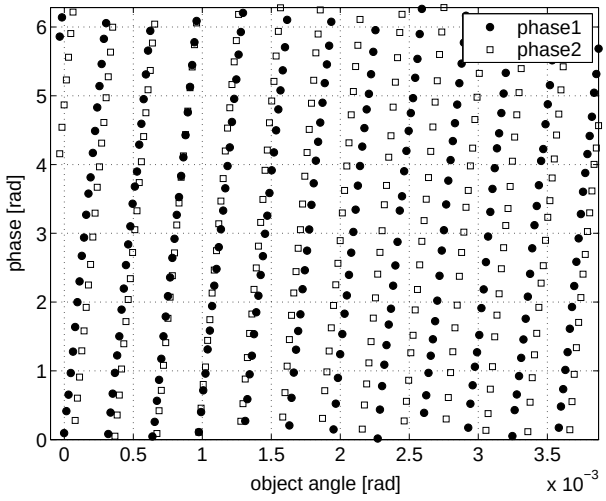

Figure 3.24: Calculated phases of the interference signals corresponding to the two interfocal distances d_1 and d_2, respectively.

The phases, ϕ_1 and ϕ_2, of the two interference signals (belonging to the interfocal distances d_1 and d_2, respectively) have now been calculated. Subsequently, the phase difference (modulo 2π), ϕ_d, between the two signals is calculated and is shown in Fig. 3.25.

The phase difference is used to calculate the actual fringe number of the interference signals. In other words, the phase difference is used to make a first rough estimate of the differential displacement or tilt. Ideally, the phase difference would follow a linear curve, which would make the fringe calculation simple. However, if one observes Fig. 3.25, it is seen that measurements are not so ideal. In fact, it can be seen that the phase difference is not even monotonously increasing. Therefore, we deploy a simple fringe determination algorithm, in order to reduce the probability of faulty calculation of the fringe number. The phase difference, ϕ_d, is divided into N intervals, where N is the number of fringes within the measurement range, i.e., the ratio between the effective wavelength, Λ_{eff}, and the operating wavelength λ.

First, the phase, ϕ_1, is probed. Based on whether ϕ_1 is smaller or larger than π, the phase difference, ϕ_d, will be shifted $\pm 2\pi/4N$ (a quarter of a fringe). The fringe number, m_1, is therefore

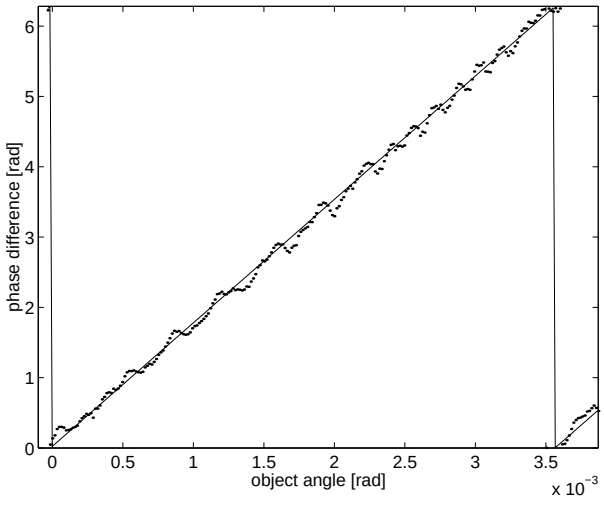

Figure 3.25: Calculated phase difference between the two interference signals, corresponding to the two interfocal distances d_1 and d_2, respectively.

found using the following expression:

$$m_1 = \begin{cases} \left\lfloor \frac{\left(\phi_d + \frac{2\pi/N}{4}\right) \bmod 2\pi}{2\pi/\mathrm{N}} \right\rfloor & \text{for} \quad 0 \leq \phi_1 < \pi \\ \left\lfloor \frac{\left(\phi_d - \frac{2\pi/N}{4}\right) \bmod 2\pi}{2\pi/\mathrm{N}} \right\rfloor & \text{for} \quad \pi \leq \phi_1 < 2\pi \end{cases} \tag{3.30}$$

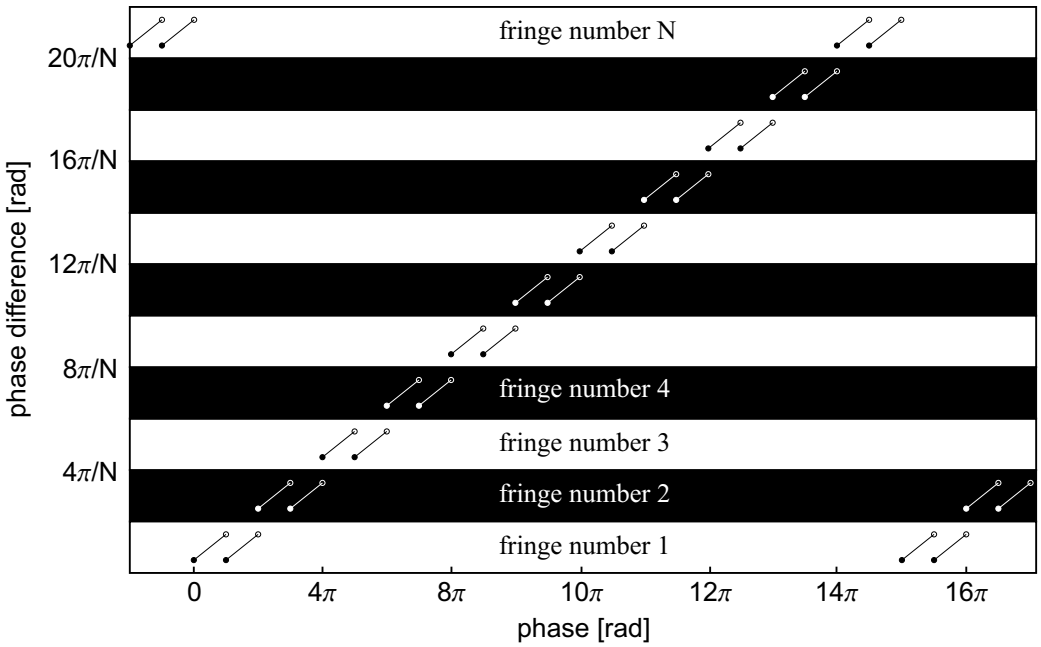

Figure 3.26: Illustration of the fringe count algortithm depicted for a measurement range of 11 fringes ($N = 11$) as a function of the unwrapped phase under ideal conditions.

where $\lfloor . \rfloor$ denotes the floor-function. It is readily seen that the expression is a peridodic step-function with N numbers of steps as a function of the phase difference, ϕ_d. Using the algorithm shown in Eq. (3.30) allows for a certain margin of error for the calculated phase difference as can be seen from Fig. 3.26. The fringe numbers calculated from the measurements are shown in Fig. 3.27 and it is seen that it has the desired staircase shape without any errors.

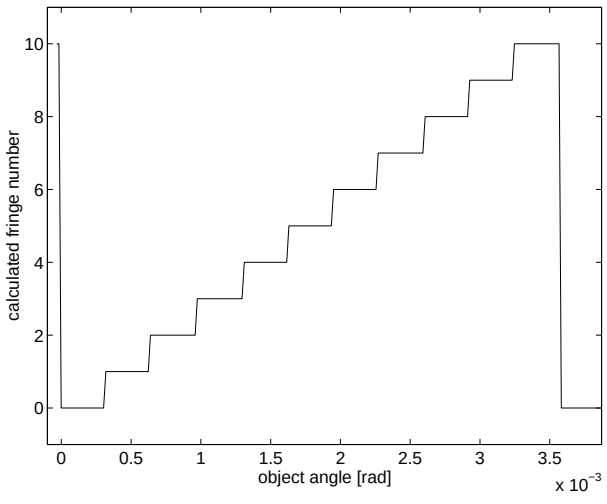

Figure 3.27: The calculated fringe numbers having the desired staircase shape as a function of the object angle.

Having determined the fringe number, m_1, and knowing that the period of the interference signals corresponds to a displacement of $\lambda/2$, it is straight forward to calculate the differential displacement Δz_1,

$$\Delta z_1 = \left(m_1 + \frac{\phi_1}{2\pi} \right) \frac{\lambda}{2} , \tag{3.31}$$

and converting this into an angular displacement is trivial, since the distances, d_1 and d_2, between the foci are known. These are more precisely determined to be $d_1 = 1.20$ mm and $d_2 = 1.31$ mm by doing a beam scan in the focal plane (see Fig. 3.21). Having applied the afore-mentioned calibration routine and Eq. (3.29)–(3.31), the actual angle can be determined in real-time from the detector scan. The angles measured can be seen in Fig. 3.28 and it is noticed that the measurements follow a linear graph as expected. The effective wavelength for which an absolute measurement can be made, corresponds to the displacement of approximately 11 interference fringes, or equivalently a differential displacement of approximately 4.3 μm.

The sensitivity of the system has been estimated by collecting data for a long period for each measurement position. The standard deviation of the measurements of the two centre interference signals (G1 and G2) shows that the system for these static measurements has a signal-to-noise ratio of 600. This means that the system can probe differential displacements with a sensitivity of approximately 0.3 nm on specular surfaces and has proven to be even more sensitive than the earlier common-path interferometer (see Sec. 3.1). The sensitivity of the interference signals is of course lower at the deflection tangents of the sine-signal, but since the phase quadrature signal is provided automatically by the HOE, the sensitivity at these positions is maintained. This means

that the angular sensitivity of the system in its present configuration is approximately 2.5×10^{-7} rad. The range for unambiguous measurements for the system is larger than 3.5×10^{-3} rad, i.e. the dynamic range can be divided into approximately 14,000 sampling areas.

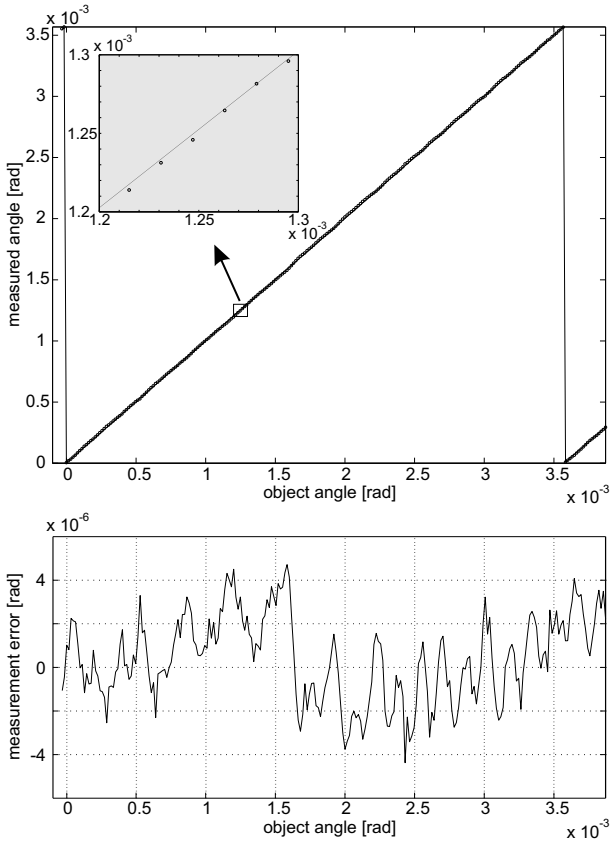

Figure 3.28: The measured differential tilt angle of the object compared to the angle of the gimbal mirror mount. The grey-tinted inset shows a magnification of a part of the plot.

The accuracy or reproducibility of the system, however, is another matter entirely. Since small variations in modulation depth, average intensity, or even the phase of the interference signals are almost inevitable, it is difficult to obtain a system, where the accuracy is comparable to the sensitivity. It is seen from Fig. 3.28 that the measurement error approaches a factor 18 greater than the sensitivity of the system.

3.3.4 Discussion

One of the main advantages of the system presented is that it provides a simple and all passive measurement of phase stepped signals. Another advantage compared to two-wavelength interferometry is that the interference signals with different spatial frequencies are obtained using only one light source (and wavelength). However, one of the main problems of the present system and the signal processing, is the slight variations of average intensity and modulation depth for the individual interference signals. These variations introduce errors, when making the phase calculations. An active phase stepping method (for instance a movable reference mirror in a two-wavelength Michelson interferometer) might be advantageous in this respect, since the phase quadrature sig-

nals provided here comes from the same interference signals and the change in the variables of the phase stepped signals will probably be smaller.

We also stated that one of the advantages of applying the technique for angular displacement measurements is that the angular sensitivity and measurement range can easily be designed by choosing the proper interfocal distances, d_1 and d_2. However, one should be aware that increasing the measurement range makes increasing demands on the precision of the phase calculation. An increase in the number of fringes within the measurement range means that the phase difference will be divided into more intervals, see Eq. (3.30) and Fig. 3.26. The maximum deviation from the fitted curve allowed decreases proportionally with this increase. In the measurements presented here, it is seen that the deviations of the phase difference, ϕ_d, from the fitted curve are quite large (see Fig. 3.25). This means that we would not be able to extend the measurement range much further than to the 11 fringes that we did, since this would result in faulty fringe number calculations. This type of error will be quite severe.

It must be noted that the system relies on using the specularly reflected light from the surface. Consequently, a finite surface roughness will inevitably reduce the specular component and increase the diffusely scattered. The latter will give an insignificant contribution to the measured signal, while the decrease in the specular part will be proportional to $\exp[-4k^2\sigma_{rms}^2]$ where k is the wave number and σ_{rms} is the surface roughness [54]. Furthermore, the variations in surface slope must be small so that the specularly reflected light does not miss the HOE entirely.

It is clear that in order to overcome the afore-mentioned problems, an optimisation of the system has to be carried out. Especially, if the system is to be used for measurement on rough surfaces, where the variations between the individual interference signals become quite prominent. Initiatives to improve the quality of the interference signals could for instance be to make dedicated apertures for the six signal groups and instead use focusing lenses and separate detectors. Another issue that could be interesting to examine is to vary the depth of the gratings in order to change the energy distribution between the main diffraction orders and the sidebands. This might improve the quality of the interference signals.

However, these initiatives might show that the signal quality cannot be improved enough to use the *3-bucket* or even the *2+1 algorithm* in order to improve the accuracy of the system. Perhaps new algorithms have to be developed, or using look-up tables might prove to be a better method to improve the accuracy.

3.4 Impulse Response Function in Common-Path Interferometers with Fourier Plane Filters

Along with the process of developing the methods for pressure sensing, we also explored other methods than the ones described in the previous sections of this chapter. Amongst other things we explored the use of diffractive optical elements placed in the Fourier plane of a 4-f setup. This work is purely theoretical and has not yet been demonstrated in practice. The work was originally presented in Ref. [55] and later in Ref. [56].

3.4.1 Introduction

Speckle shearing interferometry or *shearography* is a well-known method for measuring the first derivative of deflections for rough surfaces, which combined with electronic speckle interferometry (ESPI) makes it possible to obtain real-time correlation fringes on a monitor [57].

A typical approach in shearography is to illuminate an object with coherent light and observe the scattered light through a Michelson-type interferometer, where one of the mirrors has a slight incline, the size of the incline determining the size of the shear. The introduction of a holographic grating as the shearing element can yield advantages in respect to light efficiency, simplicity and cost efficiency [58–61]. Holographic optical elements (HOE) can also provide compact and self-aligning systems for other types of interferometers, such as electronic speckle interferometry systems (ESPI systems) or vibrometers [35], and displacement sensors as the ones presented earlier in this chapter.

We introduce here a system that can facilitate an arbitrary type of common-path interferometer and with the proper design of the HOE can measure a desired type of surface deformation. The optical setup is a 4-f system with an HOE placed in the Fourier plane as illustrated in Fig. 3.29.

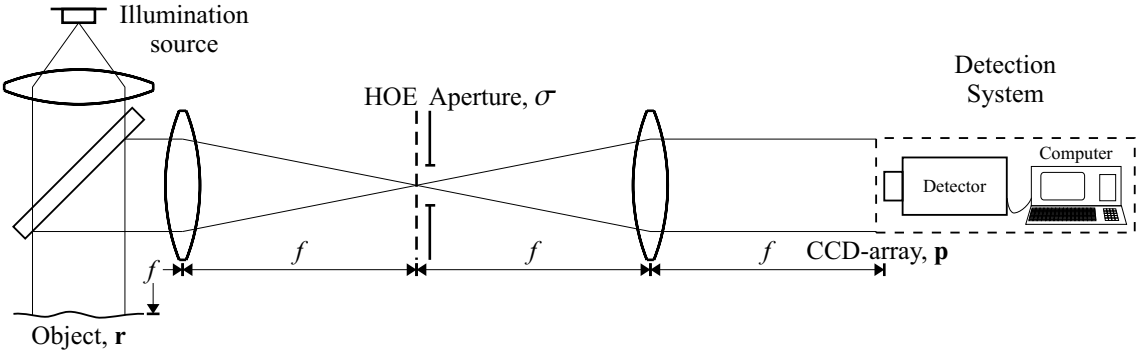

Figure 3.29: The 4-f setup for measuring surface deflections, tilt or vibration. f is the focal length of the two lenses, and **r** *and* **p** *are the position vectors in the object and observation plane, respectively.*

It is here assumed - for the sake of simplicity - that the object is illuminated with coherent light in a backscattering mode and that the system without the Fourier filter makes up an imaging configuration. Furthermore, it is assumed that the HOE divides the incident light into two fields with comparable strength and these fields interfere in the observation plane (at the CCD-array). To ensure fully developed speckle it is additionally assumed that the surface roughness is large compared to the wavelength and that the illuminating spot size exceeds any lateral surface roughness scale [54].

The correlation fringe pattern is viewed by subtracting the speckle pattern recorded with the object in the undeformed state from the speckle pattern after a deformation of the object surface has taken place, which results in the following average intensity distribution on the monitor:

$$\Pi(\mathbf{p}) = \left\langle \left(I(\mathbf{p}) - I'(\mathbf{p}) \right)^2 \right\rangle = \Pi_{DC}(\mathbf{p}) + \Pi_{int}(\mathbf{p}) \tag{3.32}$$

where Π_{DC} is a DC term and Π_{int} is an interference term. The interference term, which is that of

interest, is given by the following correlation:

$$\Pi_{int}(\mathbf{p}) = \mathrm{Re}\left\{\left\langle U_0(\mathbf{p})U_0'^{*}(\mathbf{p})\right\rangle\left\langle U_1^{*}(\mathbf{p})U_1'(\mathbf{p})\right\rangle\right\} \tag{3.33}$$

where subscripts 0 and 1 denote the undiffracted and diffracted fields, respectively, the prime indicates the fields after deformation, the square brackets denote an ensemble average, and Re{.} denotes the real part. It is seen that the interference is given by the correlation between the fields before and after deformation of the object surface.

The fields are analysed using the paraxial approximation of the Huygens-Fresnel principle utilising the $ABCD$-matrix formalism for the system and introducing soft (Gaussian) apertures [62]. The Green's function connecting the optical field leaving the object plane with the field in the observation plane without the Fourier plane filter takes the following form:

$$G(\mathbf{r},\mathbf{p}) = \frac{k^2\sigma}{4\pi f}\exp\left[-\frac{(\mathbf{r}+\mathbf{p})^2}{\omega^2}\right] \quad , \omega^2 = \left(\frac{2f}{k\sigma}\right)^2\left(1 - i\frac{k\sigma^2}{2f^2}\Delta\right) \tag{3.34}$$

where σ is the $1/e^2$ intensity radius for the aperture in the Fourier plane and Δ describes an optional slight defocus of the 4-f system, viz. the offset of the target from the exact image plane.

The scattered optical field from the object can be expressed as:

$$U(\mathbf{r},t) = \sqrt{I(\mathbf{r})}\Psi(\mathbf{r},t) \tag{3.35}$$

where $\Psi(\mathbf{r},t)$ is the complex reflection coefficient with a random phase introduced by the rough surface of the object. The scattered field from the object is connected to the detected field through the two Green's functions:

$$U_i(\mathbf{p}) = \int_{-\infty}^{\infty} d\mathbf{r}\, G_i(\mathbf{r},\mathbf{p})U(\mathbf{r}) \quad , i = \{0,1\}\,, \tag{3.36}$$

where the scattered field, $U(\mathbf{r})$, is given by Eq. 3.35 and the subscript, i, denotes the unperturbed and perturbed fields, respectively.

Having assumed that the surface gives rise to fully developed speckle and assuming a reflection coefficient of unit magnitude yields the following expression for the correlation of two reflection coefficients:

$$\left\langle \Psi(\mathbf{r_1},t)\Psi^{*}(\mathbf{r_2},t)\right\rangle = \left(\frac{4\pi}{k^2}\right)\delta(\mathbf{r_1}-\mathbf{r_2}) \quad , \ |\Psi(\mathbf{r_1},t)| = 1\,, \tag{3.37}$$

where the factor $4\pi/k^2$ accounts for the object acting as a Lambertian source. It is assumed that the displacement between the two recordings is very small and consists only of a simple out-of-plane movement perpendicular to the object plane, by which the following expression relating the phase functions before and after displacement is obtained:

$$\Psi(\mathbf{r},t_2) = \Psi(\mathbf{r},t_1)\exp\left[-2ik\Delta z_{12}(\mathbf{r})\right] \tag{3.38}$$

where $\Delta z_{12}(\mathbf{r}) = h(\mathbf{r},t_2) - h(\mathbf{r},t_1)$ is the local shift in axial position of the object surface between the recordings. We tacitly assume a backscattering optical system, hence the factor 2 in the expression that accounts for the reflection setup.

3.4.2 Tilt Measurement

In order to keep things simple, we start by presenting a shearing interferometer, which is to be used to measure change in tilt, following the guidelines described earlier in this section. The shearing interferometer works such that light from two points on the object surface is collected by the optical system and interferes at a point in the detector plane as illustrated in Fig. 3.30. Thereby the system is sensitive to tilt along the axis between the two points.

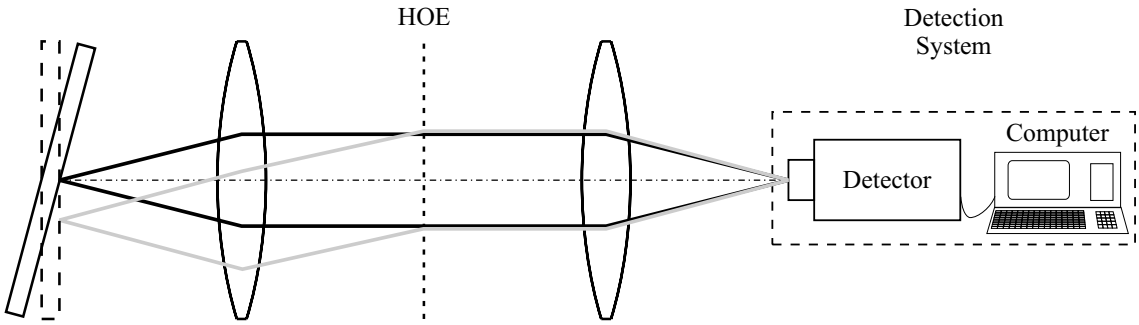

Figure 3.30: The receiver part for measuring tilt.

In this 4-f system, the shear can be obtained by letting the HOE be a conventional grating with suppressed 1st or -1st order diffraction. The Green's functions for the diffracted and undiffracted fields thereby take the following form:

$$G_0(\mathbf{r},\mathbf{p}) = -\frac{ik\kappa_0}{2\pi B_0}\exp\left[-\frac{(\mathbf{r}+\mathbf{p})^2}{\omega^2}\right] \tag{3.39}$$

$$G_1(\mathbf{r},\mathbf{p}) = -\frac{ik\kappa_1}{2\pi B_1}\exp\left[-\frac{\left(\mathbf{r}+\mathbf{p}-\hat{\mathbf{x}}\frac{f\alpha}{k}\right)^2}{\omega^2}\right], \tag{3.40}$$

where G_0 denotes the Green's function for the imaging system, or the 4-f system without the HOE, while G_1 denotes the Green's function for the diffracted field. B_0 and B_1 are the B-elements from the system matrices for the undiffracted and diffracted beam, respectively. ω is the resolution of the optical system, while κ_0 and κ_1 denote the transmission coefficients for the diffracted and undiffracted fields, respectively, k is the wave number and f the focal length of the lenses. $\hat{\mathbf{x}}$ denotes that the shear occurs along the x-axis. If we look at G_1, it is seen that the "shear" is determined by the grating constant, α, and the applied wavelength.

The important term of Eq. 3.32 is the interference term. In order to derive an expresson for the interference term, the correlations of the unperturbed field before and after deformation of the

object as well as for the perturbed field are needed,

$$\langle U_0(\mathbf{p})U_0'^{*}(\mathbf{p})\rangle = \frac{P_0\kappa_0^2\sigma^2}{2f^2\pi r_s^2}\exp\left[-\frac{2(p_x^2+p_y^2)}{r_s^2}\right]\exp\left[-2ikh_0\right]\exp\left[2ik\left(h_x' p_x + h_y' p_y\right)\right] \exp\left[-\frac{2f^2(h_x'^2+h_y'^2)}{\sigma^2}\right] \quad (3.41)$$

$$\langle U_1^*(\mathbf{p})U_1'(\mathbf{p})\rangle = \langle U_0(\mathbf{p})U_0'^{*}(\mathbf{p})\rangle^* \left(\frac{\kappa_1}{\kappa_0}\right)^2 \exp\left[-\frac{2f^2\alpha^2 - 4fk\alpha p_x}{k^2 r_s^2}\right]\exp\left[2if\alpha h_x'\right]. \quad (3.42)$$

where the subscripts x and y denote the vector components along the x- and y-axes, respectively, in the object and detector planes, r_s is the spot radius on the object, P_0 is the power of the applied light source, and h' denotes the first derivative.

The interference term is then found using Eq. 3.33 multiplying the two correlation terms,

$$\Pi_{int}(\mathbf{p}) = \left(\frac{P_0\kappa_0\kappa_1\sigma^2}{2f^2\pi r_s^2}\right)^2 \exp\left[-\frac{4(p_x^2+p_y^2)}{r_s^2}\right]\exp\left[-\frac{4f^2(h_x'^2+h_y'^2)}{\sigma^2}\right] \exp\left[-\frac{2f^2\alpha^2}{kr_s^2}\right]\exp\left[\frac{4f\alpha p_x}{kr_s^2}\right]\cos\left(2f\alpha h_x'\right). \quad (3.43)$$

Taking a closer look at the interference term, it is again seen that this is proportional to the grating constant of the filter and also the focal length of the system. But more importantly, it is also proportional to the tilt h_x' of the surface. The detected signal is insensitive to common vibrations due to the nature of common-path interferometers, and also insensitive to wavelength fluctuations, since the size of the shear is linearly proportional to the wavelength, and the optical path difference thereby is constant for a given change in object angle.

3.4.3 Curvature Interferometer

Let us now consider an example where the interferometer is to be used to measure change in curvature, for example the deflection of a circular diaphragm as in the use of pressure sensing. We design the HOE so that light from the centre of the diaphragm interferes with light collected from a circular ring at the edge, as illustrated in Fig. 3.31. The light collected from the edge of the diaphragm thus constitutes a reference wave for the light scattered from the center of the diaphragm.

The two Green's functions for the propagation of the undiffracted and diffracted fields, respectively, thereby take the following form:

$$G_0(\mathbf{r},\mathbf{p}) = \frac{k^2\kappa_0\sigma}{4\pi f}\exp\left[-\frac{(\mathbf{r}+\mathbf{p})^2}{\omega^2}\right] \quad (3.44)$$

$$G_1(r,p) = \frac{k^2\kappa_1\sigma}{4\pi f}\exp\left[-\frac{(r+p-R_0)^2}{\omega^2}\right] \quad (3.45)$$

where G_0 describes the imaging system and G_1 describes the propagation of light from an annular part of the object with radius R_0 and width ω to the on-axis position in the observation plane. κ_0

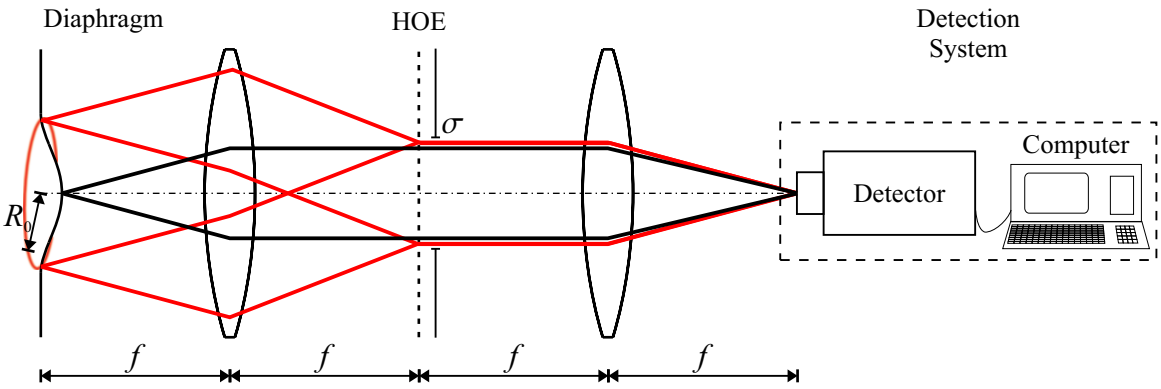

Figure 3.31: The receiver part of the interferometer for measuring curvature.

and κ_1 denote the diffraction efficiencies for the unperturbed and perturbed optical fields, respectively.

In order to find an expression for the interference term of Eq. 3.32, one has to go through the steps as described in the shearing interferometer. The calculations, however, are somewhat more painful for the curvature interferometer, so we will only present the final result. We assume that the surface curvature gives rise to a pure axial displacement, i.e. $\Delta z_{12} = \alpha r^2 + \vec{\beta} \cdot \mathbf{r} + \gamma$, and the important contribution to the interference pattern is found from the two essential terms of Eq. 3.32. Provided that the spot size, r_s, on the target is much larger than the diffraction limit of the system, i.e. $r_s^2 \gg (2f/k\sigma)^2$ and that the change in curvature is very small, $\alpha^2 \ll \left(k^2\omega^4\right)^{-1}$, then one obtains the following relation for the on-axis contribution:

$$\Pi(0) \propto I_{res}\left(1 + M\cos\left(2kR_0^2\alpha\right)\right) \tag{3.46}$$

where I_{res} is the average intensity and M is the modulation depth of the interference pattern.

The system is seen to be insensitive to a common translation of the object due to the common-path setup and is also insensitive to object tilt, since the phase contribution is cancelled out due to the circular symmetry of the system. The system is therefore seen to be sensitive to change in curvature only.

3.4.4 Impulse Response Function

An intuitive way of depicting the effect of an arbitrary HOE placed in the Fourier plane of the ESPI or vibrometer system will be given next. The purpose is not only to familiarise the user of interferometers with the interferometers presented, but also to provide a tool for conceiving new common-path interferometers.

It is intuitively recognised that any shearing-type ESPI-system will subtract the phase change due to an axial translation of the object from the phase change occurring at a given lateral distance (i.e. “the shear”) from the first position. Thus the system is generally considered to measure the change in slope of the object between the two exposures, i.e. the first derivative. The area over

which the axial displacement is averaged is given by the resolution of the optical system, ω.

Pursuing this idea, we can establish the following function, here named the impulse response function (IRF), $\Omega(\mathbf{r_0})$, of the optical system referred to the object plane. We assume that the filter is placed exactly in the Fourier plane, which results in the effect from the IRF being translationally invariant. Furthermore, - for the sake of simplicity - we assume the system to work in a backscattering mode, i.e. we only consider and probe axial translations, $\Delta z(\mathbf{r_0})$.

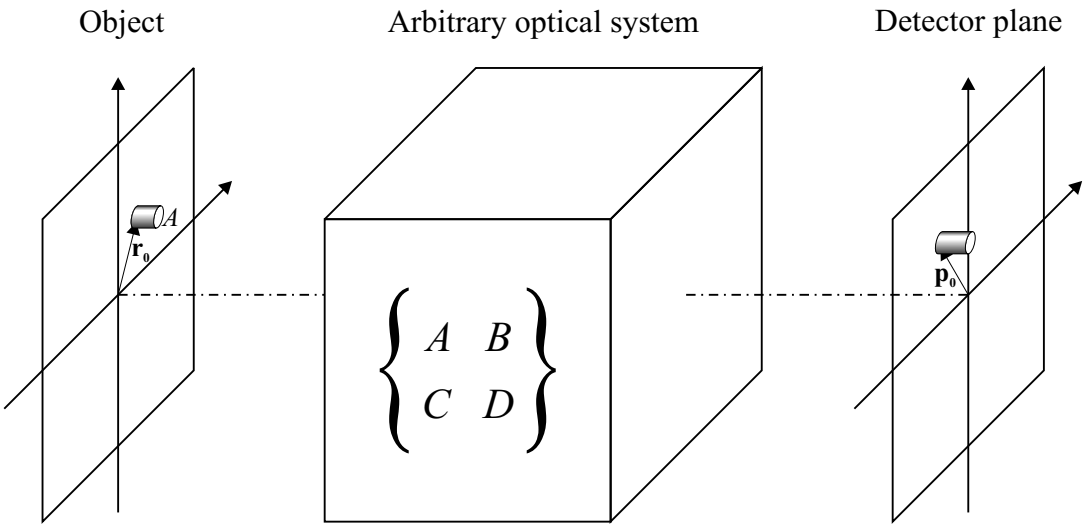

Figure 3.32: Illustration of the impulse response function. The system is affected by a piston-like deflection in the z-direction at $\mathbf{r_0}$ *and the effect is observed in the observation plane at* $\mathbf{p_0}$.

The IRF is defined as the phase change, $\Delta\varphi_{out}(\mathbf{p_0})$, in the detector plane due to a small change of phase, $\Delta\varphi_{in}$, at $\mathbf{r_0}$ in the object plane over a small area A, consequently the units for the IRF is m^{-2}. The expression for the IRF are as follows:

$$\Omega(\mathbf{r_0},\mathbf{p_0}) = \lim_{\{A,\Delta\varphi_{in}\}\to\{0,0\}} \left\{ \frac{\Delta\varphi_{out}(\mathbf{p_0})}{A\Delta\varphi_{in}(\mathbf{r_0})} \right\} . \tag{3.47}$$

If we observe the response at an arbitrary point, $\mathbf{p_0}$, in the observation plane and let $\mathbf{r_0}$ vary over the entire object plane, the IRF depicts the sensitivity of the entire system referred to the object plane.

The field incident on the Fourier plane filter is divided into two fields, which in the object plane are denoted U_0 and U_1 for the undiffracted and diffracted fields, respectively.

The complex reflection coefficient is assumed to be delta-correlated in input-space due to the assumption of fully developed speckle. The relation between the reflection coefficient before and after the phase change at $\mathbf{r_0}$ can then be written:

$$\left\langle \Psi(\mathbf{r_1})\Psi'^{*}(\mathbf{r_2}) \right\rangle = \frac{4\pi}{k^2}\delta(\mathbf{r_1}-\mathbf{r_2})\,(1 + A\exp[-i\,\Delta\varphi_{in}]\delta(\mathbf{r_1}-\mathbf{r_0}) - A\,\delta(\mathbf{r_1}-\mathbf{r_0})) \tag{3.48}$$

We can now calculate the interference term of Eq. 3.33, which is the dynamic term of the expression of Eq. 3.32, by using the proper Green's functions (see Eq. 3.36) and inserting the above expression for the complex reflection coefficient,

$$\begin{aligned}\Pi_{int}(\mathbf{p_0}) &= \left\{\int_{-\infty}^{\infty}\int_{-\infty}^{\infty} d\mathbf{r_1}d\mathbf{r_2}\langle\Psi(\mathbf{r_1})\Psi'^{*}(\mathbf{r_2})\rangle\sqrt{I(\mathbf{r_1})I(\mathbf{r_2})}G_0(\mathbf{r_1},\mathbf{p_0})G_0^{*}(\mathbf{r_2},\mathbf{p_0})\right\}\cdot \\ &\quad \left\{\int_{-\infty}^{\infty}\int_{-\infty}^{\infty} d\mathbf{r_3}d\mathbf{r_4}\langle\Psi^{*}(\mathbf{r_3})\Psi'(\mathbf{r_4})\rangle\sqrt{I(\mathbf{r_3})I(\mathbf{r_4})}G_1^{*}(\mathbf{r_3},\mathbf{p_0})G_1(\mathbf{r_4},\mathbf{p_0})\right\} \quad (3.49)\end{aligned}$$

By using the expansion $\exp[-i\Delta\varphi_{in}] \approx 1 - i\Delta\varphi_{in}$ and provided that the phase shift at $\mathbf{r_0}$ only occurs over a small area, A, compared to the two Green's functions, the following expression is obtained:

$$\begin{aligned}\Pi_{int}(\mathbf{p_0}) \approx \left(\frac{4\pi}{k^2}\right)^2 \Bigg[&\int_{-\infty}^{\infty} d\mathbf{r_1}\,|G_0(\mathbf{r_1},\mathbf{p_0})|^2 \int_{-\infty}^{\infty} d\mathbf{r_3}\,|G_1(\mathbf{r_3},\mathbf{p_0})|^2 - A\Delta\varphi_{in}\,|G_0(\mathbf{r_0},\mathbf{p_0})|^2 \\ &\int_{-\infty}^{\infty} d\mathbf{r_3}\,|G_1(\mathbf{r_3},\mathbf{p_0})|^2 + A\Delta\varphi_{in}\,|G_1(\mathbf{r_0},\mathbf{p_0})|^2 \int_{-\infty}^{\infty} d\mathbf{r_1}\,|G_0(\mathbf{r_1},\mathbf{p_0})|^2\Bigg] \quad (3.50)\end{aligned}$$

Besides the previous assumptions, we have here assumed that the illuminating spot does not truncate the extension of the Green's functions, i.e. we have assumed an infinitely large incident beam. The purpose here is not to deduce the influence of the illumination but to probe the influence of a Fourier plane filter.

We can now find the phase, $\Delta\varphi_{out}$, in the detector plane by using the following relation:

$$\Delta\varphi_{out} = \arctan\left[\frac{\mathrm{Im}\{\Pi(\mathbf{p_0})\}}{\mathrm{Re}\{\Pi(\mathbf{p_0})\}}\right] \approx \frac{\mathrm{Im}\{\Pi(\mathbf{p_0})\}}{\mathrm{Re}\{\Pi(\mathbf{p_0})\}} \quad (3.51)$$

where it tacitly has been assumed that $\Delta\varphi_{out}$ is small, since both A and $\Delta\varphi_{in}$ are small. Thereby the following expression for the IRF is obtained:

$$\Omega(\mathbf{r_0},\mathbf{p_0}) = \frac{\Delta\varphi_{out}(\mathbf{p_0})}{A\Delta\varphi_{in}(\mathbf{r_0})} = \frac{|G_1(\mathbf{r_0},\mathbf{p_0})|^2}{\int_{-\infty}^{\infty} d\mathbf{r_3}\,|G_1(\mathbf{r_3},\mathbf{p_0})|^2} - \frac{|G_0(\mathbf{r_0},\mathbf{p_0})|^2}{\int_{-\infty}^{\infty} d\mathbf{r_1}\,|G_0(\mathbf{r_1},\mathbf{p_0})|^2} \quad (3.52)$$

It is seen that the IRF as expected is independent of the ratio between the two Green's functions. The spatial position of the interference fringes indeed does depend on the perturbing effect of the holographic optical element in the Fourier plane, whereas the modulation depth depends on the diffraction efficiency of the filter.

Had the intensity distribution been included, the IRF would have taken the following form:

$$\Omega(\mathbf{r_0},\mathbf{p_0}) = \frac{|G_1(\mathbf{r_0},\mathbf{p_0})|^2\, I(\mathbf{r_0})}{\int_{-\infty}^{\infty} d\mathbf{r_3}\,|G_1(\mathbf{r_3},\mathbf{p_0})|^2\, I(\mathbf{r_3})} - \frac{|G_0(\mathbf{r_0},\mathbf{p_0})|^2\, I(\mathbf{r_0})}{\int_{-\infty}^{\infty} d\mathbf{r_1}\,|G_0(\mathbf{r_1},\mathbf{p_0})|^2\, I(\mathbf{r_1})} \quad (3.53)$$

This expression shows that the strength of the IRF in this case should be weighed with the incident intensity at that point. This means that the IRF may be changed by the intensity distribution – especially in the case where the illuminating beam truncates one or both of the extents of the Green's functions.

In the case where the Green's function multiplied by the incident intensity can be expressed as a function of $\mathbf{r_0} + \mathbf{p_0}$, the system is space invariant and the IRF is independent on the position in the detector plane. This is the case for an imaging system and an infinitely large illuminating beam.

Any possible defocus of the imaging system or curvature of the incident beam may be included in the Green's functions (see for example Eq. 3.34).

As already mentioned, the IRF gives the relative on-axis phase change due to a small piston-like deflection in the z-direction at position $\mathbf{r_0}$. Figure 3.33 shows the on-axis response for three different types of interferometers.

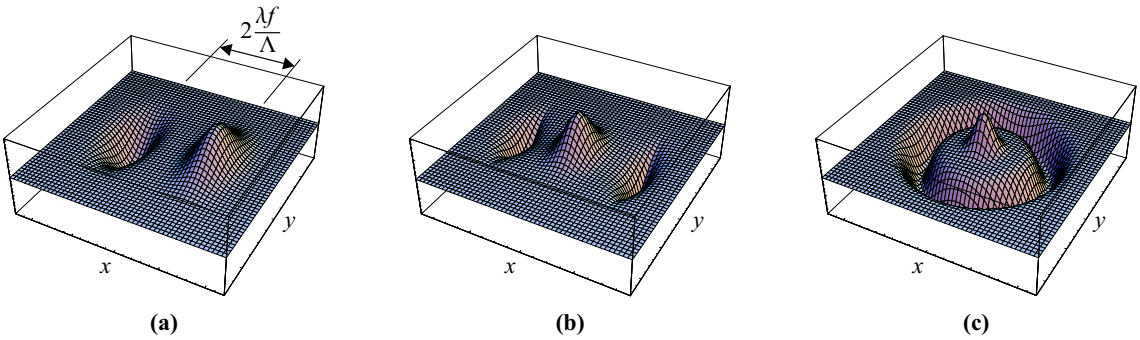

Figure 3.33: Impulse response for (a) a shearing system, (b) a one-dimensional and (c) two-dimensional curvature interferometer.

Figure 3.33 (a) shows the IRF for a simple shearing system where a grating with period Λ along the x-axis and suppressed zero-order diffraction is placed in the Fourier plane. A positive and negative contribution of widths ω is noticed giving rise to an impulse response function approaching the first derivative in the x-direction. Likewise, for the curvature interferometer, the IRF can be determined both for the one-dimensional case probing change in curvature in the x-direction, Figure 3.33 (b), and for the 2-D case probing change in average curvature, Figure 3.33 (c).

The IRF may be used not only to depict the effect of a given Fourier filter but also for synthesising a Fourier plane filter based on a desired impulse response by Fourier transforming the IRF.

3.4.5 Summary and Discussion

A common-path interferometry system for measuring various types of surface deflections has been presented. The system can be designed to probe the desired type of deflection by a proper choice of holographic optical element positioned in the Fourier plane of the system. This has been demonstrated with a specially designed Fourier filter for detecting change in surface curvature. A tool for depicting the effect of an arbitrary filter, called the impulse response function, has been presented and it has been shown how this tool can be used to design common-path interferometers for specific measurements. Fourier transforming the IRF will provide the phase function for the Fourier plane filter, which subsequently can be implemented as an on-axis filter or preferably designed

as an off-axis hologram with a carrier frequency bending the optical axis 90 degrees, thereby increasing the diffraction efficiency. Furthermore, oblique incidence of the incoming beam and a simultaneous use of an HOE will facilitate measurement of higher order strain components.

3.5 Outlook

It is clear that the results described earlier in this chapter are promising, but it is also clear that a lot of work has to be done before a commercial sensor can be developed. This section tries to speculate on methods to take this step and subjects for further studies.

First of all, we want to exploit the self-aligning features of the HOEs as well as the automatically provided quadrature phase signals. Furthermore, the sensor has to be implemented in a way so that it easily can be assembled, thereby lowering the production cost. We therefore suggest the use of a stacking technique, which is an easy way to achieve a compact and sturdy sensor and at the same time making it feasible to reduce production costs.

One of the problems addressed is how to separate the detector unit from the laser diode so that light is not coupled back into the laser diode, which could make the sensor unstable. The idea is to have the beam splitting and focusing as well as the receiving lenses in the same HOE plane, as the system described in Sec. 3.3. However, in order to separate the received signal from the transmitted signal, it could be desirable to let the transmitter HOE and receiver HOE be separate holograms. The receiver hologram has to be written in an almost identical way as the transmitter HOE, with the exception that the film has to be turned 180 degrees compared to the transmitter, so that the reflected light is diffracted and collimated at an angle laterally reversed compared to the normal of the HOE plane as illustrated in Fig. 3.34.

The complete setup consists of two stacked HOE layers and an electronics layer. The first HOE layer is partly composed of a HOE that collimates and directs the light to the transmitter HOE, which splits up and focuses the light onto three points on the diaphragm. The diaphragm consists of stainless steel and the reflecting side is polished to such a flatness that only specular reflections are observed. The receiver HOE collects the light reflected from the diaphragm and directs it towards another HOE, which is simply implemented as a linear grating. The first order diffraction from this grating is sent to a detector system. The detector system could simply be a photodiode array as used in Sec. 3.3, but could also consist of a series of apertures and micro-lenses that separates the six interference signals and focus them onto point detectors as illustrated in Fig. 3.34. In order to get an easy method for assembly and alignment of the sensor, the HOE layers can be constructed with alignment notches so that they can only be oriented in one way. Additionally, the inclusion of spacers between the HOE layers can be used for rough alignment of the sensor.

Although originally intended for pressure sensing, the measurement principle is probably better suited for vibrometry. This is due to the spatially provided quadrature phase signals, which makes the system suitable for dynamic measurements. Moreover, the vibrometer setup is simpler to implement, since only two lens elements are necessary in the transmitter HOE. Furthermore, the detector unit can be made much simpler, since the three interference signals can be focused onto three point detectors using a hologram identical to the one that collimates the laser diode (see

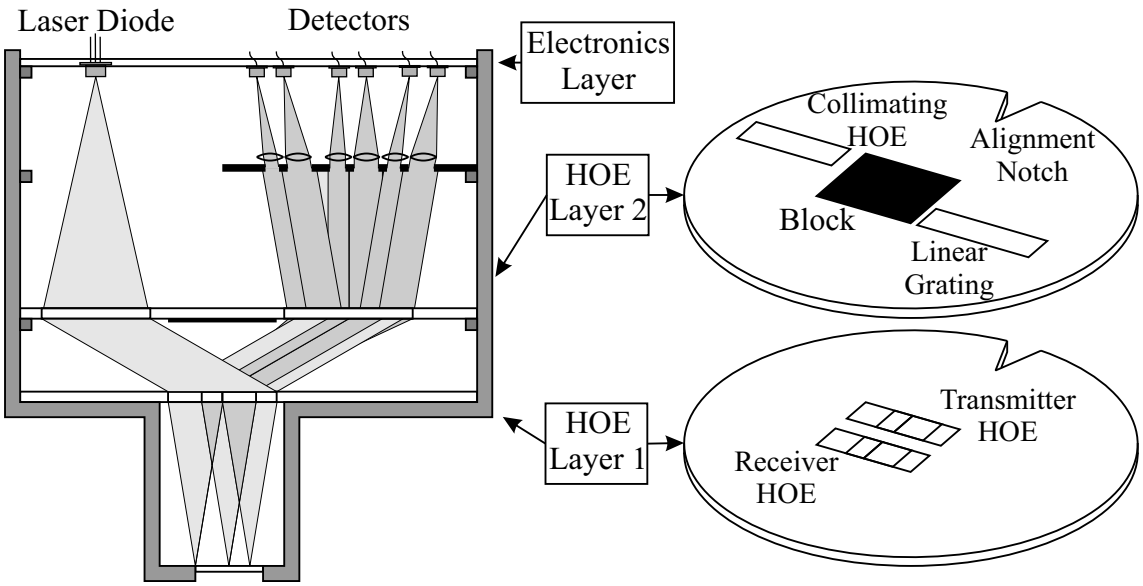

Figure 3.34: A proposal for the future design of an optical based pressure sensor, where the majority of the optical functions of the system are implemented in two stacked hologram layers.

Fig. 3.35).

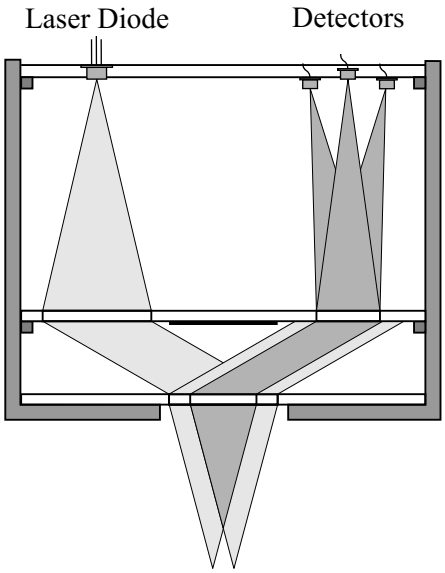

Figure 3.35: A proposal for the future design of an optical based vibrometer, where the the optical functions of the system are implemented in two stacked hologram layers.

The use of the identical hologram for the detector unit is not possible for the pressure sensor, since the two adjacent interference signals would be focused onto the same detectors.

3.6 Conclusion

A new interferometric system that can probe differential displacements has been devised. Additionally, a novel technique for extending the measurement range of this system has been presented. The technique has been demonstrated by constructing a system for measuring the angular deflection of a mirror. The system is constructed as a common-path interferometer that simultaneously probes the out-of-plane displacement of three points on an object surface. A theoretical description of the measurement range extension technique shows how the sensitivity and measurement range easily can be designed by choosing the proper distances between the probing points. Furthermore, the description shows how the technique can be reconfigured for the measurement of other types of differential displacements, such as the deflection of a diaphragm in a pressure sensor - the purpose that it originally was intended for.

The central part of the system is a multi-functional holographic optical element (HOE) that includes all the optical functions of the system and operates as both transmitter and receiver in the system. The HOE, additionally, provides spatially phase stepped interference signals, which mutually are shifted by $\pi/2$. This makes real-time phase measurements possible and makes the system well suited for measurement of dynamic displacements, e.g. vibrometry. The origin of the observed phase quadrature signals is not fully understood. However, the presence of a non-linear difference grating gives a plausible explanation of the effect. This hypothesis is still to be proven, and is a subject for further studies, perhaps through simulations that predict the shape and functionality of the surface structure based on the writing and development procedure of the HOE.

The optical alignment is imbedded in the HOE, which reduces the need for alignment during assembly and use of the system. This combined with the common-path scheme provides a system that is insensitive to common vibrations and when applied as a tilt sensor is insensitive to in-plane displacements. Furthermore, the system can be produced at a low cost through replication of the HOE, which is implemented as a surface relief grating. The system is thus well suited for applications in industrial environments and especially shows potential for use in commercial vibrometer sensors. It is demonstrated that the common-path interferometer can probe differential displacements with a sensitivity of approximately 0.3 nm. The system can in its present configuration with interfocal distances $d_1 = 1.20$ mm and $d_2 = 1.31$ mm, respectively, measure angular displacements on specular surfaces with a sensitivity of approximately 2.5×10^{-7} rad and facilitates absolute measurement over a range larger than 3.5×10^{-3} rad, i.e. the system has a dynamic range of 1:14,000. However, the system still needs a great deal of optimisation, especially if used on rough surfaces, where revised algorithms for the phase calculation have to be developed.

A suggestion for a future design of a pressure sensor and vibrometer has been given. This suggestion is based on stacking of layers with multifunctional HOEs. The stacking should allow for an cheap production of the layers through replication of the surface structures and additionally allow for easy alignment of the system. However, it would have been advantageous to demonstrate the use of the measurement principle in a vibrometry setup and in probing the deflection of the diaphragm. However, this has not been made in time for this thesis, and the applicability of the system for these purposes are still to be demonstrated. Furthermore, it would have been profitable to make replications of the HOEs and demonstrate the use of these replicas in a differential displacement sensor.

4

Flow Sensors

Computers are useless. They can only give you answers.

Pablo Picasso (1885-1973)

Since the invention of the laser, several optical methods for measuring velocity have been devised. Most of these methods are based on the Doppler effect, originally proposed by H. Z. Cummins et al. [63] and later used for dedicated flow measurements by J.W. Foreman et al. [64]. Laser Doppler Anemometry (LDA) systems are widespread [65–68] and commercial systems have been available for nearly four decades. Another common laser based method, which has been developed during this period, is the laser time-of-flight velocimeter (LTV), also known as laser dual focus anemometry (L2F) [69–71].

These laser based anemometry or velocimetry systems makes it possible to obtain excellent measurement accuracies and acquision rates for velocity measurements in, for example, fluids or gasses as well as for solid surfaces. The systems, however, are usually based on advanced and delicate optical technologies and voluminous laser systems, which makes miniaturisation of the systems difficult and generally makes the systems expensive to manufacture.

In the following a short description will be given of the three optical flow sensor techniques, which are pursued in this project, comparing advantages and disadvantages of the different techniques.

Laser Doppler Anemometry

Doppler shifts occur when there is movement of either the light source or the receiver. Other possibilities are when a medium is propagating or an intervening object reflects or scatters light. In LDA the Doppler shift occurs when a moving particle or object scatters or reflects light from the source to the receiver. This is the same principle as used in Radar, where the frequency of the source, however, is substantially lower than the frequency of light. In practice the Doppler shift is not accurately measurable in LDA systems, since the Doppler shift is very small compared to

the frequency of the light source. Therefore the *heterodyning principle* or *optical beating* of 2 frequencies is used in the LDA [68].

Typical LDA sensors have a measurement volume of 0.1 mm in diameter and 1 mm in longitudinal length with a fringe spacing of 2-4 μm. A basic LDA system can measure one velocity component independent of the degree of turbulence. Depending on the geometry of the system, the signal processing and setup, one can expect measurement accuracies of 0.1-1%. Velocity measurement can be obtained from signals where the signal-to-noise ratio is less than -5 dB [67, 68, 72].

The LDA systems usually rely on high power and wavelength stabilised lasers such as the Ar-Ion laser. The systems also use high quality optics that is carefully aligned so that the two laser beams intersect at their respective beam waists. This is essential in order to achieve a minimum spatial gradient in the measurement volume [73, 74]. Commercial systems are therefore rather bulky and expensive in manufacturing terms. Another thing that limits the possibilities of miniaturisation via the use of laser diodes, is the fact that the fringe spacing in the measurement volume is directly proportional to the wavelength. Due to the uncertainty of 1-3 longitudinal modes of the laser diode (see App. A), this usually renders the use of laser diodes impossible.

Laser Time-of-Flight

LTV systems rely on high quality of the foci of two parallel laser beams having a well-known spacing. These two focal spots will be imaged onto two detectors carefully avoiding any crosstalk. Particles passing through both beams in the measurement volume will scatter light that is sent to the two detectors. By, for instance, cross-correlating the temporal signals of the two detectors, one can find the time delay between the two signals, thereby being able to calculate the velocity of the particle, since the beam spacing is known. A laser time-of-flight system with an numerical aperture comparable to that of an LDA system will be able to give comparable measurement accuracies [71].

Generally, LTV systems will yield spot intensities that are one or two magnitudes larger than those from LDA systems, while the digital signal processing requires a signal-to-noise ratio of approximately 10 dB [75].

The basic time-of-flight design does not contain any wavelength-dependent optics and can thus more easily be implemented with laser diodes as the light source.

Multiple Time-of-Flight

More recently, several authors have suggested multiple time-of-flight sensors based on edge emitting laser diode arrays [75, 76]. The former of these systems is based on an array of four 30 mW laser diodes, which enables measurement accuracies comparable to commercial LDA systems. The total intensity in the measurement volume increases with the number of laser beams. This method has the advantage that several time-of-flight measurements are obtained when a particle passes through the measurement volume. Thereby, one can get a successful velocity measurement from signals with a lower signal-to-noise ratio. As something new, a multiple time-of-flight based on an array of evenly spaced vertical cavity surface emitting laser diodes (VCSELs) [77]. This

method has some advantages compared to the use of laser diodes, viz. the fact that VCSELs have circular symmetry, relative small beam divergence and no mode hopping between longitudinal modes.

The multiple time-of-flight sensor is probably one of the easiest ways to implement a compact and robust flow sensor. However, these systems are not very flexible. For instance, only VCSEL arrays with a spacing of 250 μm exist, which means that one cannot design a system with a desired ratio between beam diameter and beam spacing. Furthermore, these system are only advantageous in conditions where a relatively large measurement volume is allowed.

Reader's Guide

During the period of the PhD project, the PhD fellow has worked on three different flow measurement systems. A new beam splitter for LDA systems based on linear gratings has been developed. The new beam splitter enables the use of laser diodes in LDA systems by letting the fringe spacing in the measurement volume be independent of wavelength changes. The work on this system has been aimed at a proof-of-principle so that it would support the patenting of the system [78], and the work has thus not been aimed at the development of a commercial product. The work on the LDA sensor is described in Sec. 4.1 and has been submitted to Applied Optics [79].

The commercial aspects of the work has generally been focused on the development of a tool for calibrating the ultrasound sensors. This tool has been focused on the development of a time-of-flight sensor, which can be used to make a flow profile measurement of flow pipes up to DN200 (Ø200 mm). The LTV sensor is based on a single multifunctional holographic optical element that allows for a robust, self-aligning system that to a first degree is independent of wavelength changes. The work on the laser time-of-flight sensor is described in Sec. 4.2. Due to the commercial development of the system, a lot more work on the development of the digital signal processing has been performed on this system compared to the other systems described. The system has been patented (see Ref. [80]) and a scientific paper on the system is in preparation [81].

Finally, the PhD fellow has performed the characterisation of the measurement volume of a multiple time-of-flight sensor based on a VCSEL array [77]. These measurements will be compared to the other systems. This type of sensor is probably the easiest of the three sensors to make as a compact and robust sensor. However, the sensor is not suitable for measurements in large flow pipes, since a large working distance will yield a large spacing between the probe beams and therefore a very large measurement volume. The work has merely been included in the thesis as a comparison to the other systems and is described in Sec. 4.3

4.1 Laser Doppler Anemometry

We propose a new beam splitter system that makes it possible to use non-stabilised laser diodes for Laser Doppler Anemometry (LDA) systems by making the system wavelength independent. The beam splitter consists of two linear diffraction gratings that produce two parallel beams with a beam spacing, which is wavelength dependent. This ensures a passive wavelength compensation of the fringe spacing in the measurement volume. The distance between the two parallel beams can be chosen by changing the distance between the two gratings, while the distance to the mea-

surement volume can be designed by choosing a condensing lens with the proper focal length. This means that the system can be designed to have a desired fringe spacing in the measurement volume. The gratings are implemented as surface relief holograms in photoresist. This makes it possible to mass-produce the beam splitter system at a low cost through replication of the structure. The method for passive wavelength compensation of the fringe spacing is demonstrated both theoretically and experimentally. This work has been submitted to applied optics (see Ref. [79]).

4.1.1 Measurement Principle

The most common configuration of the LDA system is the *Differential Doppler Technique* or *Dual Beam Technique* (see for instance Ref. [68]). Figure 4.1 shows the schematics for a simple arrangement for this technique.

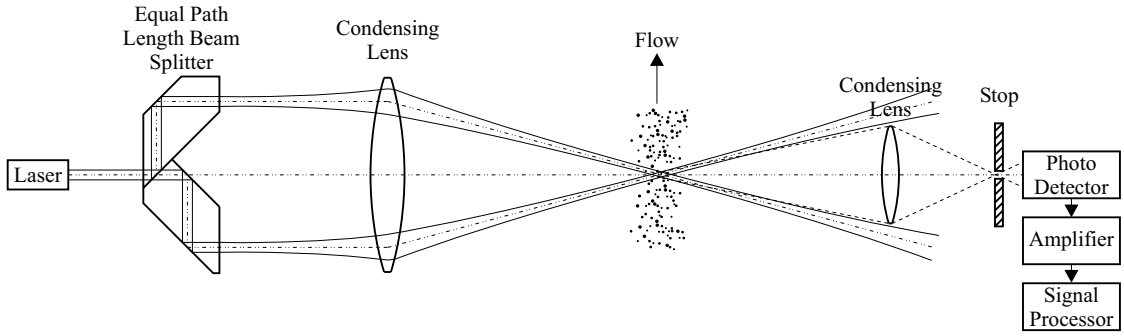

Figure 4.1: Typical setup for the LDA-system.

A laser beam is split up into two beams of equal intensity by a 50/50 equal path length beam splitter and later both beams are focused and crossed at the point under investigation by a condensing lens. Scattered light from particles passing through this region is imaged onto a photo detector. Since the light scattered from both beams reaches the detector simultaneously, a beat frequency, corresponding to the difference in Doppler shifts from the two scattered beams, is obtained. The beat frequency is directly proportional to the particle's velocity component perpendicular to the fringe geometry, which emerges in the cross section. When a particle passes through the cross section, the modulation of scattered light measured at a detector changes due to differing illumination of the particle. The output signal from the detector is processed to find the velocities of the particles. Additionally, the optical path lengths for the two beams are assumed to be the same. Thereby it is ensured that the beam waists are located at the same distance from the lens and the beams are coherent in the measurement volume.

If two-dimensional velocities are required to be measured, then there must be two extra beams present in the LDA system. These must be aligned in such a way that the fringe geometry emerging in the measurement volume is perpendicular to the other fringe geometry. If extending this to 3D-measurement of the velocity then an additional two beams must be used. In practice the laser beam pairs which are placed in planes perpendicular to each other, have different wavelengths. Thereby the measurement of the three velocity components can be distinguished from each other.

Miniaturising LDA systems

The LDA systems usually rely on high power and wavelength stabilised lasers such as the Ar-Ion laser. The systems also use high quality optics that are carefully aligned so that the two laser beams intersect at their respective beam waists. This is essential in order to achieve a minimum spatial gradient in the measurement volume [73, 74]. Commercial systems are therefore rather bulky and expensive in manufacturing terms.

There have been many attempts to miniaturise LDA systems with the intention to introduce the measurement technique for industrial purposes. However, to the best of our knowledge, there has not yet been introduced any low-cost commercial system. This is probably due to the lack of affordable medium power lasers and the price of the optical components needed to generate the diffraction-limited beams that are necessary to obtain sufficiently accurate fringe spacing.

Some of the proposed systems for miniaturisation are based on fibre lasers [82] while others are based on laser diodes [83–85]. The latter is an obvious way to miniaturise LDA systems. However, laser diodes are significantly temperature dependent and even temperature stabilised laser diodes will be undefined within 1-3 longitudinal modes due to mode hops (see App. A). Wavelength changes will normally give rise to changes in the fringe spacing in the measurement volume and thereby influence the measurement accuracy.

Some of the laser diode systems are based on conventional optics [85], while others try to compensate for the wavelength uncertainty by using diffractive optical elements [48, 82, 86, 87]. In order to obtain high diffraction efficiencies, these types of systems usually require the use of volume holograms, which are difficult to replicate. Dam-Hansen et al. have considered this dilemma by using surface relief holograms with high spatial frequencies implemented in photoresist for an optical flow sensor, which combines replicability through for instance injection moulding and high diffraction efficiency [48]. We propose a new diffractive beam splitter for use in LDA systems that utilises these ideas. Additionally, we try to devise a flexible system that does not have limitations on the working distance and closing angle such as the systems proposed in Refs. [86, 87]. The wavelength compensation is achieved by changing the distance between the two parallel beams as the wavelength changes. Thereby the closing angle of the two beams after the condensing lens will also be dependent on the wavelength. The two parallel beams are generated by a beam splitter consisting of two linear gratings positioned laterally compared to the propagation direction. This also ensures that higher diffraction efficiencies can be achieved, since the diffraction angles are large.

4.1.2 Optical System

The object of the system presented is to provide a flexible and simple beam splitter arrangement that ensures that the fringe spacing in the probe volume is kept constant despite wavelength fluctuations of the applied light source.

The fringe spacing, Λ, in the measurement volume of an LDA system assuming parallel wave-

fronts is given by:

$$\Lambda = \frac{\lambda}{2\sin(\theta/2)}\,, \tag{4.1}$$

where λ is the applied wavelength and θ is the angle between the probe beams. When a particle passes through the measurement volume and the interference pattern, the intensity of light sent to the detector will vary because of differing illumination of the particle. The frequency of the measured signal will be given by the particle velocity component, $v_\perp$, perpendicular to the fringe geometry and the distance, Λ, between the fringes,

$$f = \frac{v_\perp}{\Lambda} = \frac{2v_\perp \sin(\theta/2)}{\lambda}\,. \tag{4.2}$$

The measured frequency is equivalent to the difference in Doppler shift from the scattered light of the two probe beams.

It is readily seen from Eq. (4.1) that an increase in wavelength will increase the fringe spacing. If the system can be designed so that the angle, θ, between the probe beams follows the wavelength fluctuations, the change in fringe spacing can be compensated.

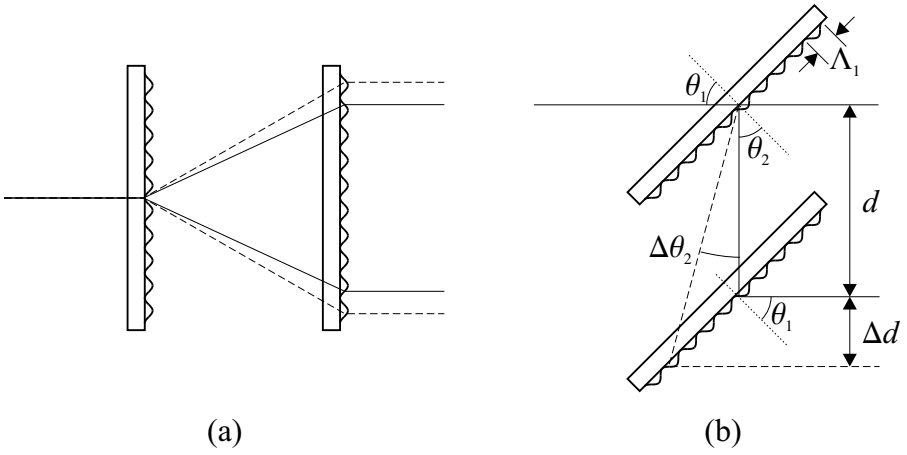

Figure 4.2: Two ways of producing two parallel beams using two diffraction gratings as a beam splitter. (a) is a common approach and (b) is the new proposed configuration. The dashed lines illustrate the beam splitting for a higher wavelength.

Our ambition is to construct a beam splitter that compensates for wavelength fluctuations in LDA systems by making the distance between the two parallel beams that are sent to the focusing lens wavelength dependent. This is achieved by letting two diffraction gratings handle the beam splitting. However, we do not want to put any restrictions on the working distance of the system. Therefore, we have displaced the gratings laterally as illustrated in Fig. 4.2 (b) rather than longitudinally as in Fig. 4.2 (a), which is a more common approach (see for instance Ref. [87]). The new method also makes it possible to make a more diffraction efficient system, since only the 0th and 1st order diffraction are present and where arbitrary efficiencies between these two diffraction orders can be obtained.

The diffractive beam splitter is schematically illustrated in Fig. 4.2 (b). A collimated laser beam, originating from a laser diode with a collimating lens is incident to a linear grating at an angle of θ_1 to the normal. The grating both diffracts and transmits the light. The diffracted light is diffracted at an angle θ_2 to the normal and is sent to another grating, which has the same grating period and positioned at the same angle as the first grating. Therefore, the light diffracted from the second grating will be parallel with the transmitted light from the first grating.

Knowing the diffraction dependency on the operation wavelength, λ, and the spatial frequency, Λ_1, of the diffraction grating, one can derive the following expression for the diffraction angle θ_2 (see also Fig. 4.2 (b)),

$$\theta_2 = \arcsin\left(\frac{\lambda}{\Lambda_1} - \sin\theta_1\right) \tag{4.3}$$

where θ_1 is the angle of incidence on the first grating. The shift in diffraction angle, $\Delta\theta_2$, due to small shifts in wavelength and/or grating period then takes the following form:

$$\Delta\theta_2 = \frac{1}{\sqrt{1-\left(\frac{\lambda}{\Lambda_1} - \sin\theta_1\right)^2}}\left(\frac{1}{\Lambda_1}\Delta\lambda - \frac{\lambda}{\Lambda_1^2}\Delta\Lambda_1\right) . \tag{4.4}$$

The change in diffraction angle will lead to a change, Δd, in the distance between the two parallel beams. Provided that the grating period is constant ($\Delta\Lambda_1 = 0$), then the change in beam separation, Δd, will be given by:

$$\Delta d = \frac{\sin\theta_2 \sin\Delta\theta_2}{\cos\theta_2\cos\Delta\theta_2 - \sin\theta_2\sin\Delta\theta_2} d , \tag{4.5}$$

where it has been assumed that the light is deflected at an angle of 90 degrees ($\theta_1 + \theta_2 = 90°$).

The transmitted light from the first grating is reflected by two mirrors in order to ensure an equal path length in the two arms (see Fig. 4.3). The two parallel beams from the beam splitter system have a beam spacing $d_{res} = 2d$ and are sent to a condensing lens, which focuses and crosses the two laser beams at their waist points. These two beams will be denoted *probe beams*. The result is that a fringe pattern arises in the section where the two beams are overlapping. It is important to have the mirrors in the beam splitter system, since it is necessary for the two beams to have equal path lengths in order to obtain a good fringe geometry [73, 74].

We choose to implement the beam splitter system so that the angle of incidence and diffraction, θ_1 and θ_2, are both 45 degrees. Equation (4.5) can then be simplified to:

$$\Delta d = \frac{\sin\Delta\theta_2}{\cos\Delta\theta_2 - \sin\Delta\theta_2} d \approx \Delta\theta_2\, d . \tag{4.6}$$

where the last derivation can be made since $\Delta\theta_2$ is small.

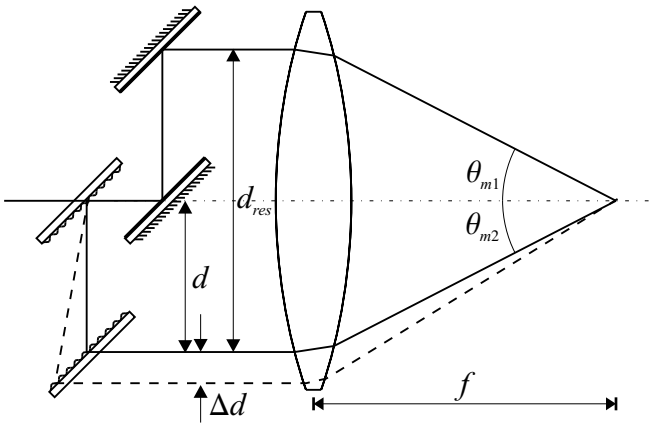

Figure 4.3: The LDA system based on beam splitter consisting of diffractive optical elements.

The angles, θ_{m1} and θ_{m2}, of the two probe beams are given by:

$$\theta_{m1} = \arctan\left(\frac{d_{res}/2}{f}\right) \tag{4.7}$$

$$\theta_{m2} = \arctan\left(\frac{d_{res}/2 + \Delta d}{f}\right), \tag{4.8}$$

where f is the focal length of the condensing lens (see Fig. 4.3). The fringe spacing for two plane waves intersecting at an angle of $\theta_{m1} + \theta_{m2}$ is given by the following expression,

$$\Lambda_m = \frac{\lambda + \Delta\lambda}{2\sin\left(\frac{\theta_{m1}+\theta_{m2}}{2}\right)}. \tag{4.9}$$

The compensation of the fringe spacing occurs since the diffraction angle of the gratings is approximately proportional to the wavelength (see Eq. (4.4)). That is, the diffraction angle will increase if the wavelength increases. The distance between the two parallel beams will thereby increase with the distance Δd (see Eq. (4.6)) and consequently also the angle, $\theta_{m1} + \theta_{m2}$, between the probe beams (see Eq. (4.7) and (4.8)). The denominator of Eq. (4.9) will thus increase and compensate for the increase in wavelength in the numerator.

Using Eq. (4.3)-(4.9) with $\Delta\Lambda_1 = 0$, the change in fringe spacing of the proposed system as a function of wavelength will vary as shown in Fig. 4.4. This is compared to an uncompensated system, where the fringe spacing will be proportional to the wavelength according to Eq. (4.1).

In this comparison there has been assumed a centre wavelength of $\lambda = 672$ nm, the beam distance $d_{res} = 38$ mm and the focal length of the lens being $f = 400$ mm, which yields a fringe spacing of approximately 7.08 μm.

It is seen from the magnified plot in Fig. 4.4 (b) that the new system does not perfectly compensate for the wavelength changes as is the case for the systems presented in Refs. [86, 87]. This is due to the slight asymmetry about the centre axis of the new beam splitter system. However,

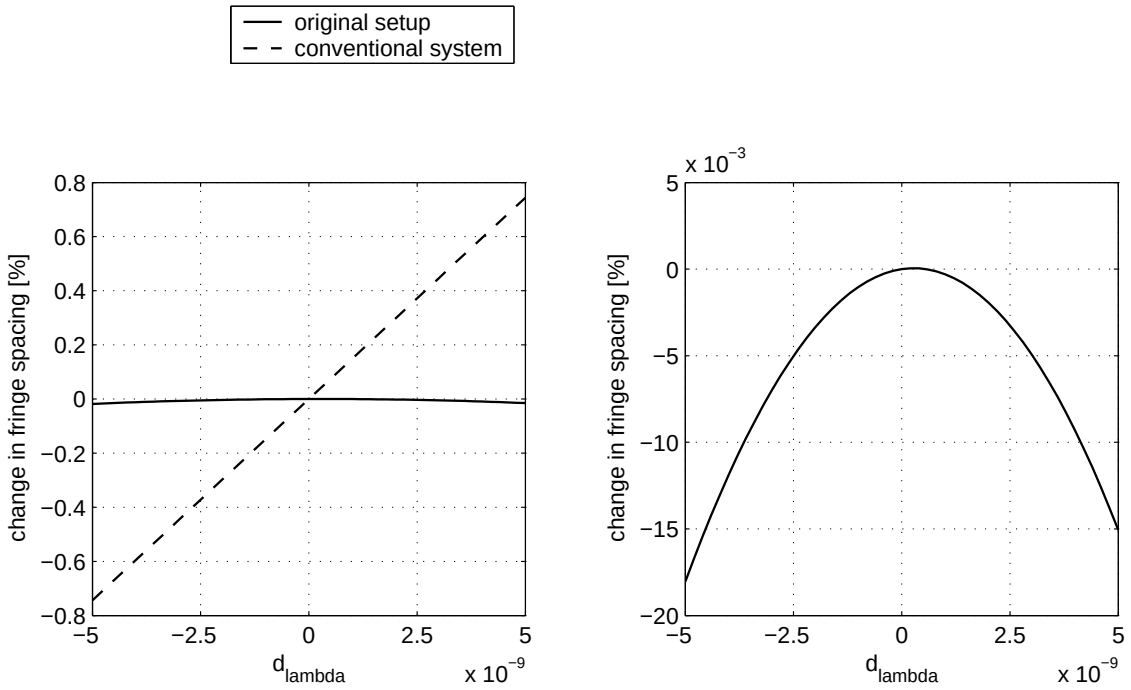

Figure 4.4: The change in fringe spacing as a function of the wavelength compared with an uncompensated LDA system.

it is a huge improvement compared to an uncompensated system and it leaves one with a system that can easily be designed to achieve a desired fringe geometry of the system, since the fringe period can be changed by altering the lateral displacement of the two gratings and mirrors and/or choosing another focusing lens. The change in fringe spacing for a ± 5 nm wavelength change is smaller by more than a factor of 42 compared with an uncompensated system. For a ± 0.3 nm change in wavelength, corresponding to a mode hop in a laser diode, the change in fringe spacing is reduced more than 200 times.

Temperature Dependence of the Gratings

Variations in the temperature will not only influence the light source. It will also influence the diffraction angles of the light due to expansion or contraction of the gratings. The change, $\Delta\Lambda_1$, in grating period is given by:

$$\Delta\Lambda_1 = \alpha\, \Delta T\, \Lambda_1\,, \tag{4.10}$$

where α is the linear thermal expansion coefficient for the material used and ΔT is the change in temperature. The diffraction angle, θ_2, is therefore seen to be directly proportional to the temperature fluctuation according to Eq. (4.4), assuming that the temperature does not change the wavelength of the light source ($\Delta\lambda = 0$). The change in fringe spacing due to the temperature fluctuations is depicted in Fig. 4.5 for different materials of the gratings.

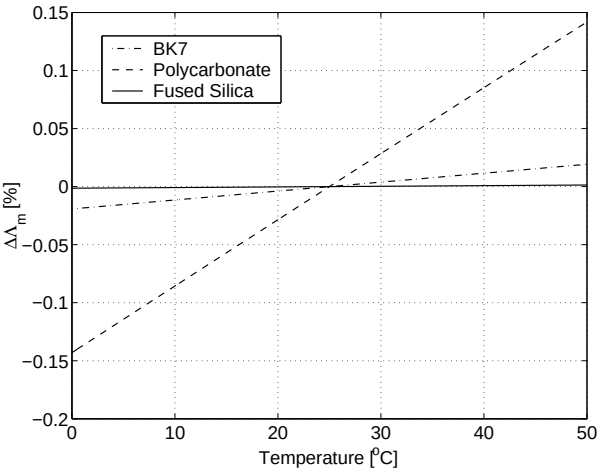

Figure 4.5: The change in fringe spacing due to temperature fluctuations of the gratings. The operation wavelength is assumed to be constant.

Polycarbonate would be a material choice, if one wants to replicate the diffractive structures, for example through injection moulding. However, it is seen from Fig. 4.5 that the temperature dependence is quite severe when using polycarbonate. The gratings should therefore either be constructed in materials with a lower expansion coefficient, like BK7 or fused silica, or be temperature stabilised. Alternatively, the system should be combined with a temperature sensor, so that the corresponding change in fringe period is known.

Turning of Fringes

Since the system is not symmetrical about the optical axis, the fringes will shift orientation as the probing angles change due to wavelength fluctuations. This will result in a measurement error, the magnitude of which will be estimated here. The change in angle, $\Delta\phi$, for the fringes will be given by:

$$\Delta\phi = \Delta\theta_{m2}/2, \tag{4.11}$$

where the change in probing angle, $\Delta\theta_{m2}$, can be found from Eq. (4.8). The velocity measurement error, $\Delta v/v$, will therefore take the following form:

$$\frac{\Delta v}{v} = 1 - \frac{1}{\cos\Delta\phi}\,. \tag{4.12}$$

where v is the correct velocity of the flow.

The measurement error due to fringe turning simulated with the same parameters as previously described is depicted in Fig. 4.6.

It is seen that the error due to fringe turning is much smaller than the change in fringe spacing depicted in Fig. 4.4 and the effect is therefore negligible.

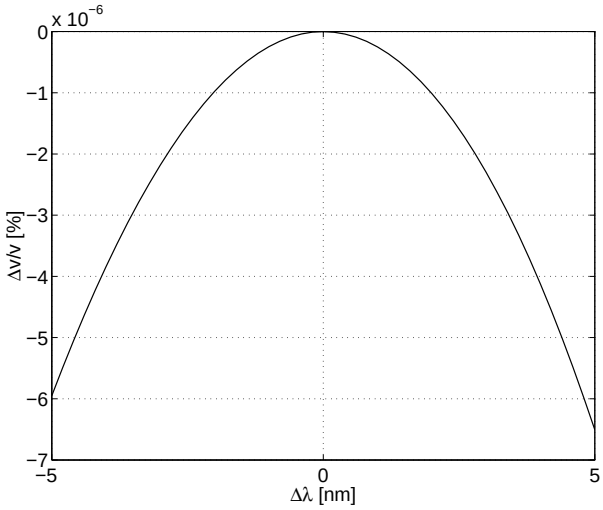

Figure 4.6: Measurement error due to turning of the fringes as the wavelength is varied.

Optimising the length of the Diffraction Arm

Previously in this section, it was assumed that the distances between the two gratings and the two mirrors were identical. However, this does not necessarily yield the optimum compensation for wavelength changes. In general there will be a optimum lateral distance between the two gratings. This distance will depend on the chosen geometry of the system, that is, be dependent on the chosen distance, d_{res}, between the two parallel beams from the beam splitter system and the focal length, f, of the lens (see Fig. 4.3). The optical path length difference between the diffracted and undiffracted arm can then be equalised by tilting the two mirrors as illustrated in Fig 4.7.

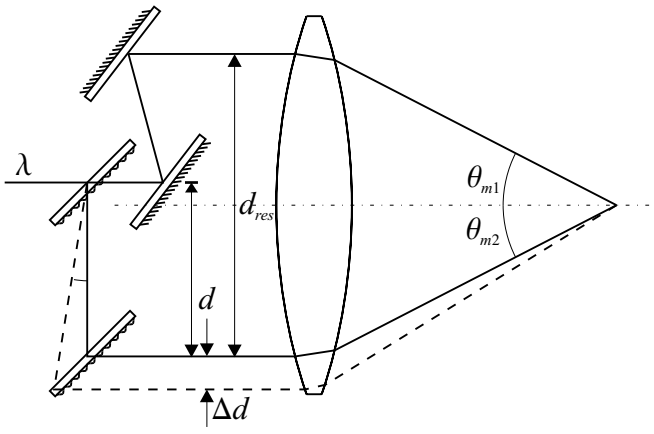

Figure 4.7: General setup of the LDA system, where the gratings assure optimum compensation for wavelength changes and the mirrors ensure equal path lengths in the two arms.

If the LDA system has a low numerical aperture, then the arguments of Eq. (4.7) and (4.8) will be

small. In this case, Eq. (4.9) can be approximated with the following expression:

$$\Lambda_m \approx \frac{\lambda + \Delta\lambda}{d_{res} + \Delta d} \approx \frac{\lambda + \Delta\lambda}{d_{res} + \frac{1}{\sqrt{1-\left(\frac{\lambda}{\Lambda_1} - \sin\theta_1\right)^2}} d \, \frac{\Delta\lambda}{\Lambda_1}} \,, \tag{4.13}$$

where the last derivation has been made using Eq. (4.4) and (4.6).

The system is least sensitive to wavelength changes when the slope of Eq. (4.13) as a function of $\Delta\lambda$ is zero. We therefore differentiate Eq. (4.13) with respect to the change in wavelength $\Delta\lambda$ and solve the resulting expression equal to zero. This yields the following relation for the ratio d/d_{res}:

$$\frac{d}{d_{res}} = \frac{\cos\theta_2}{\sin\theta_1 + \sin\theta_2} \,. \tag{4.14}$$

For a system with a low numerical aperture where $\theta_1 = \theta_2 = 45°$, the optimum ratio between d and d_{res} is therefore 50%.

If the numerical aperture is not small, then the analysis above does not hold and finding the optimum ratio between d and d_{res} becomes quite complicated to solve analytically. However, it can easily be solved empirically by trial and error. This approach yields a relation between the optimum ratio d/d_{res} and the numerical aperture (or equivalently $d_{res}/2f$) as depicted in Fig. 4.8

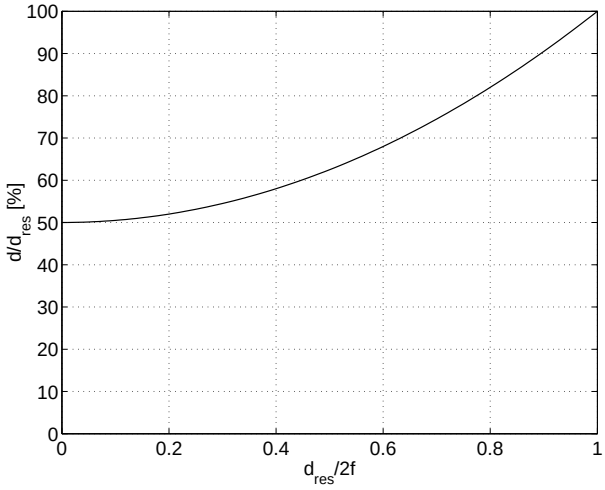

Figure 4.8: The optimum ratio between the distance between the two gratings, d, and the distance between the two parallel beams, d_{res}, for the beam splitter as a function of the numerical aperture of the system.

If again assuming a centre wavelength of 672 nm, a distance between the two parallel beams of 38 mm and the use of a condensing lens with a focal length of 400 mm, then one obtains from Fig. 4.8 that the optimum distance, d, between the two gratings is 19.04 mm. That is, very close to the previously proposed design where $d = d_{res}/2$. If one observes the relation between the optimum grating spacing and the focal length of the lens as illustrated in Fig. 4.8, it is seen that the lower the numerical aperture, the closer the optimum ratio d/d_{res} gets to 50%.

In this configuration it means that the system can readily be designed with the two mirrors angled 45 degrees to the incoming beam. This makes alignment of the system easy and additionally it means that the beam splitter system can be constructed on two substrates, both substrates containing one grating and one mirror as illustrated in Fig. 4.9. It is also seen from Fig. 4.8 that as long as the system does not have a very high numerical aperture, then the ratio between d and d_{res} is close to 50% and one can readily use the implementation shown in Fig. 4.9.

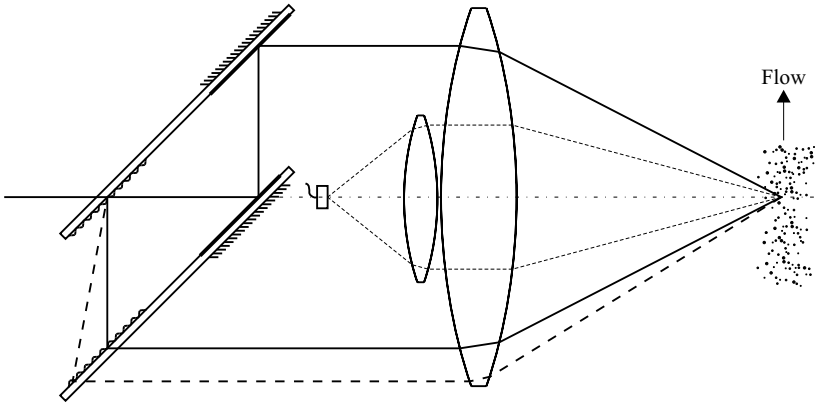

Figure 4.9: A possible way to implement the beam splitter in a LDA system with a detection system consisting of a lens and a photodiode. Constructing substrates with one grating and one mirror simplifies the alignment of the system.

However, if one desires to design a system with a high numerical aperture, then one can still achieve the optimum compensation by designing the ratio d/d_{res} according to Fig. 4.8 and tilting the mirror in order to obtain an equal optical path length in the two arms.

4.1.3 Measurements

The objective of the measurements is to demonstrate that the proposed diffractive beam splitter configuration compensates for wavelength fluctuations. In other words, our aim is to make a proof-of-principle. For simplicity, we therefore choose to construct the system without a normal LDA detection system and instead make a direct intensity scan of the measurement volume.

The measurements for verifying the wavelength compensating LDA system were performed with a tunable external cavity laser diode having a centre wavelength of 672 nm. The laser beam is made circular by an anamorphic prism pair. The collimated laser light was sent through a 1:1 beam expander and then through the novel beam splitter consisting of two linear gratings with a grating period of 475 nm and two mirrors. The lenses of the beam expander are movable so that the beam can be adjusted so that the two probe beams cross at their respective beam waists.

The gratings are implemented as transmission surface relief gratings in photoresist on a glass substrate. They are produced using an analog interferometric setup, employing a HeCd laser at 441.6 nm as described in Chap. 2. The depth of the grating structure sets the diffraction efficiency of the grating and the applied grating period ensures that only two diffraction orders are present,

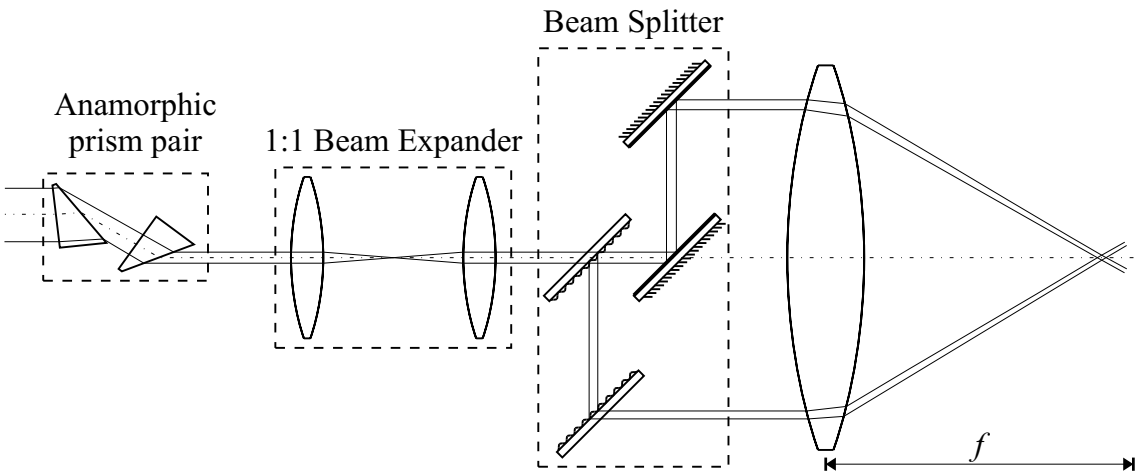

Figure 4.10: Figure that shows how the measurement setup is constructed with the 1:1 beam expander in order to be able to adjust the position of the beam waist.

namely the 0th order (undiffracted) and the 1st order (diffracted). The ratio between the energy in the 0th and 1st order diffraction order is 44/56 for the first grating and 10/90 for the second grating. These values ensures approximately equal intensities in the two parallel beams and thereby a fringe visibility of nearly 100% in the measurement volume. The total efficiency of the diffractive beam splitter without anti-reflection coating of the glass substrates is better than 80%. Using anti-reflection coated components will make it possible to obtain an efficiency close to 100%.

The distance between the two parallel beams was set to 38 mm and the focusing lens had a focal length of 400 mm. Thereby a fringe period of approximately 7.08 μm according to Eq. (4.9) was obtained. The wavelength of the tunable laser diode was changed in steps of 1 nm from 665 to 679 nm. For each wavelength, 10 scans of the measurement volume were made, such as the one depicted in Fig. 4.11. The scans were made with a Photon Inc. beam scanner with a 0.2 μm resolution positioned in the cross section of the two laser beams. Prior to the measurements, the beam scanner was translated through the measurement volume to ensure that the two probe beams crossed at their respective waist points and to make sure that the beam scans were performed in the correct position. The scans were Fourier transformed to find the fringe spacing using a Gaussian fitting function in the frequency space. The results of the measurements are shown in Fig. 4.12.

The error bars show the mean measured fringe spacing together with the standard deviation of the measurements. The standard deviation is approximately 0.15 percent of the mean fringe spacing. The dash-dotted line shows the theoretical fringe spacing for an uncompensated system, while the dashed line shows the theoretical fringe spacing for the new system. The measurement uncertainties are seen to be so large that the effect of the new beam splitter system cannot conclusively be verified. For comparison, the theoretical change in the fringe period due to a 5 nm change in wavelength is approximately 0.015 percent (see also Fig. 4.4). That is, the measurement uncertainty is approximately 10 times greater than the quantities that we are trying to demonstrate. However, the dashed line is within all the error bars, and the measurements clearly show that the diffractive

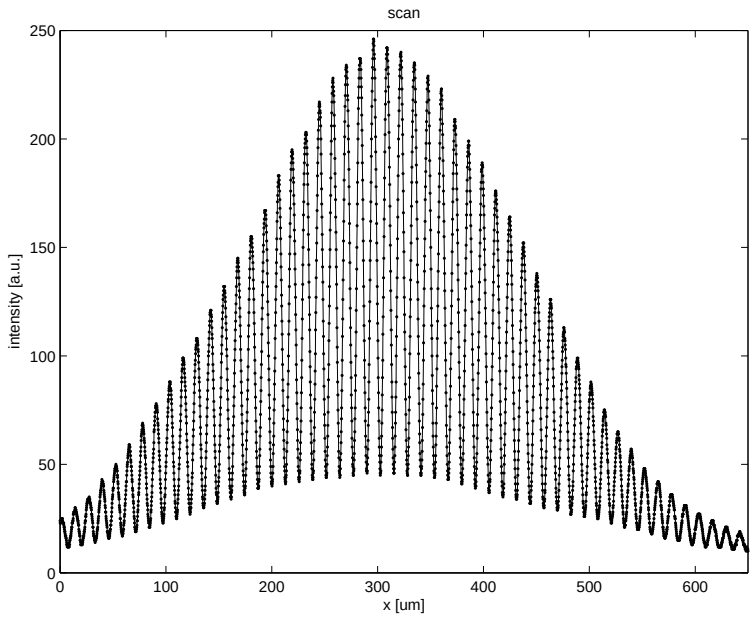

Figure 4.11: Beamscan of the measurement volume for a system with $f = 400$ mm and $d_{res} = 20$ mm.

beam splitter compensates for wavelength fluctuations.

4.1.4 Discussion and Conclusions

A novel beam splitter system that can be used for passive wavelength compensation of the fringe period in laser Doppler anemometry (LDA) systems has been presented. A theoretical examination of the beam splitter shows that significant improvement of the wavelength sensitivity of the

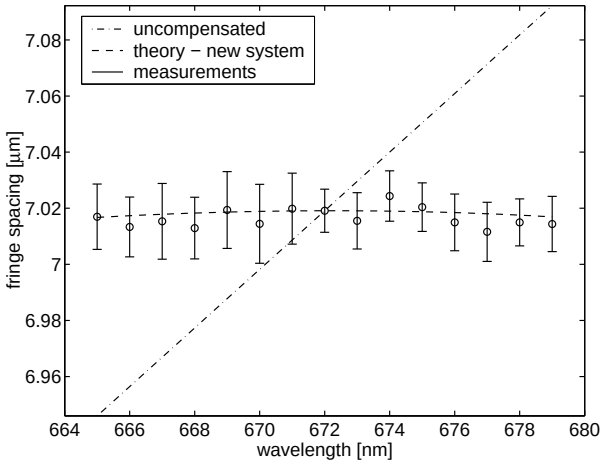

Figure 4.12: The measured fringe period in the cross section of the measurement volume. The wavelength was varied using a tunable laser diode. The error bars show the standard deviation of the measurements for the different wavelengths.

LDA system can be achieved by using the beam splitter in the system compared to a conventional LDA setup. This is substantiated by the measurements, which were carried out by making beam scans in the cross section of the measurement volume. The measurements were performed using a tunable laser diode so that it indeed was the wavelength dependency that was tested rather than the temperature dependency. The theory and measurements indicates that non-stabilised laser diodes can be used together with the new beam splitter in LDA systems.

However, if the wavelength fluctuations in the system were to occur due to changes in the temperature, then one should be aware that this can influence other properties of the system and thereby also the fringe period in the measurement volume. The temperature fluctuations could for instance influence the collimation of the laser diode, which would result in spatial gradiants in the measurement volume, since the two probe beams would no longer intersect at their beam waists. More obviously, the temperature fluctuations could make the grating material expand or contract, thereby changing the grating period and consequently also the diffraction angles. The theoretical treatment of this subject shows that the change in fringe period in the measurement volume due to changes in the temperature can be quite severe when the gratings are fabricated for instance in polycarbonate. Using this type of material in a replication process, therefore means that the system either should be temperature stabilised or the temperature should be probed in order to calculate the corresponding shift in fringe period. Alternatively, the gratings have to be constructed in a material with a lower thermal expansion coefficient.

One of the main advantages of the new beam splitter setup is that it is very simple and easy to align. One can design the system to have a desired fringe geometry by choosing the proper distance between the parallel beams from the beam splitter and a lens with the proper focal length. The angle of the mirrors in the beam splitter configuration can be changed so that equal path lengths in the two arms as well as the optimum wavelength compensation can be achieved. This means that one does not have to construct new gratings, if changing to a lens with a different focal length. This would be necessary for instance in the system presented in Ref. [86, 87], since the diffraction angles of the grating have to be matched with the closing angles of the probe beams. Additionally, the large diffraction angles in the beam splitter we present, make it possible to implement the gratings as surface relief holograms with high diffraction efficiencies instead of using volume holograms. This means that the beam splitter can be mass-produced at low cost through replication of the structure, for instance by injection moulding. One of the disadvantages of the system compared to Ref. [87] is that our system does not perfectly compensate for wavelength fluctuation. This would be the case for Ref. [87] as long as the diffraction angle from the gratings and the closing angle of probe beams are matched, in which case the fringe period in the measurement volume would be one half of the grating period. However, the compensation with the system we propose is still significant, and it leaves one with a system that is more flexible.

4.2 Laser Time-of-Flight

The laser time-of-flight velocimeter (commonly abbreviated to LTV) or laser dual focal velocimeter (L2F) works by using two parallel focused laser beams with a known distance. When particles pass through the first of these beams, the time to which it passes the second laser beam is measured. Thereby one can get a measure for the velocity component perpendicular to the beam direction.

4.2.1 Measurement Principle

Figure 4.13 shows a typical LTV system, where a laser beam is split up into two beams by a wollaston prism. The two laser beams are made parallel by a condensing lens, carefully chosen and positioned to obtain the desired beam spacing.

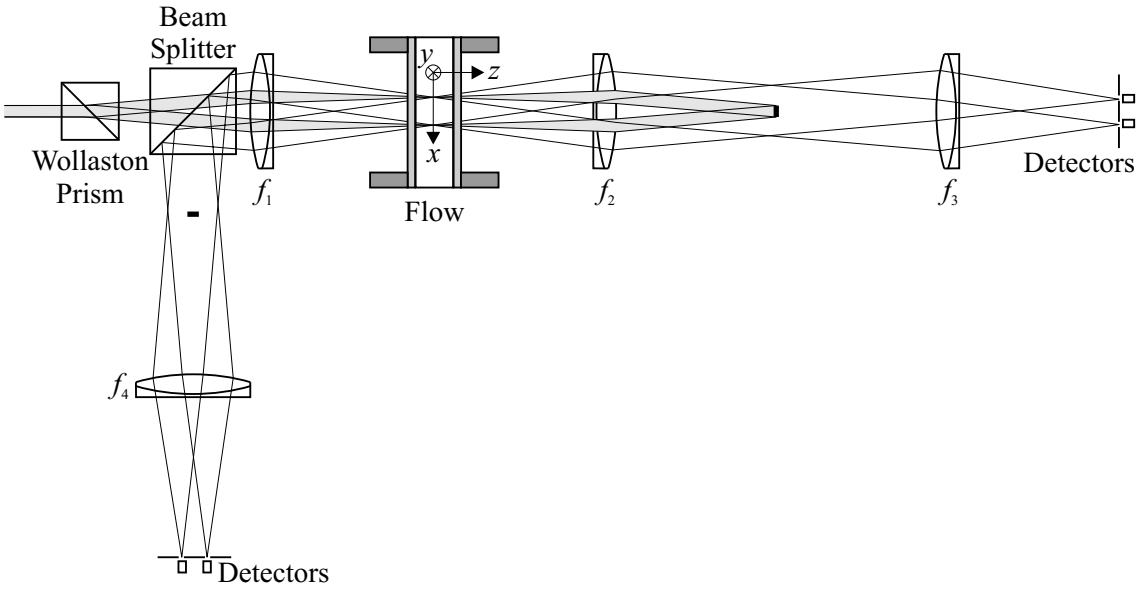

Figure 4.13: Illustration of a typical laser time-of-flight velocimeter system where both the forward scattered and backscattered light is observed.

The figure shows two ways of collecting the light scattered from particles passing through the measurement volume, viz. the forward and backward scattered light. For both configurations, a condensing lens collects the scattered light. This lens directs the light towards another lens, which focuses the two beams onto two detectors. In other words, the light scattered from particles passing through the measurement volume is imaged onto two detectors. Apertures in front of the detectors ensure that cross talk is reduced and preferably removed from the system. Additionally, the size of the apertures can be used to limit the extent of the measurement volume (confocal system).

The LTV system can be used in two different configurations, using backscattered or forward scattered light. The backscattering configuration has the advantage that there only has to be one access window to the flow. Additionally, the receiver system is pre-aligned since the receiver and transmitter are on the same side of the flow. The forward scattering configuration demands two access windows, and the system must be aligned on both sides of the flow, which in some cases may prove difficult. Furthermore, the transmitter and receiver must be moved simultaneously if the system is used to obtain a flow profile across the pipe. However, the backscattering configuration has a disadvantage with respect to efficiency, since the backscattering coefficient is often several orders of magnitude lower than the forward scattering coefficient.

In the focal plane of the collecting lens, a beam stop should be placed so that the direct reflected

light (or transmitted) light is not imaged onto the detectors, which would result in a smaller dynamic range due to saturation of the detectors.

The two detectors both measure a temporal signal originating from the focal areas of the two probe beams, respectively. By cross-correlating the two signals, one obtains a peak around the time delay, τ, between the two signals. This can be converted into a velocity by the following relation:

$$v = \frac{2D}{\tau}\,, \tag{4.15}$$

where $2D$ is the beam spacing, which is known from calibration of the system.

4.2.2 Optical System

The idea of implementing all the functions of a laser time-of-flight velocimeter in a single HOE plane was first proposed in [58] and later for a dedicated flow sensor in Ref. [48]. However, problems with this setup emerged when placing small apertures in front of the detectors in order to reduce crosstalk as well as the extent of the measurement volume. Due to the wavelength dependency of the diffraction angle, one could observe that the signals sometimes would disappear due to mode hops of the laser diode, resulting in the light not being coupled through the apertures.

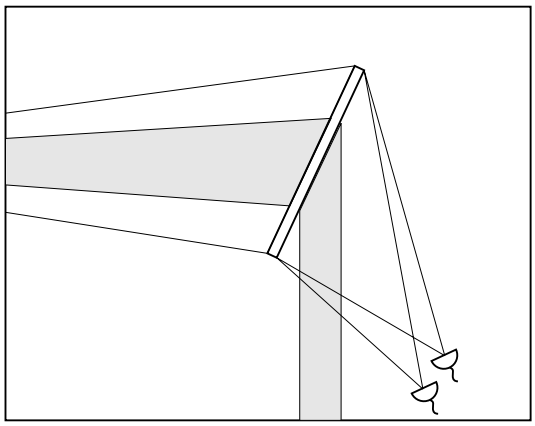

Figure 4.14: Illustration of the old configuration where the transmitter (grey tinted) and receiver had different diffraction angles.

In the LTV sensor presented here, this problem is solved by letting the total deflection angle for the transmitter and receiver HOE be identical. In order to maximise the diffraction efficiency of the gratings, the total deflection angle is set so high that higher order diffractions are suppressed. More precisely, the total deflection angle is set to 90 degrees, which also simplifies the alignment of the HOE. The transmitter HOE is placed in the centre of the HOE plane. Since this HOE has the function of splitting the incoming beam into two beams and focusing them in the plane where measurements are to be performed, the HOE consists of two partially overlapping lens elements. Two receiver HOEs are placed on each side of the transmitter. Since the function of these HOEs are to image the light scattered from the two measurement points to two detectors, the receivers only consist of one lens element. The layout of the transmitter and receiver HOE is depicted in Fig. 4.15 (a).

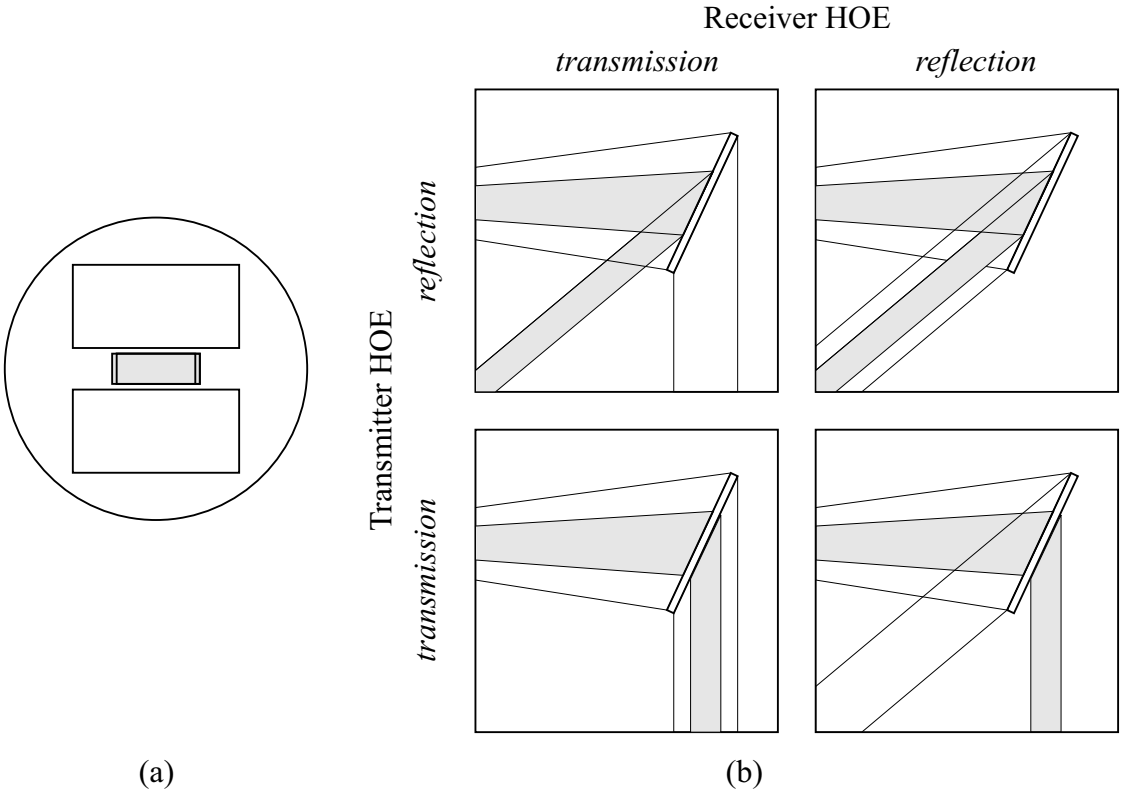

Figure 4.15: (a) The layout of the HOE showing the mutual position of the transmitter (grey tinted) and the receiver. (b) shows the four combinations of implementing the transmitter and receiver.

The HOE is a surface relief hologram and can be implemented in two ways, as a transmission HOE or a reflection HOE. The HOE itself is implemented in photoresist, which makes it obvious to implement the HOEs as transmission holograms. However, by applying a reflective coating to the surface relief structure, they can be used in a reflection setup. The reflection coating could be a thin layer of Au, but other materials such as Al or Ag could also be used. This leaves one with the four possibilities for implementation of the HOE plane as shown in Fig. 4.15 (b).

In many aspects, it would be preferable to implement the transmitter and receiver as different types of holograms, thereby separating the received beam from the incoming beam. However, the coating of the HOE introduces difficulties in the production of the HOE. Therefore, for the sake of simplicity, it was chosen to use transmission holograms both for the transmitter and receiver.

The ambition is to construct an LTV system intended for use in flow pipes with a large diameter (up to DN200) with a measurement precision better than $\pm 0.5\%$. The focal length of the lens element was therefore set to be 160 mm from the centre of the HOE. In order to obtain the desired precision, it was chosen to construct the system with a ratio between the waist diameter and beam spacing to be $w_1/D \approx 0.03$. Through trial of different configurations of the transmitter HOE, a version for which a 22 μm radius for the $1/e^2$ intensity of the two laser beams is obtained with a

beam spacing of approx. 600 μm. It should be noted that if the LTV system were to be used in smaller pipes, it would be desirable to construct the sensor with a shorter focal length. This would mean that the laser beams would have narrower beam waists and thereby a smaller measurement volume, just as the confocal parameter would be smaller as well.

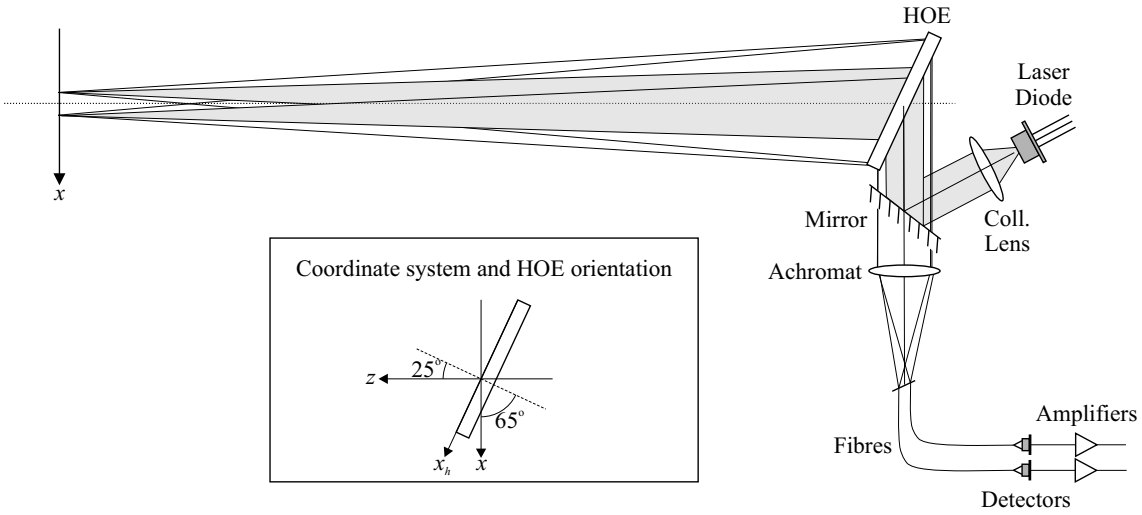

Figure 4.16: The chosen setup for the laser time-of-flight velocimeter.

The resulting design of the LTV sensor is depicted in Fig. 4.16 and can be seen on the photograph in Fig. 4.17. A laser diode operating at 50 mW and 785 nm emits light, which is collimated by a condensing lens. The laser diode and collimating lens are assembled in a cooled and temperature stabilised unit using a Peltier element. The collimated beam is sent to a mirror that directs the light towards the transmitter HOE, which splits the laser beam up into two beams and focuses them at a distance of 160 mm from the centre of the HOE. The angle of incidence is 65 degrees to the normal of the HOE plane and the angle of diffraction is 25 degrees to the normal. The light scattered from particles passing through the two laser beams is collected by the receiver HOEs, which recollimate and send the light past the mirror to the achromat lens. The mirror removes the light that is directly reflected from the access window in the flow pipe. The achromat has a focal length of 40 mm and focuses the two laser beams onto two optical fibre ends. It is necessary to use a refractive lens such that one does not introduce a new wavelength dependency. The fibres are multimode fibres with a core diameter of 50 μm and are positioned in a holder with two v-grooves having a spacing of 320 μm. The edge of the holder is angled 25 degrees since the two beams are not focused in the same plane due to the slight difference in average optical path lengths from the two focal points to the receiver HOEs. The sensor is mounted on specially designed base plate that ensures easy assembly of the system. The sensor can be translated along the propagation direction of the probe beams by the use of a rail system. Thereby, the measurement volume can be positioned at the desired position in the flow under investigation. An electronic ruler monitors the position of the sensor.

With the setup suggested, all the optical components can be placed on the same side of the HOE, which means the effective working distance can be maximised. Additionally, it makes it possible

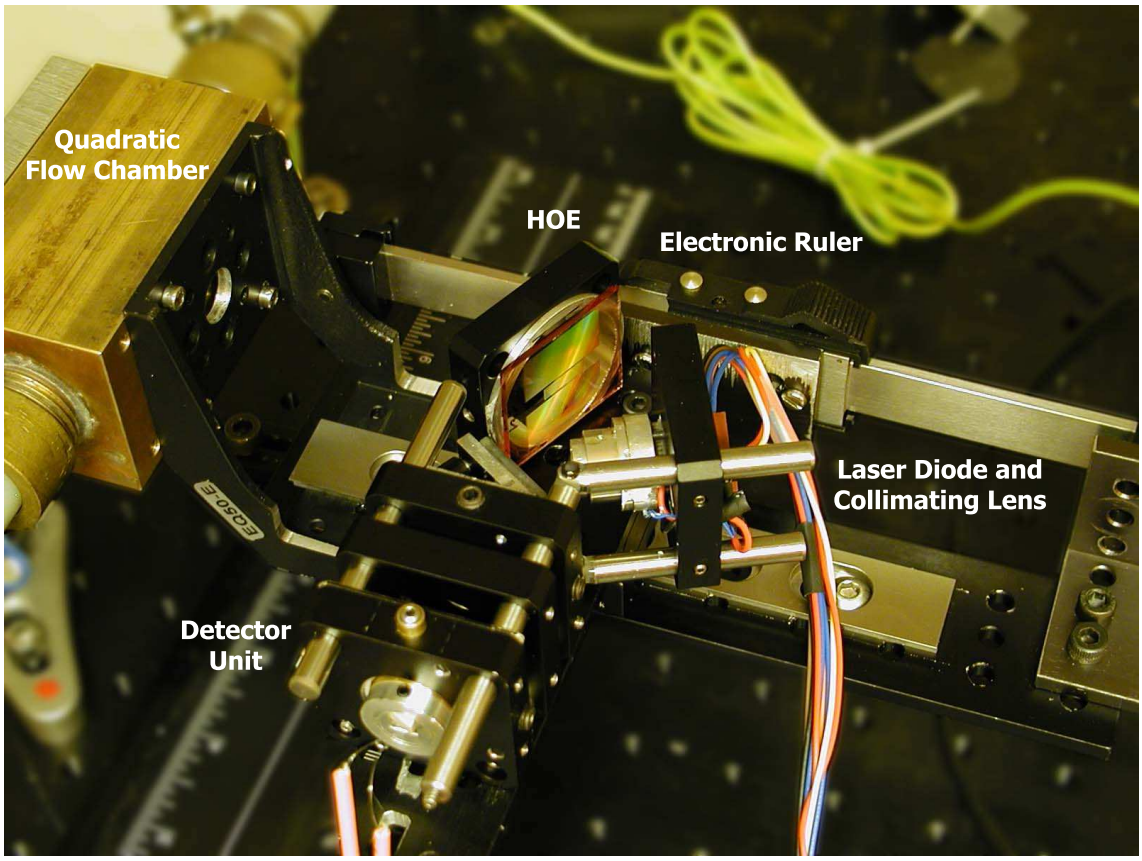

Figure 4.17: Photo of the LTV system.

to construct a compact and robust setup.

Notes on the Production of the HOE

The transmitter HOE is written as two partially overlapping lens elements, both having a 11 mm aperture. Since the total angle of deflection is set to 90 degrees, it is impossible to construct the system so that the HOE plane is parallel to the measurement plane, such as the case of the constructed common-path interferometer (see Sec. 3.2). This somewhat complicates the writing process of the HOE (as well as alignment of the system). In order to obtain the interfocal distance of 600 μm between the two beams, it means that the film should be shifted 662 μm between exposures due to the 25 degrees angle of the HOE plane compared to the measurement plane. However, this angle also makes it necessary for the different lens elements to have a different focal lengths in order for both beams to be focused in the measurement plane.

The (x,z)-coordinates in Fig. 4.16 for the centre of the two transmitter lens elements are therefore $(-300,-139.9)$ and $(300,139.9)$ μm, respectively, while the receiver HOEs have the coordinates $(0,0)$.

The radius of curvature and centre angle of incidence for the two writing beams have been found using an aberration balancing scheme for a desired construction and image beam (see Sec. 2.3). The sizes of the writing parameters are listed in Tab. 4.1.

	writing Beam #1		**writing Beam #2**		**Focal Length**
	R_0 [mm]	α_0 [deg]	R_R [mm]	α_R [deg]	f [mm]
Transmitter Lens #1	-213.867	23.8608	-864.451	-20.0639	159.8601
Transmitter Lens #2	-214.241	23.8608	-865.963	-20.0639	160.1399
Receiver Lenses	-214.054	23.8608	-865.207	-20.0639	160.0000

Table 4.1: The writing parameters for the constructed HOE.

The different writing parameters for the lens elements accommodate for the lenses needing to have different focal lengths in order to focus in the same plane.

Wavelength Dependency

The HOEs are written using a interferometric writing setup in photoresist. In the writing technique, two laser beams are used, and the resulting period, Λ_C, of the gratings across the HOE will depend on the angle of illumination and curvature of phase fronts for the two writing beams in the following way,

$$\Lambda_C(x_h) = \frac{\lambda_0}{\sin\alpha_R(x_h) - \sin\alpha_0(x_h)} \tag{4.16}$$

where λ_0 is the wavelength of the writing beams and α_R and α_0 is the angle of incidence for the reference and object beams across the HOE, respectively.

Similarly, the grating period of the HOE must comply with the desired image properties according to the following expression:

$$\Lambda_C(x_h) = \frac{\lambda_C}{\sin\alpha_C(x_h) - \sin\alpha_I(x_h)} \tag{4.17}$$

where λ_C is the applied wavelength, and α_C and α_I are the angle of incidence and diffraction of the reconstruction beam and image beam, respectively.

Furthermore, the following relations applies to the focal length and angle for the image beam in imaging holography:

$$R_I = \frac{1}{\frac{1}{R_C} + p\mu\left(\frac{1}{R_0} - \frac{1}{R_R}\right)} \tag{4.18}$$

$$\alpha_I = \arcsin\left(\sin\alpha_C + p\mu\left(\sin\alpha_0 - \sin\alpha_R\right)\right) \tag{4.19}$$

where $\mu = \lambda_c/\lambda_0$ and $p = \{1, -1\}$ describes the real and virtual image, respectively.

By observing Eq.(4.18) and (4.19) one can obtain an estimate of how much the measurement volume and the individual focal points move as a result of wavelength fluctuations. As can be seen from Eq. (4.18), the focal length is inversely proportional to the operation wavelength, while Eq. (4.19) shows that the diffraction angle is approximately proportional to the operation wavelength for small fluctuations. This means that the measurement volume moves along a straight line for small changes in the operation wavelength. More precisely, the x- and z positions of the two focal points move as depicted in Fig. 4.18.

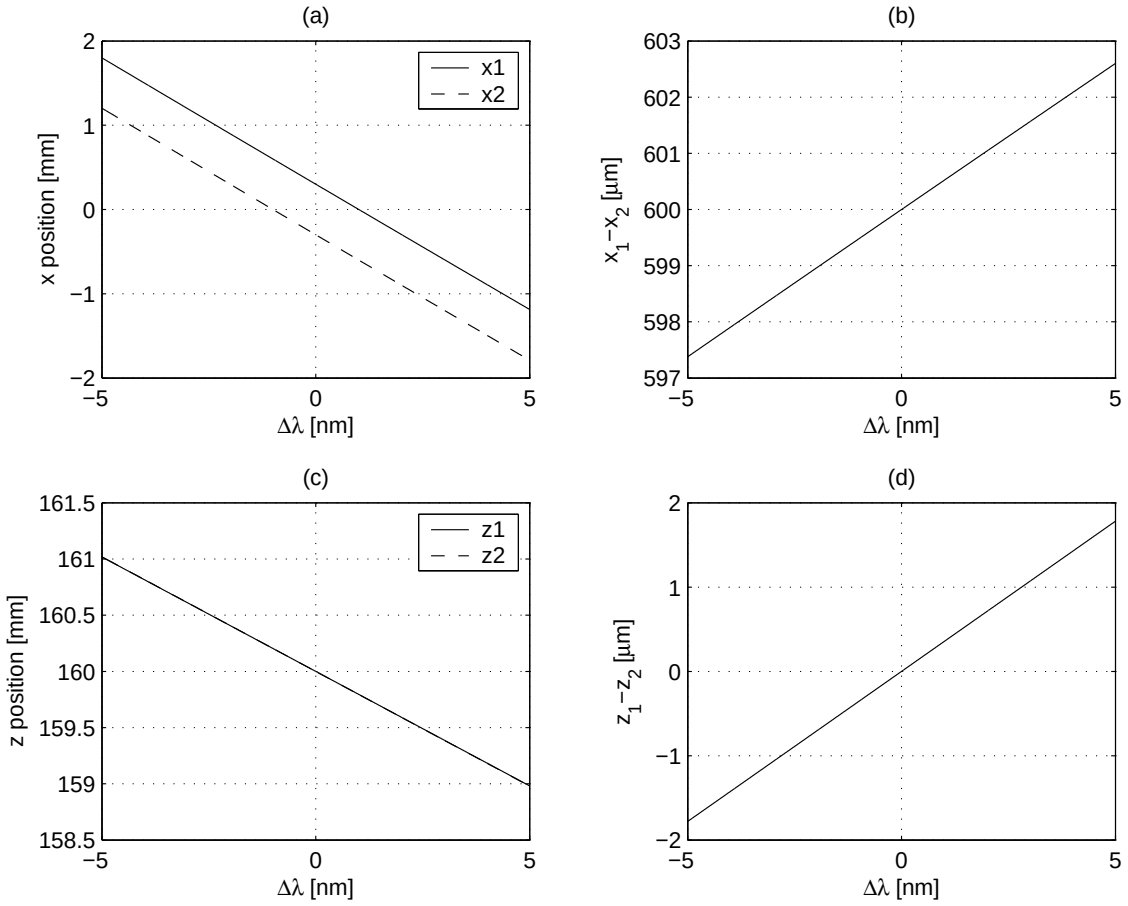

Figure 4.18: The movement of the measurement volume as a function of the change in wavelength. (a) shows the x-position of the two beam waists, (b) the x-distance between the two waists, (c) the z-position of the two beams (nearly coinciding), and (d) the z-distance between the two waist points.

Since the two beams have a slight difference in focal lengths, their wavelength dependency will also be slightly different. With regards to the location of the measurement volume across the flow pipe (the z-direction) it can be seen from Fig. 4.18 (c) that the measurement volume moves approximately 1 mm for a 5 nm wavelength shift. For a ± 0.3 nm shift (corresponding to a mode hop), the measurement volume moves 61 μm. This will of course influence the precision with which the flow profile across the pipe can be determined. In return, the difference between the z-positions of the two waists does not vary much – only 1.78 μm for a 5 nm shift in wavelength,

which is much smaller than the confocal parameter.

The movement of the measurement volume along the flow pipe (the x-direction) is as much as 1.5 mm for a 5 nm shift in wavelength. This, however, does only have a negligible influence on the precision of the measurements, since it is the profile across the pipe, which is of interest. The interfocal distance, however, is another matter entirely. It is seen that the spacing changes 2.6 μm for a 5 nm shift in wavelength, which introduces a measurement error of 0.43%. For a $\pm$0.3 nm shift in wavelength, the corresponding change in beam spacing is 0.16 μm. This introduces a measurement error of 0.026%, which is well below the precision that we try to obtain.

Temperature Dependency

We here examine what effect the changes in the ambient temperature have on the measurement volume. Only the effect due to expansion or contraction of the HOE is analysed and not the effect on the characteristics of the laser diode or the collimation.

We will restrict ourselves to look at the interfocal distance along the flow direction, since the analysis of effects due to wavelength fluctuations showed that the predominant effect on the precision of the measurements are found here. The expansion of the HOE has two effects on the interfocal distance. First of all, the two lens elements move further apart as the temperature increases, which means that the focal points also will move further apart according to the following expression:

$$\frac{\Delta D}{D} = \alpha \Delta T \,, \tag{4.20}$$

where α is the linear thermal expansion coefficient for the grating material and ΔT is the change in temperature.

Secondly, the imaging of the individual lens elements change due to the grating period across the HOE being larger. To a first approximation, the expansion of the HOE corresponds to a reduction of the operating wavelength in the following way,

$$\lambda_{c,res} = \frac{\lambda_c}{1 + \alpha \Delta T} \,. \tag{4.21}$$

As can be seen from the analysis of the wavelength dependency, a decrease in the operating wavelength will result in the two focal points moving closer to each other as can be seen from Fig. 4.18. Since the expansion of the HOE can be perceived as a decrease in wavelength, this means that the expansion also counteracts the fact that the centre of the lens elements move apart, thereby reducing the effect of the temperature fluctuations. The total effect of the temperature fluctuations are found using Eq. (4.18)-(4.21) and is depicted in Fig. 4.19.

As can be seen from the from Fig. 4.19 the temperature dependency is very dependent on the chosen material for the HOE. However, even for the choice of polycarbonate, the interfocal distance only changes 0.045% for a 25 centigrades change in ambient temperature. The effect from fluctuations in the wavelength of the laser diode is therefore seen to be considerably more dominant. Table 4.2 shows the linear thermal expansion coefficient for relevant materials and the maximum allowed change in temperature in order to keep the relative uncertainty, $\Delta(2D)/2D$, below 0.01%.

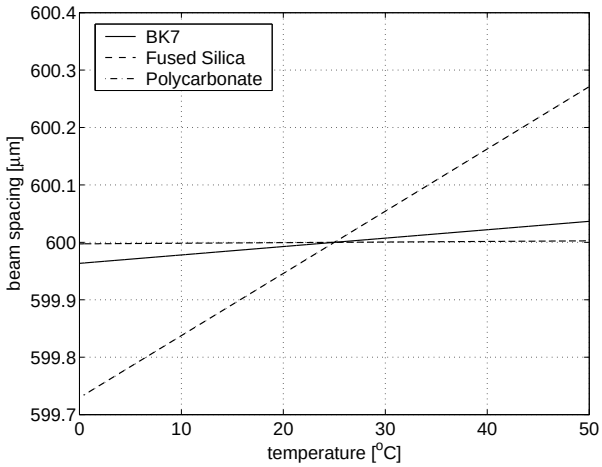

Figure 4.19: The beam spacing along the flow direction as a function of the temperature assuming the system is designed for use at 25 degrees centigrade.

Material	α [10^{-6} K^{-1}]	$\Delta T_{0.01\%}$ [K]
BK7	7.7	41
Fused Silica	0.55	574
Polycarbonate	57	5.54

Table 4.2: Linear thermal expansion coefficient and the maximum allowed temperature shift .

4.2.3 Measurement Volume

In this section we will throw light on how the appearance of the measurement volume influences the measurements and how one optimises the design. Matters that have influence on the characteristics are the degree of turbulence within the measurement volume, the velocity gradient and the angle of acceptance for the measurement system. It should be noted that the following analysis assumes dealing with Gaussian laser beams. The focal plane of the two laser beams as well as the flow direction are assumed to be along the x-axis. The waist radii, w_1 and w_2, are aligned along the x- and y-axes, respectively and are assumed to be identical for the two laser beams. The two semi-axes of the beam waist will normally be different for a laser diode, thereby obtaining an elliptical focus as illustrated in Fig. 4.20.

The distance between the two laser beam is denoted $2D$, while the confocal parameter, $2z_r$, is twice the size of the Rayleigh length and is given by:

$$2z_R = \frac{2\pi n w_1^2}{\lambda}, \tag{4.22}$$

where λ is the wavelength and n is the refractive index of the medium.

As can be seen from Eq. (4.22) one cannot design the two parameters z_R and w_1 independently. In

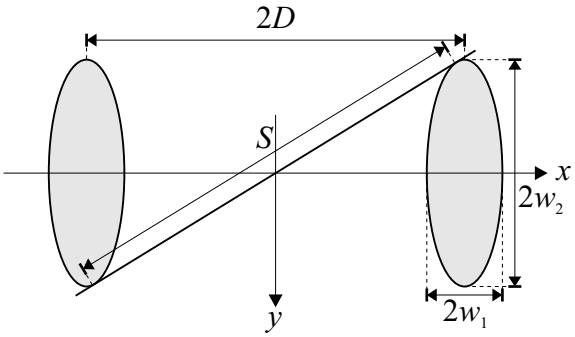

Figure 4.20: Illustration of measurement volume and the parameters used to describe the characteristics.

return, the extent of the measurement volume along the z-axis can be reduced by placing apertures in front of the detectors.

The measurement volume is depicted in Fig. 4.20. In the characterisation of the measurement volume, we use two quantities, viz. the ratio between the waist size, w_1, along the x-axis, and the distance between the two beams, $2D$, and the ratio between the two semi-axes of the beam waist, w_1/w_2. The ratio between the two semi-axes will for the laser diodes we are using be approximately 1:3 and the divergence between the two axes is approximately inversely proportional to this ratio.

Focusing

The size of the two waist points is determined by the desired size for the integration volume in the flow pipe. Additionally, there is a demand for sufficient intensity in the two beams in order for the scattered light to be detectable. This is especially important when using a backscattering configuration due to the lower amount of light compared to a forward scattering configuration. The measured power, P_d, at the detector will be given by the following relation:

$$P_d = 2S_s \frac{P_0}{\pi w_1 w_2} T_t T_r \,, \tag{4.23}$$

where the suffixes, s, r, and t, denote scattered, receiver, and transmitter, respectively, P_0 denotes the power of the light source, T is the transmittance of the HOE in the applied diffraction order, and S_s is a scattering coefficient that depends on the size of the collector lens or HOE.

In Fig. 4.21 the received power, P_d, is plotted as a function of the waist size, w_1, for different ratios between the two waists, w_2/w_1. The power of the laser diode, P_0, is assumed to be 50 mW and S_s is 10^{-4} and 10^{-7} mm^{-1} for the forward and backward scattering configuration, respectively. The values for the scattering coefficient are found from an earlier time-of-flight experiment. The transmitter efficiency is assumed to be 10% (for each beam) and the receiver efficiency to be 40%. If, for instance, the demand for the minimum detected power is 1 μW, then it is seen that the semi-axis has to be smaller than 8.2 μm for a backscattering configuration where $w_2/w_1 = 3$.

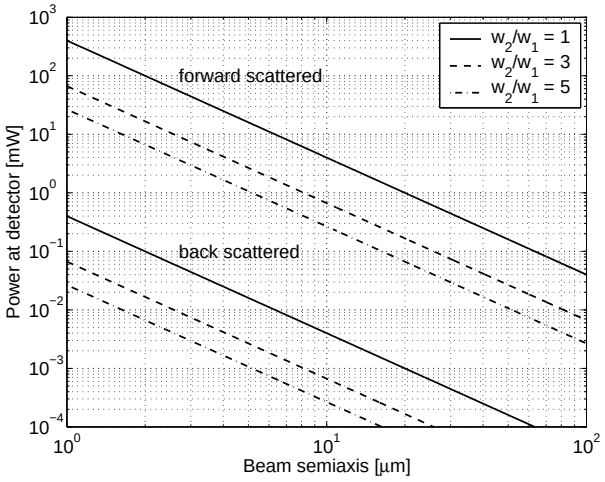

Figure 4.21: Calculated power received as a function of the semiaxis of the waist in a back scattering and forward scattering configuration, respectively.

Beam Spacing

When the flow is turbulent, not all particles passing through the first laser beam will necessarily pass through the second laser beam as well. The larger the degree of turbulence, the smaller the probability will be that the particle will contribute to a successful measurement of the velocity. The spacing between the two beams has to be designed so that a desired accuracy of the measurements is obtained and at the same time the angle of acceptance must match the turbulence conditions.

The probability, p_I, for a particle to contribute to the velocity measurement depends on the degree of turbulence and the spacing between the two beams. Due to the Gaussian intensity profile of the laser beams, this probability will depend on where the particle passes through the focal points. The probability, p_I, can consequently be approximated by the intensity distribution in the beam waist [88],

$$p_I(\Delta\alpha) \approx \frac{I(y)}{I_0} = \exp\left[-\frac{(\Delta\alpha)^2}{2\sigma_d^2}\right] \quad , \quad \sigma_d = \frac{w_2}{2D}\,, \tag{4.24}$$

where it has been used that $\Delta\alpha = y/D$.

The probability distribution function for a flow direction, $\Delta\alpha$, in a turbulent flow is denoted p_α. The probability will approximate a normal distribution,

$$p_\alpha(\Delta\alpha) = \frac{1}{\sqrt{2\pi}}\frac{1}{\sigma_\alpha}\exp\left[-\frac{(\Delta\alpha)^2}{2\sigma_\alpha^2}\right] \tag{4.25}$$

where the standard deviation, σ_α, assuming an isotropic turbulence, can be approximated with the turbulence intensity, Tu, which is given by the ratio between the standard deviation of the velocity measurements and the average measured velocity [88].

The probability, p_d, of a successful time-of-flight measurement is thereby given by the following expression:

$$p_d = \int_{-\infty}^{\infty} p_\alpha \, p_I \, d(\Delta\alpha) = \frac{1}{\sigma_\alpha} \frac{1}{\sqrt{\frac{1}{\sigma_\alpha^2} + \frac{1}{\sigma_d^2}}} = \frac{1}{\sqrt{1 + \left(2 \frac{D}{w_1} \frac{w_1}{w_2} Tu\right)^2}} \,. \tag{4.26}$$

The probability for a successful time-of-flight measurement is plotted as a function of the turbulence in Fig. 4.22 intensity for different values of w_1/D and w_2/w_1.

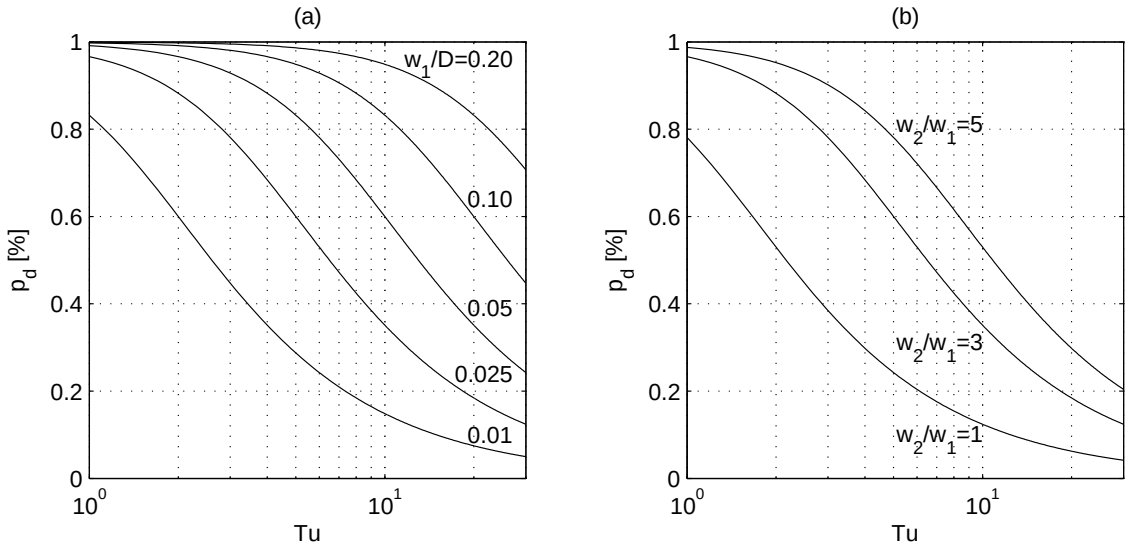

Figure 4.22: Plots of the probability of detecting particles as a function of the degree of turbulence. Graph (a) depicts the probability for different values of w_1/D and $w_2/w_1 = 3$ and (b) for different values of w_2/w_1 and $w_1/D = 0.025$.

Normalised Measurement Error

The normalised measurement error, ϵ_s, of the particle velocity when the particle passes through the measurement volume under the maximum angle of acceptance compared to the when the particles pass at $\Delta\alpha = 0$ is given as follows:

$$\epsilon_s = \frac{2D - S}{2D} = 1 - \sqrt{1 - \left(\frac{w_1}{D}\right)^2} \sqrt{1 + \left(\left(\frac{w_2}{w_1}\right)^2 - 1\right)\left(\frac{w_1}{D}\right)^2} \,. \tag{4.27}$$

The measurement error is plotted as a function of the ratio between the waist diameter and the beam spacing for different values of ellipsity in Fig. 4.23. Note, however, that the measurement error is positive for circular beams (one measures a too high velocity component, since $S < 2D$), while the error is negative for the ellipses.

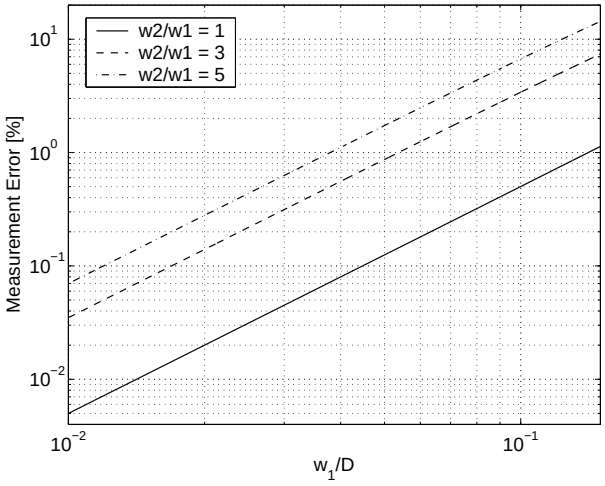

Figure 4.23: The normalised error in measured velocity of a particle passing through the measurement volume at the maximum angle of acceptance compared to the measurement if the particle had passed through in the angle $\Delta\alpha$ = 0.

If one wishes to have a system with measurement errors smaller than 1%, it can be seen that the ratio, w_1/D, must be less than 0.141 for a system with circular focal points. In a system with an elliptical focus, the ratio must be less than 0.054 and 0.038 for w_2/w_1 equal to 3 and 5, respectively. Equivalently, if one wishes to obtain a system with an accuracy better than 0.2% the corresponding values of w_1/D should be less than 0.063, 0.024, and 0.017, respectively. Consequently, the two elliptical configurations presented need a larger relative distance between the two beams in order to obtain the same accuracy as a system with circular beam waists.

Another limitation of the ratio between w_2 and $2D$ is the fact that this ratio dictates a lower limit for measurable degrees of turbulence. Consider for instance the situation, where a laminar flow is to be measured. The beams can be oriented in a certain angle range where measurements can be obtained. Consequently, a probability distribution function, $p_{\alpha,meas}$, with a standard deviation, $\sigma_d = w_2/2D$, is measured, suggesting a degree of turbulence that in fact does not exist. Provided that Eq. (4.25) describes the real angle distribution in the flow, one can show that the measured standard deviation will depend on both σ_d and σ_α through the following relation:

$$\sigma_{\alpha,meas} = \sqrt{\sigma_d^2 + \sigma_\alpha^2}\,. \tag{4.28}$$

Remembering that the turbulence intensity can be approximated to σ_α, then using Eq. (4.26) it follows that,

$$Tu_{meas} \;=\; \sqrt{Tu^2 + \left(\frac{w_2}{2D}\right)^2}\,, \tag{4.29}$$

from which one can find the true turbulence intensity, knowing the geometrical properties of the system, provided that the turbulence intensity is larger or equal to $\sigma_d = w_2/2D$. As a consequence, small values of the ratio between w_2 and D are required in flows of low turbulence, while higher values can be tolerated for higher degrees of turbulence.

4.2.4 Statistics for LTV Measurements

A measurement will consist of n observed time delays or velocities of particles passing through the measurement volume. Each of these observations can be presented by a random variable X_i. If these random variables are independent, then according to the central limit theorem, the sum of these observations, Z_n will be normally distributed with the mean value μ and variance σ^2 when the number of observations are large [89],

$$Z_n = \frac{\sum_{i=1}^{n} X_i - n\mu}{\sigma\sqrt{n}} = \frac{\sqrt{n}}{\sigma}\left(\overline{X} - \mu\right) . \tag{4.30}$$

The maximum likelihood estimator for μ will be given by:

$$\overline{X} = \sum_{i=1}^{n} \frac{X_i}{n} . \tag{4.31}$$

However, one cannot be certain that the sample average, $\overline{X}$, is exactly equal to μ. We can only be certain that the calculated average is close to μ and that we are confident that we get closer to the correct value the more observations we use for our calculation. Therefore, it is more valuable to be able to describe an interval that we have a certain degree of confidence that μ will lie within.

We can obtain a desired degree of confidence by using the following probability:

$$P\left\{Z > z_\alpha\right\} = \alpha = 1 - \Phi\left(z_\alpha\right) , \tag{4.32}$$

where

$$\Phi(z_\alpha) = \frac{1}{\sqrt{2\pi}} \int_{-\infty}^{z_\alpha} \exp[-\frac{y^2}{2}] \tag{4.33}$$

for Z being a unit normal.

Thereby one can get the following two-sided confidence interval by using the following expression:

$$P\left\{-z_{\alpha/2} < Z < z_{\alpha/2}\right\} = 1 - \alpha . \tag{4.34}$$

Thereby one can derive the following expression by using and rewriting Eq. (4.30),

$$P\left\{\overline{X} - z_{\alpha/2}\frac{\sigma}{\sqrt{n}} < \mu < \overline{X} - z_{\alpha/2}\frac{\sigma}{\sqrt{n}}\right\} = 1 - \alpha . \tag{4.35}$$

In other words, there is a $100(1-\alpha)$ percent probability that μ will lie between $(\overline{X} - z_{\alpha/2}\frac{\sigma}{\sqrt{n}})$ and $(\overline{X} + z_{\alpha/2}\frac{\sigma}{\sqrt{n}})$.

If one wishes to have a system with a relative uncertainty, δ, for the measurement of the mean velocity, then it follows from Eq. 4.35 that in order to obtain a $(1-\alpha)$ confidence level for the mean velocity lying within the interval $[\overline{X} - \delta\mu \; ; \; \overline{X} + \delta\mu]$ that the relative uncertainty is given by:

$$\delta = \frac{z_{\alpha/2}}{\sqrt{n}} Tu , \tag{4.36}$$

where it has been used that the turbulence intensity is equal to the relative standard deviation, $Tu = \sigma/\mu$.

The expression above can be used to calculate the necessary number of observations in order to obtain a desired uncertainty with a given confidence level in a flow with a known turbulence identity,

$$n = \left(\frac{z_{\alpha/2} Tu}{\delta} \right)^2 . \tag{4.37}$$

Figure 4.24 depicts the necessary number of observations as a function of the turbulence intensity. The calculations have been made for δ = 0.1, 0.5, and 1%, respectively, using Eq. (4.37). The confidence level was set to 95%, which means that $z_{\alpha/2} = 1.96$ using Eq. (4.32) and (4.33). The full-drawn lines show the number of particles that pass through both beams, while the dashed lines shows the calculated number of particles (passing through the first beam), where the probability for a particle passing through both laser beams and successfully contributing to the measurement has been included (see Eq. (4.26)). The calculations are made for a system with elliptical beam waist with $w_2/w_1 = 3$ and $w_1/D = 0.02$.

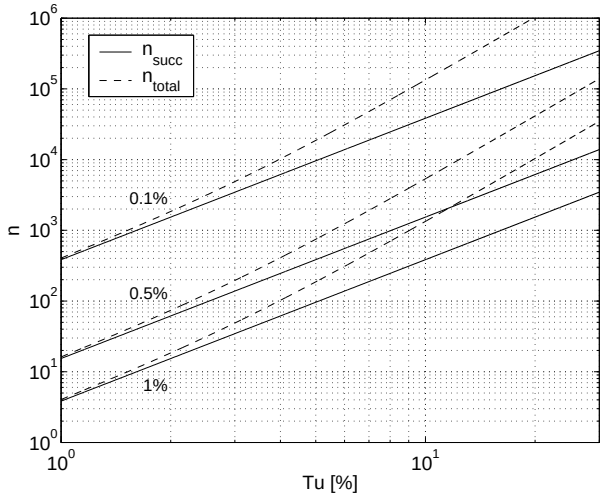

Figure 4.24: Calculated number of observations needed to obtain a relative uncertainty of 0.1, 0.5, and 1%, respectively with a confidence level of 95%.

This means that in order to obtain a relative uncertainty of 0.1%, 0.5% and 1%, respectively, under conditions where the turbulence intensity is equal to 10% that 13369, 5348, and 1337 observations are needed, respectively.

4.2.5 Signal Processing

The digital signal processing (DSP) in optical flow sensors is extremely important, since the measurement accuracy often relies on the DSP. In the system described here, the DSP has to be very flexible, since a high dynamic range is required on velocity measurements (1:10,000). This also implies the need for variable integration and sampling times, so that a similar measurement accuracy is obtained over the entire dynamic range.

For the purpose, a special DSP card was developed for this use. The card has two analogue to digital converters that can sample at 500 kHz with a 8 bit resolution. A PC frontend to perform flow measurements was created using LabView. Screen dumps from the LabView program can be seen in Fig. 4.25 and Fig. 4.26.

Figure 4.25: Screen dump from the written LabView program. The program is the PC frontend of the flow sensor. The top left window is a plot of the correlation string. The top right windows shows the correlation string in the velocity space and the Gaussian fit to this string. The bottom window shows the history of velocity measurements.

The program was made so that it changes the sample rate according to the last obtained valid velocity measurement. The sample rate can have any value, $f_s = 500/i$ kHz, where i is a positive integer. Provided that the flow sensor does not detect a flow velocity at the given sample rate, a scanning procedure begins. This scanning procedure, starts by detecting for high flow velocities (at high sampling rates). If the sensor does not detect any unambiguous velocity, the sampling speed changes to a lower velocity range. This procedure continues until an unambiguous flow velocity is measured. Once this has been obtained, the sampling rate is determined from the measured velocity such that the delay time is approximately 200 sample intervals, which gives a relative uncertainty of $\pm 0.25\%$.

The sampled detector signals are clipped to binary signals, the signal getting the value 0 if it is below a pre-defined threshold value and 1 if it above the threshold value. The signal processing can now be performed in various ways.

Correlation Calculations

The cross-correlation between the two detector signals are calculated using a special Fast Fourier Transformation (FFT) routine implemented in a programmable logical device (PLD). This routine enables real-time correlation using one bit XOR, OR, and AND operations. The total correlation string is a 256 element array. The correlated signals from the second detector are delayed 50 samples compared to the first detector signals, thereby avoiding the correlation peak around $\tau = 0$ and in the same process getting a higher precision.

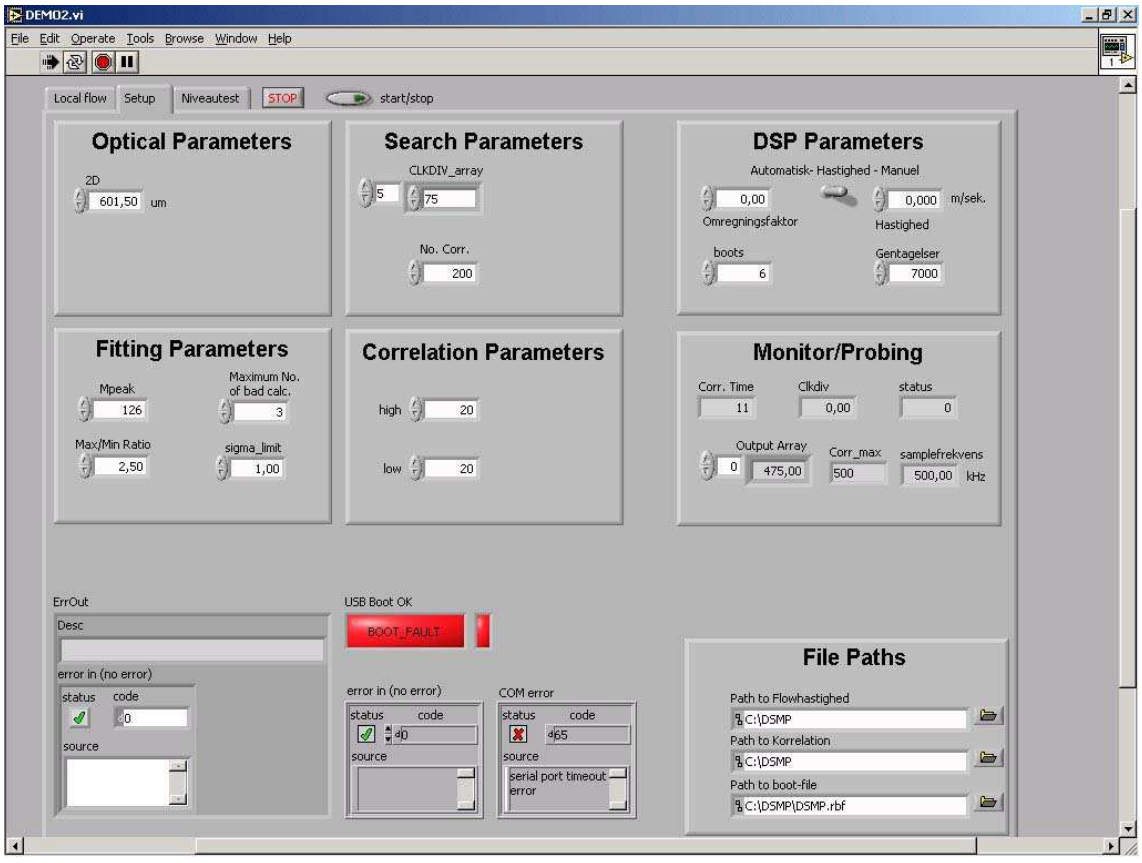

Figure 4.26: Screen dump from the written LabView program. The setup-page shows the many variables that can be set in the flow measurement program.

In order to get a better estimate of the time delay between the two detector signals, one can apply a non-linear curve fit to the cross-correlation function. It has been chosen to implement three different fitting functions to choose from,

- Gauss function
- Slanted Gauss function (Gaussian in the velocity space)
- triangle function

The correlation functions well, and when measuring on solid surfaces, a normalised correlation coefficients [90] close to 1 can be obtained. Even for measurements on water flows, a correlation coefficient above 0.8 can be obtained.

However, the light scattering particles in the water flow will generally have many different sizes, which results in the detector signals having varying peak values. A few large particles will result in large signal peaks and a good correlation, which thereby will have high weighting in the total correlation function compared to the contributions from smaller particles. Since larger particles do not follow the flow as well as small particles, the measurements can be biased towards a wrong velocity, since a large time delay (and thereby a lower velocity) is detected.

Signal Clipping and Threshold Levels

In order to reduce the influence from the larger particles on the velocity measurement, one can introduce hard clipping of the detected signals. This can be done analogue by increasing the detector gain. However, there is a limit for how high this can be set. In the created LabView program, it is done digitally by an on-off clipping determined by a threshold level. If the sampled signal has a value above the threshold, a signal having the value 1 is generated, and 0 if the sampled value is below the threshold. The cross-correlation is subsequently calculated between the clipped (or binary) signals.

If the correlation coefficient for the unclipped signals are high, then the correlation function for the binary signals will take a triangular shape. In principle, this could help one get a more accurate estimate of the time delay between the two signals, due to the discontinuity of the correlation function [91]. Even for flows with a lower correlation coefficient, the hard clipping can help on the precision of the measurement, since the weighting of the large particles takes the same weighting as the smaller particles in the calculation of the cross correlation function. This will decrease the bias error introduced due to large particles with a high slip compared to the flow. Additionally, the threshold level can be set so that the effect from optical or electrical noise in the system is reduced significantly.

Furthermore, it is an advantage to perform the FFT calculations on 1 bit signals with respect to calculation time compared to 8 bit signals and can only be done this way in the PLD.

Auto-correlation

It should be noted that signal processing can be simplified by using only one detector and calculating the autocorrelation function instead. The detector apertures in front of the detector, however, must be the same as for a cross-correlation system in order to reduce the extent of the measurement volume.

The problem with this method is that the unavoidable peak around $\tau = 0$ can be so wide that

it overlaps the correlation peak around the wanted time delay τ'. This will give rise to a reduction in accuracy for the determination of τ' and thereby also the velocity. The advantage of the method is that only a single signal is to sampled and that only the autocorrelation is to be calculated.

4.2.6 Measurements

This subsection describes the measurements performed on and with the laser time-of-flight sensor. The purpose of the measurements is to examine how the optical system compares to the design specifications and thereby how the system is expected to perform. Finally, the system is also tested in flow measurements in order to estimate its applicability as well as the created LabView program.

The Measurement Volume

The measurements on the measurement volume are performed to get an estimate of the parallellity of the two probe beams as well as measuring the confocal parameter.

The measurements are performed using a Photon Inc. beam scanner. The beam scanner is translated through the measurement volume in fixed steps of 0.1 mm and for each position 5 beam scans are made. The measurements through the volume looks like the waterfall plot shown in Fig. 4.27.

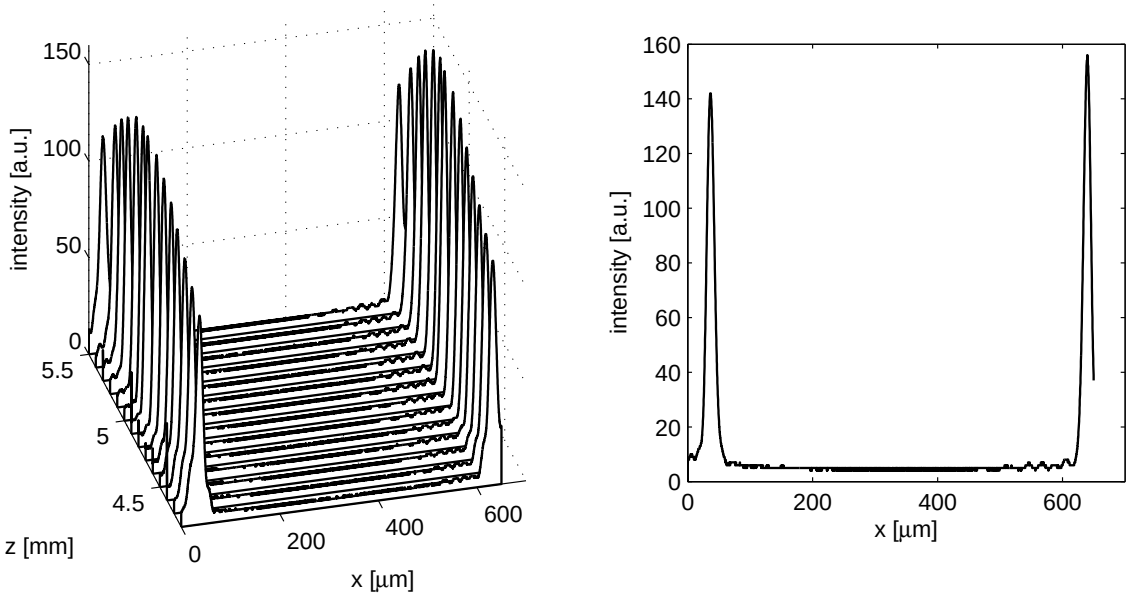

Figure 4.27: A waterfall plot (left) of beam scans made in fixed steps of 0.1 mm through the measurement volume. The plot on the right side shows a single beam scan.

The measurements are analysed by a program created in MATLAB. The program detects the peaks and makes a Gaussian fit to the peaks and returns the waist radius and spacing between the peaks. The results from the signal processing is shown in Fig. 4.28.

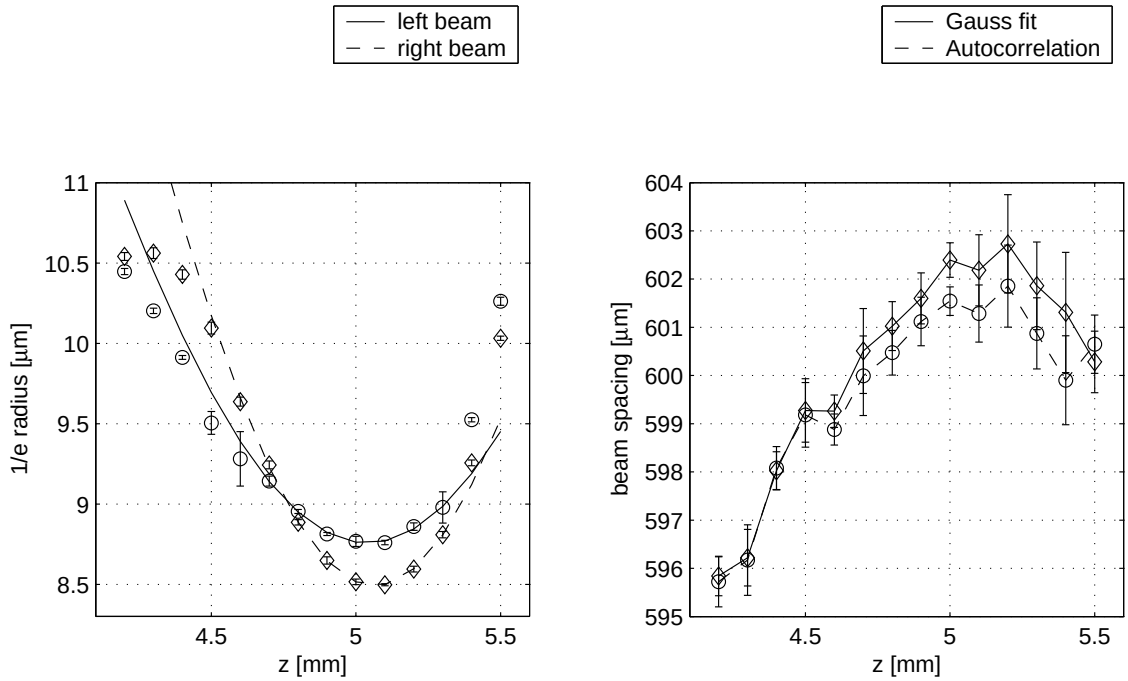

Figure 4.28: The measured widths of the probe beams and the beam spacing as a function of the propagation direction.

The average beam spacing from ± 0.45 mm of the beam spacing is measured to be 601.54 μm with a standard deviation of 0.84 μm using the Gaussian fitting function. The same values found, using a Gaussian fit to the autocorrelation function, show the average beam spacing to be 600.85 μm with a standard deviation of 0.67 μm. The latter value is probably a better estimate of the standard deviation one could expect from particles passing through this part of the measurement volume, since the autocorrelation function is closer to the signal processing one would perform when detecting the scattered light from the volume. That is, one can expect a relative measurement accuracy of 0.11%. It should be noted that the z-axis relate to the position of the translation stage on which the beam scanner head was mounted.

	Beam #1	Beam #2
w_0	8.75726	8.49127
z_0	5.03909	5.06433
M^2	0.78017	0.97334
λ	0.785	0.785

Table 4.3: Values for the fitting parameter for the two probe beams.

It can be seen that the waist radius is approximately 8.5 μm and the confocal parameter is found

to be approximately 1.2 mm. Furthermore, it is seen that the two beams are focused in the same plane. It should be noted that the value of M^2 is found to be smaller than 1, which it ought not be. This value is probably due to the fitting routine, where the Gaussian function is only fitted to the the scan values around the top of the peak. The M^2-value indicates that the probe beams are not perfectly Gaussian, in which case M^2 would equal 1.

Detector plane

The measurements on the signals in the detector plane were performed in the same way as the measurements on the measurement volume, viz. translating a beam scanner in fixed steps in the propagation direction, for each position taking 5 measurements and subsequently processing and analysing the data. The measurements was performed by placing a pitchable mirror in the centre of the measurement volume. First, the mirror was angled such that the reflected light was sent through the lower receiver HOE. With the mirror in this position, a measurement series was carried out, measuring the radius of both semi-axes for both detection beams. Afterwards, the mirror was tilted upwards, such that the reflected light was collected by the upper HOE, and the same measurement procedure was repeated. The results from the measurement and postprocessing are shown in Fig. 4.29.

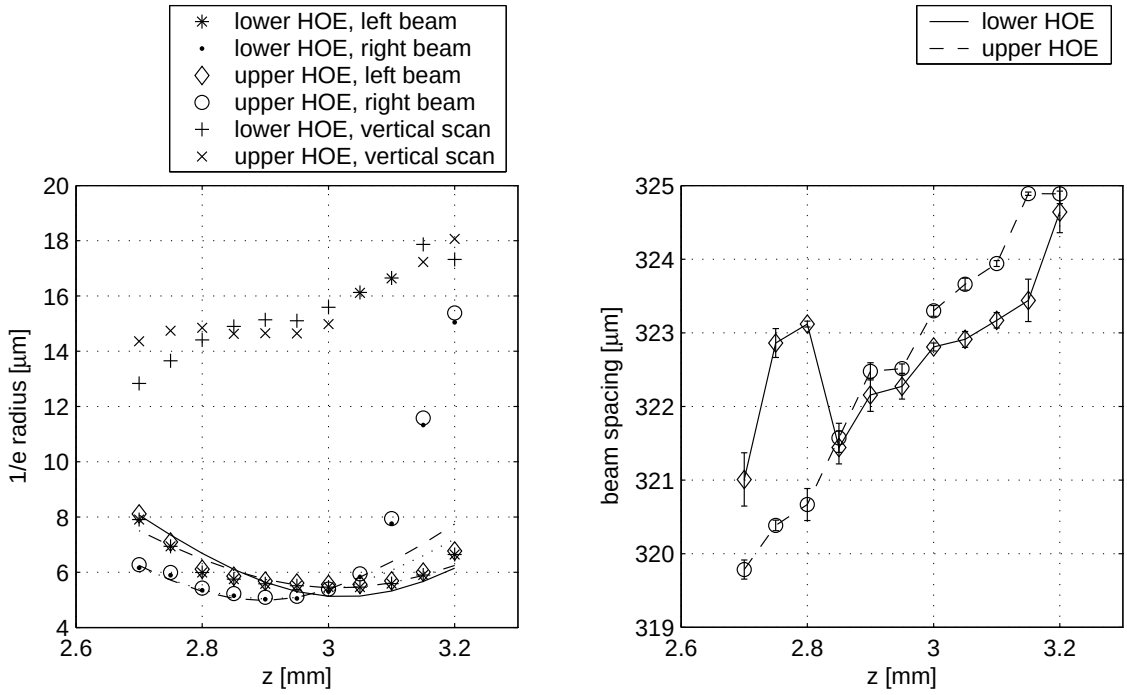

Figure 4.29: The measurements on the detector volume.

It is seen from Fig. 4.29 that the focal points of the beams collected by the two collector HOEs are coincident. It is also seen from the curve fits that the two beams are separated by a distance of approximately 0.13 mm along the propagation direction. Furthermore, it is seen that the two beams are separated with a spacing of approximately 322 μm, which is close to the design spe-

cifications. This in turn, means that the angle between the two focal points is approximately 22 degrees, which is close to the 25 degrees angle of the edge of the fibre holder.

The 1/e intensity waist radii for the four beams are seen to vary between 5.0 and 5.4 μm (equivalent to an 1/e^2 intensity radius of 7.1-7.6 μm). The vertical scan shows that the 1/e intensity beam radius equals approximately 15 μm or three times the size of the other semi-axis. One does not observe any focal point for the vertical semi-axis, but this is not necessarily due to astigmatism, but can also be caused by the linear slit scan where the sum of both beams are being scanned.

In Fig. 4.30 the different scans at different position in the propagation direction for both the upper and lower HOE used as receiver. The scans show that the light received by the upper and lower HOE is coincident in the detector plane. This means that light from both HOEs are coupled in to the two receiver fibres.

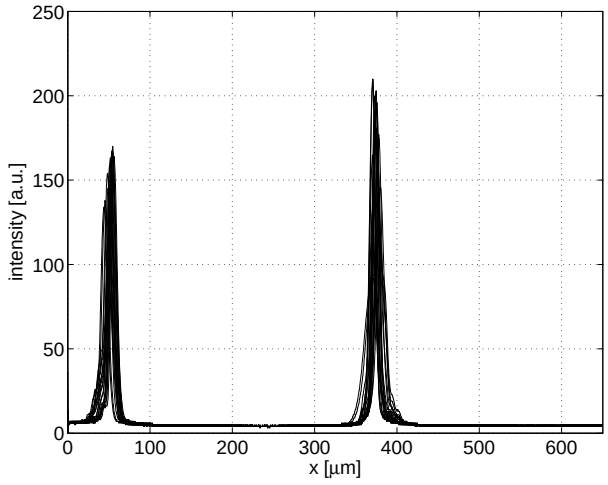

Figure 4.30: The scans made at different positions in the propagation direction show that the light received by the two receiver HOEs are coinciding at the detection plane.

The measurements of the detector plane also indicate some problems. These relate to the fact that the core of the fibres that are used to collect the light have a diameter of 50 μm. This is quite large compared to the 1/e^2 intensity radius of approximately 7.5 μm for the focused light beams. This of course makes it easier to couple the light in to the fibres, but it also means that the natural apertures from the fibre ends in themselves do not restrict the extent of the measurement volume. This is a problem that will have to be dealt with in the future. On the other hand, it is clear that cross-talk is removed from the system.

Calibration Measurements

The following calibration measurements were performed using a Sony grammophone player. A single gold thread having a 25 μm diameter was mounted vertically on the edge of the grammophone player 15 cm from the centre. The sensor was mounted so that the gold thread passed through the measurement volume, thereby making sure that only contributions from a confined area of the measurement volume were obtained. The rotational speed of the grammophone player

was monitored with a light emitting diode shining through a hole in the grammophone player. A photo diode on the other side measures the signal, and a temporal analysis of the measured signal showed that the rotational speed had a standard deviation of 0.008% compared to the average speed. The measurements were performed by translating the LTV sensor in the direction of light propagation. For each position, a number of velocity measurements were performed. The results from the measurements are shown in Fig. 4.31.

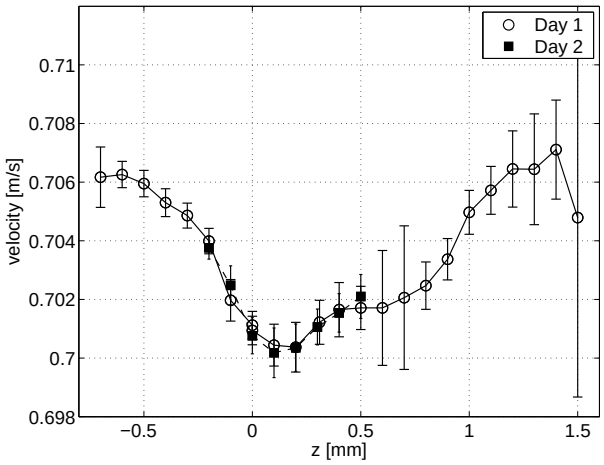

Figure 4.31: The measurements performed with a gold thread mounted on a grammophone player. The plot shows the measured velocity as a function of the longitudinal position in the measurement volume.

A number of things can be seen from the measurements. First of all, it is seen that the system is quite stable. The relative standard deviation for the majority of the different measurement positions is less than 0.1%. Furthermore, it is seen the reproducibility is quite good, since the measurements performed one day apart coincide. This shows that the position of the measurement volume is stable.

The measurements also indicate a problem with the system, since velocity measurements can be obtained within 2.4 mm of the measurement volume in the longitudinal direction. This is a problem, since we want to achieve a well-confined measurement volume. However, the relative standard deviation of the average measured velocity within the 2.4 mm is 0.32% and is well within the design parameters. Furthermore, the measurements do not give conclusive information about the extent of the measurement volume, since the measurements obtained far from the centre of the measurement volume need longer correlation times to obtain the velocity measurements due to the lower intensity of the beams at these positions, i.e. these measurements get a lower weighting than those from the centre of the measurement volume.

It can also be seen that the measurements from the centre of the measurement volume give a lower velocity than the measurements from the outer part of the volume. This result is consistent with the measured profile of the measurement volume, where the beam spacing is largest in the centre of the measurement volume (see Fig. 4.28).

Flow Measurements

The flow measurements are performed using a flow chamber. The test section has a quadratic flow channel with an inner edge length of 10 mm and a total length of 35 mm. Optical access is provided through two plane glass windows on each side of the flow chamber. Since the LTV system works in a backscattering setup, one of the windows has been made non-reflective so that particles passing the light reflected from the rear window do not contribute to the measurements. The window is 3 mm thick and the area of the window is so large that it does not restrict the receiver of the LTV system. The test section is connected to an upper and a lower water reservoir, which are held at constant water levels. These are connected using silicon hoses with a diameter of 10 mm. The inlet to the test section is straightened so that the ratio between the length of the inlet and the diameter of the hose is greater than 50, which is sufficient for the flow to nearly settle after upstream pipe bends. The water flow is constantly monitored by an ultrasonic flow meter giving an estimate of the mean flow velocity.

The system allows for stable flows in the range 1-240 l/h, which is controlled by adjustment of a valve. The flow uses demineralised water seeded with opto-PIV particles having an average diameter of 30 μm. The velocity is found from the cross-correlation string by making a Gaussian fit to the correlation in the velocity space. The turbulence intensity is found at the same time by evaluating the width of the Gaussian function, having taken the size of the seeding particles and width of the probing beams into account. The LTV sensor is mounted on the flow chamber, and the axial position of the measurement can be changed using a rail system. A digital ruler monitors the position of the sensor on the rail. The volume flow rate is monitored by an ultrasound flow meter.

Measurements in Centre of Flow Chamber

The following describes measurements performed in the centre of the flow chamber. The centre of the chamber is found by making a profile of the cross section, thereby locating the symmetry axis. The measured velocity in the centre of the chamber as a function of the mean velocity is depicted in Fig. 4.32 together with the corresponding turbulence intensities measured. The experiment has been carried out varying the volume flow from 3 to 240 l/h.

The max/avg-ratio as well as the turbulence intensity are seen to depend on the volume flow, and the flow is seen to be divided into three flow regimes. The laminar flow regime is found approximately where the average velocity ranges from 0 to 0.1 m/s. As the average velocity approaches 0, the flow should ideally follow a Poiseuille flow and the max/avg-ratio becomes approximately 2.25. For comparison the ratio would approach a factor 2 if the cross section of the flow chamber had been circular. The degree of turbulence is seen to be approximately constant at 3% in the laminar regime.

The transitional regime lies approximately in the region where the average velocity is between 0.1 and 0.3 m/s. In this regime, the flow profile is unstable and may switch between laminar and turbulent states. The velocity profile changes from a near parabolic shape to a near logarithmic shape, which has a more flat profile with sharp edges [92]. During the transition the measured max/avg-ratio drops from approximately 1.7 to 1.3.

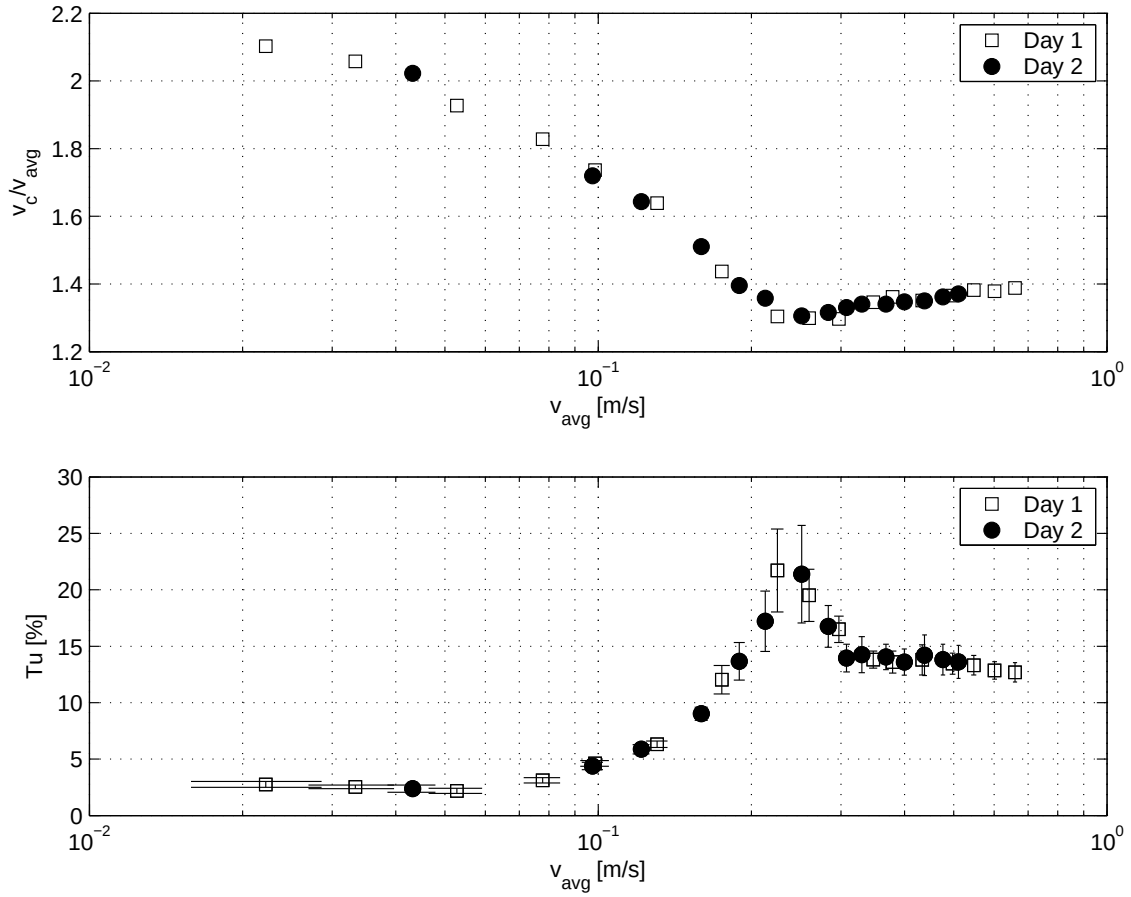

Figure 4.32: The measured velocity and turbulence intensity in the centre of a quadratic flow chamber as a function of the volume flow.

The turbulent regime is found in the region where the average velocity is greater than 0.3 m/s. In this regime the turbulence intensity stabilises and is nearly constant at 14% [93]. As the volume flow increases, the flow should theoretically approach a more logarithmic-like shape and the max/avg-ratio should accordingly approach a factor 1. However, the measurements in the turbulent region show that the ratio slightly increases instead. This indicates that conditions with either the LTV sensor or the flow system make the experiments differ from theory. More likely, it is a combination of the both. A condition of the optical system that influences the measurements is that the measurement volume is larger than intended, due to the large apertures of the fibre ends, as also indicated by the calibration measurements. Furthermore, the optical system is designed for flow pipes with a much larger diameter, which means that it is not really suitable for measurements in this flow chamber. Once again, the size of the measurement volume is the limiting factor. Conditions in the flow characteristics are also expected to influence the measurements. For instance, the fitting of the circular hose to the quadratic flow chamber can introduce unintended vortices. Furthermore, the friction conditions are not necessarily identical at both walls, since one

of the windows has been made non-reflective. This can introduce asymmetries in the flow at certain volume flow rates so that the ratio between the velocity in the centre of the chamber and the average velocity changes.

However, the measurements show some promising results in the sense that the results are reproducible. This is seen from the coinciding measurements that are taken one day apart. This means that the measurements performed with the LTV sensor can in fact be used as a calibration curve for the given flow system.

Profile Measurements

It was chosen to make a profile measurement of the volume flow from the laminar regime and one from the turbulent regime. The measured profile of the laminar regime is measured at a volume flow rate of 21 l/h corresponding to a mean velocity of 0.058 m/s and is shown in Fig. 4.33.

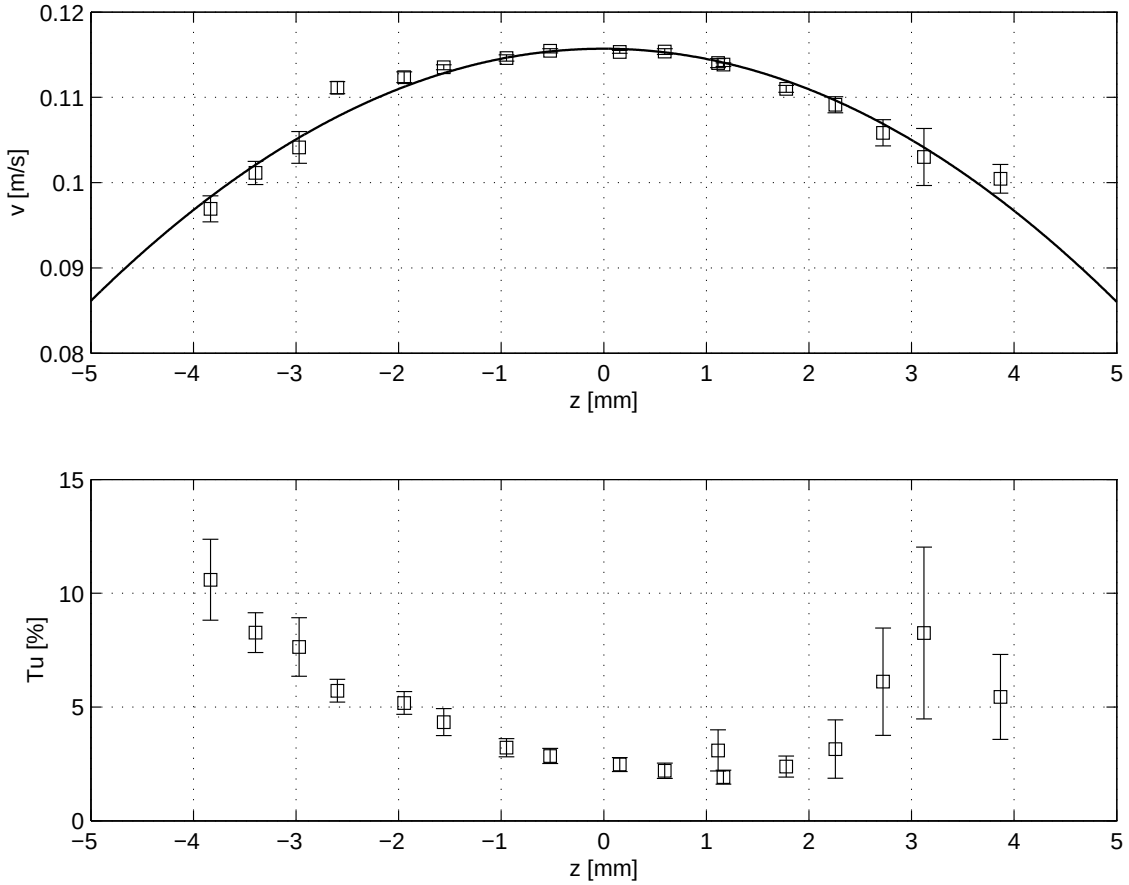

Figure 4.33: Measurement of the velocity profile and the corresponding turbulence intensities across the quadratic flow chamber performed at a volume flow of 21 l/h.

It is seen that a parabolic curve fits well with the measurements. However, it is seen that the profile is very flat and that the measured velocities are much greater than the average velocity (calculated

from the ultrasound measurement) over the entire cross section. The measured velocity, however, is in agreement with the previous measured max/avg-ratio of approx. 1.7 (see Fig. 4.32). The profile measurement additionally substantiates the fact that the size of the measurement volume is not suitable for a flow chamber of this size. The velocity measurements are the result of numerous particles passing through different positions of the measurement volume. Due to the parabolic shape of the flow profile, the measured velocity at a given axial position of the measurement volume is therefore a combination of particles having a fairly large range of velocities. Since there are more of the faster particles passing through the measurement volume in a given time period than the slower particles, the velocity measurement tends to be biased towards the higher velocities. Additionally, the turbulence intensity is lower in the centre of the flow chamber and thereby a larger share of the particles passing through the centre of the measurement volume contribute to the measurement.

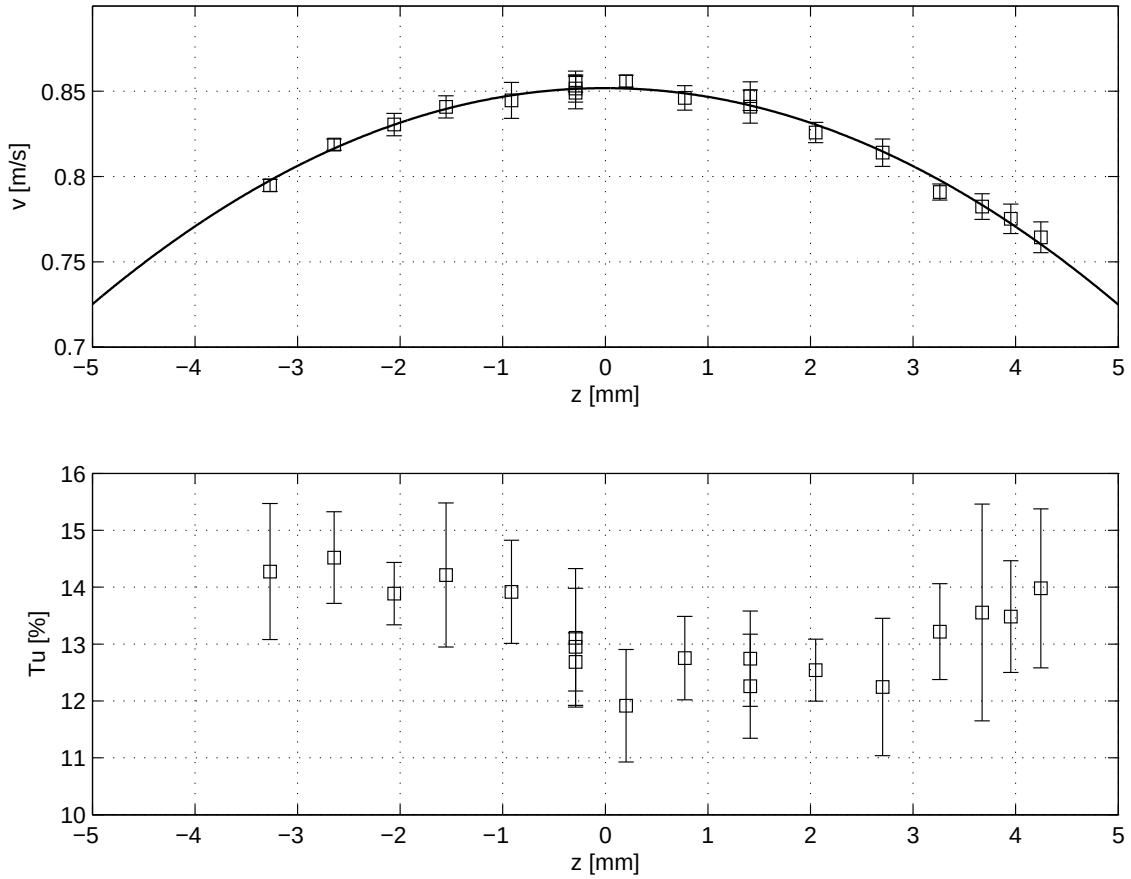

Figure 4.34: Measurement of the velocity profile and the corresponding turbulence intensities across the quadratic flow chamber performed at a volume flow of 222 l/h.

The same conditions as described above are observed in the profile measurement performed in the turbulent regime (see Fig. 4.34). These measurements are performed at a volume flow rate of 222 l/h corresponding to a mean velocity of 0.62 m/s. Once again, the measured profile is seen to

be flat and the velocities measured are approximately 1.3 times greater than the average velocity (calculated from the ultrasound measurement).

It is again seen that a parabolic function fits well with the measured profile. This again shows that the spatial resolution of the system is not high enough for showing the boundary flows and therefore the sharp edge of the logarithmic profile is difficult to detect. However, it is seen that the flow sensor is sensitive to the axial position of the sensor, and that relatively small axial changes of the sensor position are detectable. This indicates that the flow profile probably does not have so sharp edges. It would therefore have been better to measure a flow profile further into the turbulent region. However, this is not possible with the flow system provided.

The turbulence intensities measured in the two profiles show that variations are found across the profile and that the flow sensor is sensitive to these changes. This is especially apparent from the measurements in the laminar region, where the changes in turbulence intensity are significant, varying from 2.5% in the centre of the flow chamber to above 10% near the walls. It should be noted, however, that the depicted turbulence intensities are not the true turbulence. Due to the long measurement volume, there will be an apparent turbulence, which is caused by particles having different velocities throughout the measurement volume. This is especially in force in proximity to the boundary flows where the variations are greater than in the centre of the profile. Therefore, the apparent turbulence is also larger near the walls of the flow chamber.

4.2.7 Application of LTV sensor and Outlook

Once the LTV sensor has been optimised so that uncertainties from the velocity measurement in a small volume element have been minimised, it is still left to decide what method is to be used to determine the volume flow. Although the accuracy of the measurement system is high, it is notable that other sources can influence the accuracy of the volume flow measurement significantly. The uncertainties are for instance:

- Determining the area of the cross section for the flow pipe
- The position of the measurement volume
- The choice of method for determining the flow rate
- Velocity gradients in the measurement volume
- Flow measurements in flows that are temporally unstable
- Asymmetries in the velocity profile

Asymmetries in the flow are the main contribution to uncertainties [19]. It is therefore important to determine whether the system is to be able to measure asymmetrical flows or if it can be assumed that the flow profile is symmetric. In order to achieve this, the inlet has to be straightened so that the length of the inlet is 50 times greater than the diameter of the pipe.

There are several methods that can be used to determine the volume flow based on the measurements of velocities in a number of points along one or more radii in the flow pipe.

Volume Flow Measurements

The single point methods demand volume flow calibration, similar to the one depicted in Fig. 4.32. The method can either be based on measurement performed in the centre of the flow pipe or at a suitable distance from the centre. This point could for instance be chosen to be the point where the local velocity is expected to equal the average flow velocity. This point is called the Aichelen point, which is located 0.76 times the radius of the pipe from the centre [19]. The errors will be substantial if using this method on asymmetrical flows.

The multi-point methods utilise simultaneous measurements of the local velocity at strategically chosen points. The number and positions of these discrete points are chosen so that both the number of points and the measurement uncertainties are minimised. For instance, four measurements at the Aichelen distance could be used together with a measurement in the centre of the pipe [19].

The velocity-area methods are characterised by dividing the cross-section into a number of rings having the same area. In each ring, one or more measurement points are determined so that the average velocity in the ring can be measured directly. The positions of the measurement points are determined by the theoretical model used. By calculating the mean of the measurements from all the rings, the average velocity for the entire cross-section of the pipe can be calculated. Uncertainties of approximately 0.5-1% are obtainable using this method [18].

In the numerical methods, the local velocity is measured at at several positions in the cross section. Based on these measurements, an analytical integration of the velocity profile is calculated, for instance using spline-functions. The numerical methods do not need a theoretical model to describe the flow, and assumptions about the volume flow are not necessary.

The numerical and velocity-area methods use a number of measurement points along one or more radii. For symmetrical flows, it is sufficient to measure along one radius. For asymmetrical flows, however, the number of radii is generally more important than the number of measurement points along the radii.

In-Situ Calibration Sensor

We suggest a calibration or reference measurement system based on the LTV sensor developed. The volume flow is to be calculated using profile measurements along one or more radii. A computer-based system suggests the positions for local velocity measurements based on the velocity-area and/or numerical methods and the desired measurement uncertainties.

The measurement installation has to be constructed so that optical access can be achieved along a sufficient number of radii. The LTV sensor is movable, thereby allowing the measurement volume to be moved along these radii. Provided that the working distance of the LTV sensor allows for measurements over the entire diameter of the flow pipe, we suggest the installation of three access windows so that there are 60 degrees between each radius. If the measurement volume can only be moved a distance corresponding to the radius of the pipe, six access windows are suggested.

Since the LTV sensor only makes it possible to obtain local velocity measurements from one

point at a time, an auxiliary measurement of the volume flow rate is needed in order to be able to accommodate for temporal changes in the volume flow. The auxiliary measurement can be carried out using the flow sensor that is to be re-calibrated or re-verified.

4.2.8 Summary and Discussion

A novel laser time-of-flight sensor has been developed. The central part of the system is a multi-functional holographic optical element (HOE) that maintains the majority of the optical functions of the system. The HOE layer contains both the transmitter and receiver functions of the system. This makes the system self-aligning and the stability of the system is thus inherent in the HOE. The HOE layer is additionally designed so the total angles of deflection for the transmitter and receiver HOE are identical, which ensures that the system to a first degree is wavelength independent.

A theoretical description of the wavelength dependency of the system shows that the beam spacing of the two probe beams changes approximately 0.026% for a 0.3 nm shift in wavelength, which corresponds roughly to a mode hop for the laser diode used. The theoretical description also shows the changes in the ambient temperature does not have a large influence on the characteristics of the measurement volume. The interfocal distance of the two probe beams thus changes only 0.045% for a 25 degrees centigrade change in ambient temperature, even if the HOE is implemented in polycarbonate, which has a large linear thermal expansion coefficient compared to for example BK7 and fused silica.

The calibration measurements carried out by moving a thin gold thread through the measurement volume show that the relative standard deviation of velocity measurements from a well-confined point in the volume is less than 0.1%. Furthermore, the measurements showed that the total relative standard deviation is only 0.32% over a 2.4 mm longitudinal range of the measurement volume. However, the measurements also show that the longitudinal length of the measurement volume is too large, since we want to achieve a well-confined measurement volume. This can for instance be achieved by putting smaller apertures in the detection system. The apertures are presently 50 μm in diameter and made up by two multimode fibre ends. However, it should be noted that the measurement volume is probably somewhat smaller than 2.4 mm, since the reflected light from particles in the centre of the measurement volume will have a higher intensity and thereby more signals meet the binary clipping level, which is set from the digital signal processing.

The measurements of the flow in a quadratic flow chamber with an inner length of 10 mm show that the LTV system can be used to obtain measurements from a flow. The measurements performed in the centre of the chamber show that the sensor can in fact be used as a calibration tool, since the measurement relative standard deviation of the measurements are about 0.5-1% and that the results are reproducible. The measurements of the velocity profile across the flow chamber show that the LTV system is sensitive to small axial changes to the measurement volume of the system. However, the measurements show that the measurement volume is too large for accurate measurement of the profile in a flow installation of this size. This is seen clearly, since the measured velocities are greater than the average flow velocity in the chamber.

It would therefore be advantageous to test the LTV sensor on the installation that it is intended

for, i.e. flow pipes with a large diameter (up to DN200). Furthermore, it would be profitable to construct a system based on replicas of the presented system and demonstrate that the same system properties are achievable. This, however, has not been completed within the time-scope of the PhD project.

4.3 Multiple Time-of-Flight

This section deals with a constructed multiple laser time-of-flight system (MLTV). The MLTV system is probably the one of the flow systems presented in this thesis that is easiest to miniaturise and show excellent promise as a sturdy and compact sensor. However, the system is not so flexible as the other systems presented, since it is based on a VCSEL array that has a fixed spacing between the individual VCSELs. This means that the measurement volume can only be configured with a certain ratio between beam spacing and waist. This also means that it is not so applicable for flow measurements in pipes with a large diameter. For this reason, this is not the flow measurement system that is pursued in this project, but the characterisation of the measurement volume is included in order to provide some comparisons with the LDA and LTV systems. For more details on the system or flow measurements performed with the system, see Ref. [77].

4.3.1 Principle of Method

The multiple time-of-flight sensor consists of two parts, viz. a transmitter that illuminates the measurement volume and a receiver part that probes the event in the measurement volume. The light source is a VCSEL array and the near field of these VCSELs are imaged either as spots or sheets with a specific beam distance, Λ_m. This distance is determined partly by the magnification, M, of the imaging system and by the pitch distance, Λ_s, of the VCSEL array, i.e. the distance between the individual VCSELs.

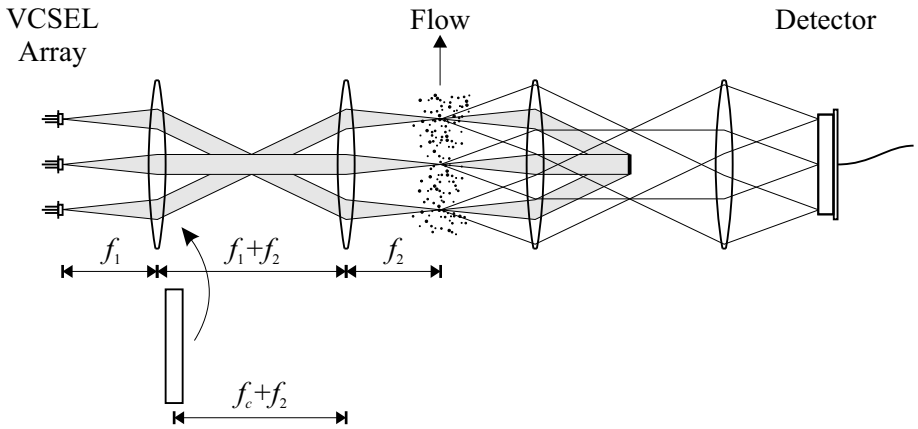

Figure 4.35: The transmitter (left) and the receiver (right) are each based on a clean imaging system. For generating sheets instead of spots in the measurement volume, a cylindrical lens, f_c, is inserted.

The transmitter system is implemented as a clean imaging system, which replicates the near field of the VCSEL array in the measurement volume, while maintaining the original propagation direction

of the beams as illustrated in Fig. 4.35. The beam distance will then be given by:

$$\Lambda_m = |M|\Lambda_s = \frac{f_2}{f_1}\Lambda_s \,, \tag{4.38}$$

where f_1 is the focal length of the lens facing the VCSEL array, f_2 is the focal length of the lens facing the measurement volume, and Λ_s is the pitch length of the VCSEL array. The pitch length for commercial VCSEL arrays for the telecommunication industry is 250 μm.

In order to generate light sheets in the measurement volume, a cylindrical lens with focal length, f_c, can be inserted with the symmetry axis parallel to the VCSEL array. The ratio between the beam spacing and the width of the beams/sheets is independent of f_2, while f_1 and f_c can be used to model this ratio, which can easily be varied from 1:1 to 1:100.

The receiver part is imaged onto a detector that is large enough for collecting the entire image. The receiver part consists of a clean imaging system with a spatial high pass filter positioned in the Fourier plane of the object, thereby blocking the directly transmitted light. The velocity component, v, is found from the beam spacing, Λ_m, and the peak separation, τ, obtained from the autocorrelation of the temporal detector signal,

$$v = \frac{\Lambda_m}{\tau} \,. \tag{4.39}$$

4.3.2 Experimental Setup

The VCSEL array is a single mode 1×10 array from Avalon Photonics and has 10 VCSELs on a straight line with a common cathode and individually addressable anodes. The VCSELs operates at single mode with an optical output of approximately 0.5 W. The operating wavelength is 850 ± 2 nm, and the full width at half maximum beam divergence is approximately 12° when operating at 4 mA.

Both the clean imaging system of the transmitter and receiver are implemented by the use of two 40 mm achromatic lenses. The optional cylindrical lens is mounted between the two transmitter lenses and up against the lens, f_1. The measurement thereby has a beam spacing of 0.25 mm, since $M = 1$, and the total width of the measurement volume is 2.3 mm.

In an ideal system, the beams have a waist of 1.6 μm. If the system is used in the spot configuration, the height of the measurement volume is twice the size of the waist size, while the height is approximately 14 mm in the sheet setup. The full longitudinal length of the measuring volume for the spot and sheet setup is 45 μm and 130 μm, respectively.

4.3.3 Measurements of the Measurement Volume

Figure 4.36 shows the intensity distribution obtained by making a beam scan in the image plane of the transmitter system using a Photon Inc. beam scanner.

This scan is performed on the system operating in the sheet configuration. By applying a Gaussian curve fit to the individual beams, the individual beam widths and spacing between adjacent beams

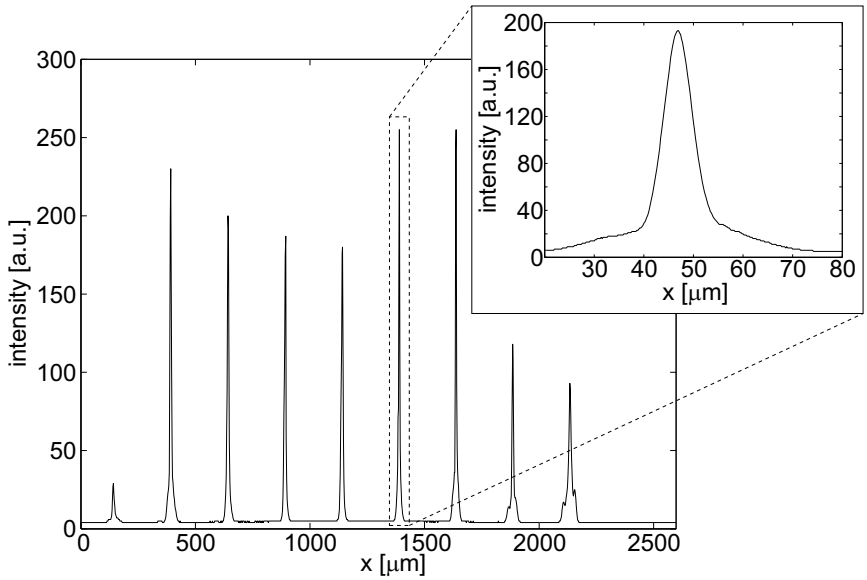

Figure 4.36: The measured intensity distribution across a measurement volume with sheets using a beam scan with 2 μm resolution. The inset shows a close-up of one the sheets, scanned at 0.2 μm resolution.

are calculated. Stepping the beam scanner through the measurement volume and finding the axial position with the lowest mean beam radius identifies the image plane. At this image plane, the mean sheet spacing is measured as 249.8 μm with a standard deviation of 0.36 μm (0.14%). At the estimated position of the image plane, the mean beam radius is measured as 7.1 μm with a standard deviation of 2.1 μm and the height of the measurement volume is measured as 10 mm.

Moving the scanner through the measurement volume (within a range of $\pm$ 0.4 mm along the optical axis), the systematic deviation in the mean spacing in estimated by linear regression as 0.4 μm/mm. Further, the maximum standard deviation at a given axial position is estimated as 1.1 μm (0.44%). The deviations are systematic and accordingly, the axial positions of the waist points appear to fit a typical curvature of field in the image plane as depicted in Fig. 4.37.

The most extreme axial position of the waist points is displaced by several Rayleigh lengths estimated to be 18.5 μm by measuring the average a mean beam divergence of 7.4°. This is one of the main reasons for the high value of the mean beam radius. However, the minimum beam waist in the image plane is measured as 4.3 μm. This is approximately a factor of two greater than expected, which is also indicated by the divergence angle. Thus, optical aberrations as well as limitations in the scanning resolution are expected to affect the individual waist measurements. The longitudinal length of the measurement volume is measured roughly to be 0.3 mm (see also Fig. 4.37). Flow measurements have been performed in the same quadratic flow chamber as described in Sec. 4.2. These measurements have been performed in a forward scattering setup in both the spot and sheet configuration. The results can be seen in Ref. [77].

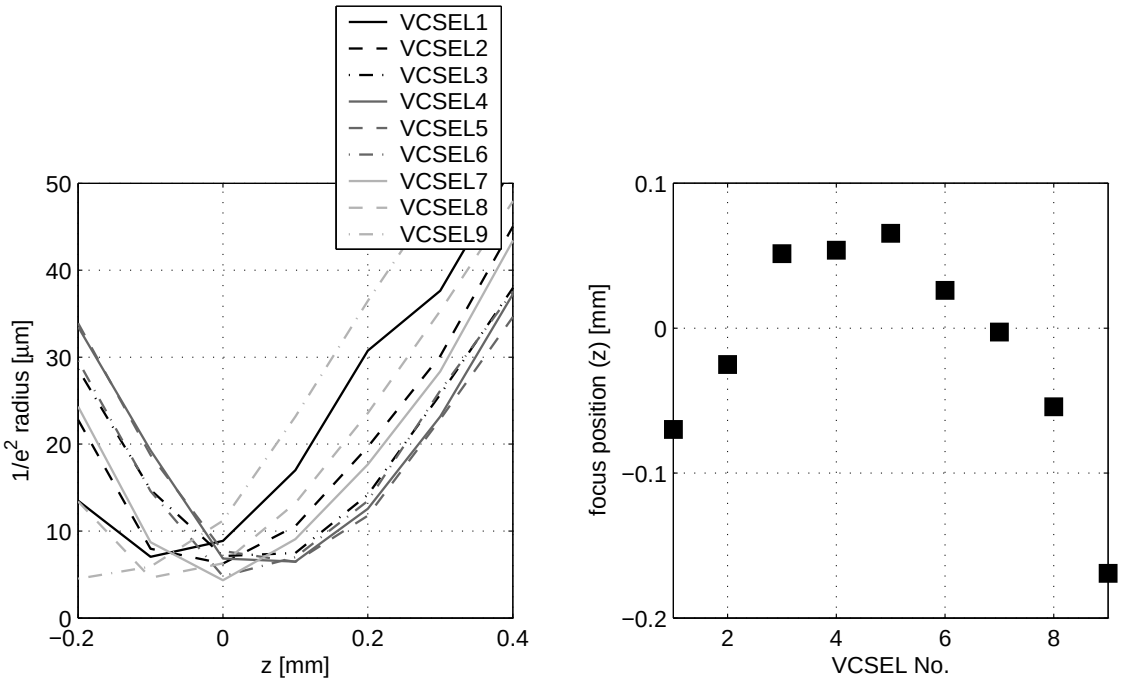

Figure 4.37: The beam radius for the different VCSELs as a function of the axial positions of the measurement volume (left) and the estimated waist point of the different positions found from curve fitting (right).

4.3.4 Discussion and Summary

A simple and inexpensive laser anemometer for low or medium power applications has been presented. The technology of the VCSEL arrays has enabled a simple optical imaging system as the key to implement a robust and temperature-stable multiple laser time-of-flight sensor. The sheet spacing is determined only by the magnification of the imaging system and the pitch length of the array. Therefore, the spacing will only vary with the thermal expansion coefficient for the substrate of the array. Furthermore, the only wavelength dependence on the beam spacing is that which enters through the wavelength dependence on the optical magnification of the imaging system.

The system provides parallel light beams with a maximum variation in spacing of 0.44% throughout the measurement volume. However, the system displays a rather large field of curvature and spherical aberrations making the variations of the axial focal point for the different VCSELs vary several Rayleigh lengths. These variations can be reduced by, for instance, using field flattening optical components. This, however, will make the system more expensive. The asset of the sensor is for short working distances with beam spacing not too far from the intrinsic pitch length of the VCSEL array. This makes the system especially applicable to measuring boundary flows. In return, the system is not applicable when a large working distance is needed, since this will make the measurement volume very large.

The method, compared to conventional LTV systems, has the advantage that several time-of-

flight measurements contribute to the total velocity measurements. This means that successful velocity measurements can be obtained from signals with a lower signal-to-noise ratio than for a two-beam LTV system. One can introduce new beams in the measurement volume without trading off the power of the individual beams, simply by choosing an array with more VCSELs. This however, makes the measurement volume wider, which might not be expedient. Furthermore, the method, compared to conventional LDA system, has the advantage that direction of the flow can be determined by introducing asymmetry in the measurement volume, which is easily obtained by switching off one of the VCSELs.

It should be noted that a multiple time-of-flight system could also be achieved by using one laser diode and a specially designed HOE. This would also be a simple method for eliminating the problems with spherical aberrations. Additionally, it leaves one with more design possibilities, since the beam spacing, number of beams and working distance can be designed independently. The trade-off is of course that the individual beams in the measurement volume will have less power. Furthermore, it can be difficult to design the HOE so that the individual beams display Gaussian behaviour.

4.4 Discussion and Conclusions

Three novel flow sensors have been presented.

A new beam splitter system for wavelength compensation of the fringe spacing in the measurement volume for laser Doppler anemometry systems has been developed. It has been both theoretically and experimentally verified that the use of the beam splitter can improve the wavelength sensitivity of the LDA system significantly, compared to a conventional LDA setup. This indicates that non-stabilised laser diodes can be used in combination with the new beam splitter system, which can reduce both size and production costs of commercial LDA probes. These are traditionally based on gas lasers and delicate optics making the systems bulky and expensive. The new LDA system, however, has not been demonstrated in a flow installation. This is therefore a subject for further studies of the system.

A novel laser time-of-flight system has been developed. The sensor is intended for in-situ calibration of other flow sensors permanently installed in the field. The central part of the LTV sensor is a multi-functional holographic optical element that works as both transmitter and receiver in the system. This makes the system inherently stable and the HOEs are additionally designed so that the system to a first degree is insensitive to wavelength changes. This, in combination with the use of a laser diode as the light source, provides a sensor that is robust and compact. It has been demonstrated that the LTV sensor can be used to measure a flow profile in a quadratic flow chamber with an inner length of 10 mm. However, the measurement volume of the LTV system is too large to give detailed information about the flow profile. This is due to the fact that the LTV sensor has been designed for measurements in larger flow installations (pipes up to DN200). Should the LTV sensor instead be used for flow measurements in small installations like the quadratic flow chamber, the sensor should have been designed with a shorter focal length, which would reduce the extent of the measurement volume. The LTV sensor is close to a working prototype, but measurements on large flow installations are needed before final estimation of the applicability of the

sensor can be given.

Finally, the characterisation of the measurement volume of a multiple laser time-of-flight system based on a VCSEL-array has been given. The sensor provides a simple and robust system and has the potential of being very compact, and is additionally distinguished by being temperature and wavelength independent. The system, however, shows a rather large curvature of field and spherical aberrations, which make the axial positions of the focal points for the different VCSELs vary several Rayleigh lengths. This can be corrected by the proper choice of optics, but will make the system more expensive.

The LDA sensor has the advantage compared to the other systems that several fringes are present in the measurement volume. These fringes presently have a spacing of approximately 7 μm, and the system can measure one velocity component no matter the degree of turbulence. The LDA sensor is also advantageous to the LTV sensor in the sense that a successful velocity measurement can be performed from signals with a lower signal-to-noise ratio, which is due to the fact that several fringes in the measurement volume contribute to the measurement. The LTV sensor on the other hand has the advantage that the spot intensities are of a magnitude greater than the fringe intensities of the LDA system, which is due to the fact that all the power of the transmission system is present in two beams. Furthermore, the beam spacing of the LTV system is to a first degree independent of temperature changes. This is not necessarily true for the LDA sensor, where temperature changes might influence the collimation of the light source. This would introduce gradients for the fringes in the measurement volume and thereby influence the accuracy of the system.

The multiple laser time-of-flight system and the LTV system are comparable in accuracy. The relative standard deviations for the beam spacing over the entire measurement volume are thus as low as 0.44% and 0.32%, respectively, for the two systems. The multiple laser time-of-flight system has the advantage compared to the LTV sensor that particles passing through the measurement volume will contribute to several time-of-flight measurements. Therefore, a successful velocity measurement can be obtained from a signal with a lower signal-to-noise ratio. Moreover, the system can add more beams to the measurement volume simply by adding more VCSELs to the array. This means that more time-of-flight measurements can be obtained without trading off power in the individual beams. However, the width of the measurement increases with each beam. The problem with the system, however, is that it in not very flexible. Commercially available VCSEL arrays are only found with a pitch of 250 μm, which means that the system cannot be designed with a desired ratio between beam diameter and beam spacing. This makes the system virtually useless for measurements in large flow installation, since the large working distance would make the measurement volume very large. The VCSEL array system thus works best in configurations where the beam spacing in the measurement volume is not too far from the intrinsic pitch length of the array.

It should be noted that a multiple time-of-flight sensor could also be achieved by using one laser diode and a specially designed HOE by adding more lens elements to the transmitter part of LTV sensor. This would leave the possibility to design the system so that the beam diameter and spacing can be chosen independently. This could also eliminate the problems with the curvature of field in the measurement volume. The trade-off, however, would be less power in the individual probe beams.

5

Conclusion

I have not failed 700 times. I have not failed once. I have succeeded in proving that those 700 ways will not work. When I have eliminated the ways that will not work, I will find the way that will work.

Thomas A. Edison (1847-1931)

This thesis deals with the development of optical sensors based on laser diodes and dedicated diffractive optical elements. The work has been divided into two parts, namely the development of interferometrically based displacement sensors and the development of optical flow sensor systems. All the diffractive structures are implemented as surface relief structures in photoresist. These structures have the advantage that they can be replicated using for instance injection moulding. Thereby one can mass-produce the structures at low cost, which makes it possible to manufacture a cheap optical sensor.

The object of the first part of the project was to explore to what degree the implementation of optical sensor techniques in pressure transducers could improve the measurement precision and dynamic range. For the purpose of probing the deflection of the diaphragm in a pressure transducer, a novel common-path interferometer has been developed. The central part of the common-path interferometer is a multi-functional holographic optical element (HOE) that handles function like beam splitting and focusing of the light. The HOE works as both transmitter and receiver in the common-path setup. This means that the stability is inherent in the HOE and the system is self-aligning, which makes the sensor very robust. During the development of the interferometer, a technique to extend the unambiguous measurement range of differential displacements was devised. This technique is based on probing three points on the object surface simultaneously and utilises the quadrature phase signals that automatically are provided by the specially designed HOE. The system has been demonstrated to having a sensitivity of 0.3 nm for differential displacements and it has been demonstrated that a dynamic range of 1:14,000 is obtainable for an angular displacement sensor. The automatically provided quadrature phase signals make the system especially suited for dynamic measurements such as vibrometry, and a proposal for the future design

of a vibrometer has been given. This design is based on stacking of HOE layers, which ideally provides a robust sensor as well as easy alignment and assembly of the sensor. Based on the same principles, a proposal for the future design of a pressure sensor has been given. However, the measurement principle has not yet been demonstrated in the probing of a diaphragm and the system is still to be optimised, especially if the system is to be used for probing the displacement of rough surfaces.

During the project, there has also been developed a new tool for conceiving new types of common-path interferometers by placing a specially designed HOE in the Fourier plane of a 4-f setup. The surface structure for the Fourier filter can be calculated by Fourier transforming the desired impulse response function of the system. Thereby, the system can be designed to probe a specific type of surface displacement. Based on this principle, a novel type of curvature interferometer has been proposed. This interferometer can probe the deflection of a circular diaphragm by letting light reflected from the annular part of the diaphragm interfere in the detector plane with light collected from the centre part of the diaphragm. The system, however, has only been described theoretically and has yet to be experimentally verified.

The second part of the project deals with development of optical flow sensors based on laser diodes and dedicated diffractive optics. In this work, two systems have been devised, which both have been described theoretically and experimentally verified. Firstly, a new beam splitter system based on two linear gratings has been devised. The beam splitter is intended for use in LDA systems, where the fringe spacing in the measurement volume is directly proportional to the wavelength of the light source. This is compensated by the beam splitter by letting the beam spacing between the two parallel beams from the beam splitter system be approximately proportional to the wavelength. It has been demonstrated both theoretically and experimentally that the wavelength sensitivity of LDA systems can be reduced significantly using the beam splitter system. The system, however, has not yet been demonstrated in a flow setup. It should be noted that the beam splitter is not necessarily restricted to the use of LDA systems, but can also be used in other systems where a wavelength dependent spacing between two parallel beams is needed. This could for instance be used to make a wavelength independent tilt sensor.

Secondly, a new laser time-of-flight sensor has been developed. The sensor is intended for in-situ calibration of other types of flow sensors, which are permanently installed in large flow installations. The system is designed so that the transmitter and receiver functions are implemented in a single HOE plane. This makes the LTV sensor self-aligning and robust. The multi-functional HOE is additionally designed so that the LTV sensor to a first degree is wavelength independent. It has been demonstrated experimentally how the LTV sensor can be used to measure a velocity profile for a given flow installation. A base plate for mounting the different optical components of the LTV sensor has been designed and the assembly of the system has been standardised, although still in need of optimisation. Additionally, digital signal processing has been developed for the sensor, and a PC front-end for the system has been created using LabView. The LTV sensor is thus close to a working prototype. Before this can be verified, the system, however, needs more thorough testing on the flow installations that it is intended for (flow pipes up to DN200). Since the HOE of the LTV sensor has many similarities to the HOE of the displacement sensor, a future design of the LTV sensor could be based on the same principles as suggested for the vibrometer and pressure sensor, i.e. stacking of HOE layers. This could provide a more compact design for

the LTV sensor, as well as simplify the design of the system, since the transmitter and receiver part of the sensor would be separated. Furthermore, the design could remove the need for the achromat in the detector unit.

In conclusion, it has been demonstrated how the use of dedicated diffractive optical elements in combination with laser diodes can make up various types of optical sensors. The sensors are sturdy and compact and have the potential of being mass-produced at low cost through replication of the diffractive structures. However, functional sensors based on replicas of the original surface relief structures are yet to be demonstrated, and this is one of the immediate subjects for further studies.

Bibliography

[1] K. Iga, M. Oikawa, S. Misawa, J. Banno, and Y. Kokubun, "Stacked planar optics: an application of the planar microlens," Applied Optics **21,** 3456–3460 (1982).

[2] P. M. Higgs, "A Recording Mechanical Pressure Gauge of High Range," The Review of Scientific Instruments **20,** 23–26 (1949).

[3] O. Tsukakoshi, K. Murakami, and C. Hayashi, "A New Diaphragm Manometer with a Semiconductor Strain Gauge as Pressure Sensing Element," Vacuum **14,** 425–427 (1964).

[4] Y. Kanda and A. Yasukawa, "Optimum design considerations for silicon piezoresistive pressure sensors," Sensors and Actuators A **62,** 539–542 (1997).

[5] W. Huang, Y. Zou, and C. Wang, "On the dynamic behaviours of a strain gauge pressure sensor," Rev. Sci. Instrum. **66,** 3676–3679 (1995).

[6] O. Akar, T. Akin, and K. Najafi, "A wireless batch sealed absolute capacitive pressure sensor," Sensors and Actuators A **95,** 29–38 (2001).

[7] H. Kim, Y.-G. Jeong, and K. Chun, "Improvement of the linearity of a capacitive pressure sensor using an interdigitated electrode structure," Sensors and Actuators A **62,** 586–590 (1997).

[8] W. H. Ko and Q. Wang, "Touch mode capacitive pressure sensor," Sensors and Actuators A **75,** 242–251 (1999).

[9] S. T. Moe, K. Schjølberg-Henriksen, D. T. Wang, E. Lund, J. Nysæther, L. Furuberg, M. Visser, T. Fallet, and R. W. Bernstein, "Capacitive differential pressure sensor for harsh enivronments," Sensors and Actuators A **83,** 30–33 (2000).

[10] M. M. Murphy and G. R. Jones, "Optical fibre pressure measurement," Meas. Sci. Technol. **4,** 258–262 (1993).

[11] A. Wang, M. S. Miller, A. J. Plante, M. F. Gunther, K. A. Murphy, and R. O. Claus, "Split-spectrum intensity based optical fiber sensors for measurements of microdisplacement, strain, and pressure," Applied Optics **35,** 2595–2601 (1996).

[12] W. N. MacPherson, M. J. Gander, J. S. Barton, J. D. C. Jones, C. L. Owen, A. J. Watson, and R. M. Allen, "Blast-pressure measurement with a high-bandwidth fibre optic pressure sensor," Meas. Sci. Technol. **11,** 95–102 (2000).

[13] J. Park and M.-G. Kim, "High-Performance Fiber-Optic Fabry-Perot Pressure Sensor with $Si_3N_4/SiO_2/Si_3N_4$ Diaphragm," Meas. Sci. Technol. **11,** 95–102 (2000).

[14] W. N. MacPherson, J. M. Kilpatrick, J. S. Barton, and J. D. C. Jones, "Miniature fiber optic pressure sensor for turbomachinery applications," Review of Scientific Instruments **70,** 1868–1874 (1999).

[15] M. C. Furstenau, "Flow Measurement," in *Encyclopdia of Science and Technology*, 6th ed. (McGraw-Hill Book Company, 1987), pp. 159–170.

[16] "Datasheet for ULTRAFLOW®,", http://www.kamstrup.com/, 2003.

[17] S. Frank and H. E. Siekmann, "Flow-rate Measurements in Asymmetric Waterflows by Means of Laser-Doppler-Velocimetry," In *International Conference of Flow Measurements*, (Beijing, China, 1996).

[18] V. D. Bublitz, S. Frank, and H. E. Siekmann, "Einsatz eines Laser-Doppler-Velozimeters als Volumenstrom-messgerät hoher Genauigkeit," Euroheat and Power **25,** 588–598 (1996).

[19] S. Frank, C. Heilmann, and H. E. Siekmann, "Point-velocity methods for flow-rate measurements in asymmetric pipe flow," Flow Meas. Instrum. **7,** 201–209 (1996).

[20] R. Dammel, "Diazonaphthoquinone-based Resists," in *Tutorial Texts in Optical Engineering* (SPIE, Washington, 1993), Vol. TT 11.

[21] C. Zanke, A. Gombert, A. Erdmann, and M. Weiss, "Fine-tuned profile simulation of holographically exposed photoresist gratings," Optics Communications **154,** 109–118 (1998).

[22] L. Mashev and S. Tonchev, "Formation of Holographic Diffraction Gratings in Photoresist," Applied Physics A **26,** 143–149 (1981).

[23] J. N. Latta, "Computer-based analysis of hologram imagery and abberations," Applied Optics **10,** 609–618 (1971).

[24] J. N. Latta, "Computer-Based Analysis of Hologram Imagery and Aberrations II: Aberrations Induced by a Wavelength Shift," Applied Optics **10,** 609–618 (1971).

[25] J. N. Latta, "Analysis of Multiple Hologram Optical Elements with Low Dispersion and Low Aberrations," Applied Optics **11,** 1686–1696 (1972).

[26] J. N. Latta and R. V. Pole, "Design techniques for forming 488-nm holographic lenses with reconstruction at 633 nm," Applied Optics **18,** 2418–2421 (1979).

[27] C. Yan, M. Nakao, T. Go, K. Matsumoto, and Y. Hatamura, "Injection molding for microstructures controlling mold-core extrusion and cavity heat-flux," Microsystem Technologies **9,** 188–191 (2003).

[28] F. Nikolajeff, S. Jacobsson, S. Hård, Å. Billman, L. Lundbladh, and C. Lindell, "Replication of continuous-relief diffractive optical elements by conventional compact disc injection-molding techniques," Applied Optics **36,** 4655–4659 (1997).

[29] D. Gabor, "A new microscope principle," Nature **161,** 777–778 (1948).

[30] H. Becker and U. Heim, "Hot embossing as a method for the fabrication of polymer high aspect ratio structures," Sensors and Actuators A **83,** 130–135 (2000).

[31] G. Giuliani, S. Donati, and M. Passerini, "Angle Measurement by injection detection in a laser diode," Optical Engineering **40,** 95–99 (2001).

[32] P. S. Huang, S. Kiyono, and O. Kamada, "Angle measurement based on the internal-reflection effect: a new method," Applied Optics **31,** 6047–6055 (1992).

[33] G. D. Chapman, "Interferometric Angular Measurement," Applied Optics **13,** 1646–1651 (1974).

[34] P. Shi and E. Stijns, "New optical method for measuring small-angle rotations," Applied Optics **27,** 4642–4344 (1988).

[35] S. G. Hanson, L. R. Lindvold, and B. H. Hansen, "Robust optical systems for nondestructive testing based on laser diodes and diffractive optical elements," Optics and Lasers in Engineering **30,** 179–189 (1998).

[36] X. Wang, X. Wang, H. Lu, F. Qian, and Y. Bu, "Laser diode interferometer for measuring displacements in large range with nanometer accuracy," Optics & Laser Technology **33,** 219–223 (2001).

[37] T. Suzuki, O. Sasaki, and T. Maruyama, "Absolute distance measurement using wavelength mutliplexed phase-locked laser diode interferometry," Optical Engineering **35,** 492–497 (1996).

[38] O. Y. Kwon, D. M. Shough, and R. A. Williams, "Stroboscopic phase-shifting interferometry," Optics Letters **12,** 855–857 (1987).

[39] M. Deininger, L. Wang, K. Gersner, and T. Tschudi, "Optical phase step method for absolute interferometry using computer-generated holograms," Applied Optics **34,** 5620–5623 (1995).

[40] N. B. E. Sawyer, C. W. See, M. Clarc, M. G. Somekh, and J. Y. Goh, "Ultrastable absolute-phase common-path optical profiler based on computer-generated holography," Applied Optics **37,** 6716–6720 (1998).

[41] C. Polhemus, "Two-Wavelength Interferometry," Applied Optics **12,** 2071–2074 (1973).

[42] O. Sasaki, H. Sasazaki, and T. Suzuki, "Two-wavelength sinusoidal phase/modulating laser-diode interferometer insensitive to external disturbances," Applied Optics **30,** 4040–4045 (1991).

[43] P. de Groot and S. Kishner, "Synthetic wavelength stabilization for two-color laser-diode interferometry," Applied Optics **30,** 4026–4033 (1991).

[44] D. C. Ghiglia and M. D. Pritt, *Two-Dimensional Phase Unwrapping: Theory, Algorithms, and Software* (John Wiley & Sons, Inc., 1998).

[45] J. E. Greivenkamp, "Sub-Nyquist Interferometry," Applied Optics **26,** 5245–5258 (1987).

[46] J. E. Greivenkamp, A. E. Lowman, and R. J. Palum, "Sub-Nyquist interferometry: implementation and meaurement capability," Opt. Eng. **35,** 2962–2969 (1996).

[47] S. R. Kitchen, C. Dam-Hansen, and S. G. Hanson, "Optical Displacement Sensor Based on Common-Path Interferometry for Industrial Purposes," In *Proceedings of the Northern Optics 2000 and EOSAM 2000 Conference*, K. Biedermann and U. Olin, eds., p. 134 (Uppsala, Sweden, 2000).

[48] C. Dam-Hansen, J. Stubager, L. Lindvold, and L. Lading, "Compact and low cost holographic optical front ends for an industrial laser time-of-flight flowsensor," In *Proceedings of the Third International Congress and Exhibition on Optoelectronics, Optical Sensors and Measuring Techniques*, pp. 7–10 (Erfurt, Germany, 1998).

[49] P. Hariahan, *Optical Holography* (Cambridge Univ. Press, 1996).

[50] S. R. Kitchen and C. Dam-Hansen, "Holographic common-path interferometer for angular displacement measurements with spatial phase stepping and extended measurement range," Applied Optics **42,** 51–59 (2003).

[51] M. D. Giovanni, *Flat and Corrugated Diaphragm Design Handbook* (Marcel Dekker, Inc., 1982), pp. 134–135.

[52] K. Creath, "Phase-measurement interferometry techniques," in *Progress in optics XXVI*, E. Wolf, ed., (Elsevier Science publishers B.V., 1988), pp. 351–391.

[53] P. L. Wizinowich, "Phase shifting interferometry in the presence of vibration: a new algorithm and system," Applied Optics **29,** 3271–3279 (1990).

[54] J. W. Goodman, "Statistical Properties of Laser Speckle Patterns," in *Topics in Applied Physics*, J. C. Dainty, ed., (Springer Verlag Berlin Heidelberg, 1975), Vol. 9, pp. 9–74.

[55] S. R. Kitchen, S. G. Hanson, and R. S. Hansen, "Fourier Plane Filters and Common-Path Interferometry in Vibrometers and Electronic Speckle Interferometers," In *Optical Engineering for Sensing and Nanotechnology (ICOSN 2001)*, K. Iwata, ed.,**4416,** 108–111 (Yokohama, Japan, 2001).

[56] S. R. Kitchen, S. G. Hanson, and R. S. Hansen, "Introduction of the Impulse Response Function in Common-Path Interferometers with Fourier Plane Filters," Optical Review **8,** 378–381 (2001).

[57] R. Jones and C. Wykes, *Holographic and Speckle Interferometry*, 2nd ed. (Cambridge University Press, Cambridge, 1989).

[58] S. G. Hanson and L. Lindvold, "High accuracy sensor for dynamic measurements based on holographic optical elements, semiconductor lasers and detectors," In *Conference on lasers and electro-optics Europe*, p. 68 (Amsterdam, 1994).

[59] H. Rabal, R. Henao, and R. Torroba, "Digital speckle pattern shearing interferometry using diffraction gratings," Optics Communication **126,** 191–196 (1996).

[60] A. Grundlach, J. M. Huntley, B. Manzke, and J. Schwider, "Speckle shearing interferometry using a diffractive optical beamsplitter," Opt. Eng. **36,** 1488–1493 (1997).

[61] C. Joenathan and L. Bürkle, "Electronic speckle pattern shearing interferometer using holographic gratings," Opt. Eng. **36,** 2473–2477 (1997).

[62] H. T. Yura and S. G. Hanson, "Optical beam wave propagation through complex optical systems," J. Opt. Soc. Am. A **4,** 1931–1948 (1987).

[63] H. Z. Cummins, N. Knable, and Y. Yeh, "Observation of diffusion broadening of Rayleigh scattered light," Physical Review Letters **12,** 150–153 (1964).

[64] J. J. W. Foreman, E. W. George, and R. D. Lewis, "Measurement of localized flow velocities in gases with a laser Doppler flowmeter," Appl. Phys. Letters **7,** 77–78 (1965).

[65] Y. Yeh and H. Z. Cummins, "Localized fluid measurements with and HeNe laser spectrometer," Applied Physics Letters **4,** 176–178 (1964).

[66] H. D. V. Stein and H. J. Pfeifer, "A Doppler Difference Method for Velocity Measurements," Metrologia **5,** 59–61 (1969).

[67] L. E. Drain, *The Laser Doppler Technique* (John Wiley and Sons, New York, 1981).

[68] F. Durst, A. Melling, and J. H. Whitelaw, *Principles and Practice of Laser Doppler Anemometry* (Academic Press, New York, 1980).

[69] L. H. Tanner, "A particle timing laser velocity meter," Opt. Laser Technol. pp. 108–10 (1973).

[70] J. C. S. Lai and Y. He, "Error considerations for turbulence measuements using laser-two-focus velocimetry," J. Phys. E: Sci. Instrum. **22,** 108–14 (1989).

[71] H. T. Yura, S. G. Hanson, and L. Lading, "Comparison between the laser time-of-flight velocimeter and the laser Doppler velocimeter for measurements on solid surfaces," In *OVmetry Conf.*, M. Pluta and J. K. Jabczynski, eds.,**SPIE Proceedings Series Vol. 2729,** 91–102 (Warzaw, 1996).

[72] C. J. Oliver, "Accuracy in laser anemometry," J. Phys. D: Appl. Phys **13,** 1145–59 (1980).

[73] S. G. Hanson, "Broadening of the Measured Frequency Spectrum in a Differential Laser Anemometer due to Interference Plane Gradients," J. Phys. D **6,** 164–171 (1973).

[74] P. C. Miles, "Geometry of the fringe field formed in the intersection of two gaussian beams," Applied Optics **23,** 5887–5895 (1996).

[75] M. Azzazy, R. L. Potts, L. Zhou, and B. Rosow, "Flow-velocity measurements with a laser diode array," Applied Optics **36,** 2721–2729 (1997).

[76] V. Strunck and D. Dopheide, "Velocimetry with phased arrays diode lasers," In *Proc. 3rd Int. Conf. on Laser Anemometry*, pp. 297–307 (Berlin, 1990).

[77] M. L. Jakobsen, S. Osten, S. R. Kitchen, C. Dam-Hansen, and S. G. Hanson, "Multiple-beam time-of-flight sensor based on a vertical cavity surface emitting laser diode array," Meas. Sci. Technol. **14,** 329–35 (2003).

[78] S. R. Kitchen, C. Dam-Hansen, and M. L. Jakobsen, "Diffractive beam splitter for wavelength compensation of laser Doppler anemotry systems,", pending US Patent 60/393,585, 2002.

[79] S. R. Kitchen, C. Dam-Hansen, and M. L. Jakobsen, "Diffractive beam splitter for wavelength compensation of laser Doppler anemometry systems,", Submitted to Applied Optics, November 2002, 2003.

[80] C. Dam-Hansen, "Temperature compensated optical system based on a diffractive optical element,", pending US Patent 60/393,584, 2002.

[81] C. Dam-Hansen and S. R. Kitchen, "Diffractive Laser Time-of-Flight Flow Sensor,", In preparation, 2003.

[82] J. Czarske, "A miniaturized dual-fibre laser Doppler Sensor," Measurement Science & Technology **12,** 1191–1198 (2001).

[83] S. Damp, "Battery-driven miniature LDA-system with semiconductor laser diode," in *Selected Papers from the Fourth Intl. Symp. on Appl. Of Laser-doppler Anemometry to Fluid Mechanics*, R. J. Adrian, D. F. G. Durão, F. Durst, T. Asanuma, and J. H. Whitelaw, eds., (Springer-Verlag, 1989).

[84] F. Quercioli, A. Mannoni, and B. Tiribilli, "Laser Doppler velocimetry with a compact disc pickup," Applied Optics **37,** 5932–5937 (1998).

[85] S. Bopp, F. Durst, R. Müller, A. Naqwi, C. Tropea, and H. Weber, "Small Laser-Doppler Anemometers Using Semiconductor Lasers and Avalanche Photodiodes," in *Applications of Laser Anemometry to Fluid Mechanics*, R. J. Adrian, T. Asanuma, D. F. G. Durão, F. Durst, and J. H. Whitelaw, eds., (Springer-Verlag, 1988), pp. 315–360.

[86] S. L. Kaufmann, F. D. Dorman, D. C. Bjorkquist, and M. R. Finn, "Laser Optical Measuring Device and Method for Stabilising Fringe Pattern Spacing,", US Patent 4,948,257, 1990.

[87] J. Schmidt, R. Völkel, W. Stork, J. T. Sheridan, J. Schwider, N. Streibl, and F. Durst, "Diffractive beam splitter for laser Doppler velocimetry," Optics Letters **17,** 1240–1242 (1992).

[88] R. Schodl and W. Förster, "A New Multi Colour Laser Two Focus Velocimeter for 3-Dimensional Flow Analysis," In *Int. Cong. on Instrumentation in Aerospace Simulation Facilities*, pp. 142–151 (Göthingen, 1989).

[89] S. M. Ross, *Introduction to probability and statistics for engineers and scientists* (John Wiley & Sons, New York, 1987).

[90] M. S. Beck and A. Pląskowski, *Cross Correlation Flowmeters - their Design and Application* (Adam Hilger, Bristol, 1986).

[91] L. Lading and R. V. Edwards, "Laser Velocimeters: lower limits to uncertainty," Applied Optics **32,** 3855–3866 (1993).

[92] R. L. Daugherty and J. B. Franzini, *Fluid Mechanics with Engineering Applications*, 6th ed. (McGraw-Hill, New York, 1965).

[93] H. Tennekes and J. L. Lumley, *A First Course in Turbulence* (MIT Press, Cambridge, MA, 1989).

A

Temperature Dependence of Laser Diodes

The laser used for the laser time-of-flight sensor described in Sec. 4.2 is a high power AlGaAs laser diode, ML64114R from Mitsubishi, which provides a stable, single transverse mode oscillation with a typical emission wavelength of 785 nm and continuous light output of approx. 50 mW.

Since the emission wavelength is strongly dependent on the temperature and also on the operating current, a characterisation of this dependence have been made in order to locate a stable working condition.

The operating current is set to 124.0 mA to obtain an output power of 50 mW. The laser diode is installed in a thermo-electric cooled mount so the temperature of the laser diode can be controlled within 0.01 K. The emission spectrum is measured using an Instaspec spectrometer with a HeNe laser at 632.8 nm as reference and with a wavestar spectrometer. Figure A.1 shows the measured emission spectrum for the laser diode. It is seen that the laser diode has a peak wavelength at 785.0 nm and a FWHM value of 0.5 nm.

In Fig. 2 the measured peak emission wavelength is shown as a function of the temperature. The arrows indicate the sequence of one measurement series (open squares), while another measurement has been performed (solid squares) to check the reproducibility.

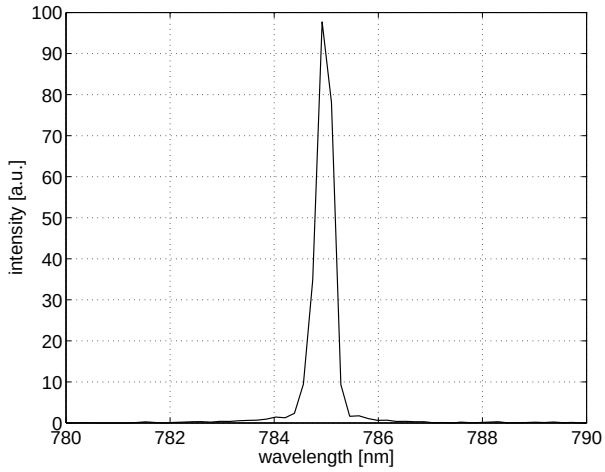

Figure A.1: Measured emission spectrum of ML64114R laser diode at 124.0 mA and 25.6 °C.

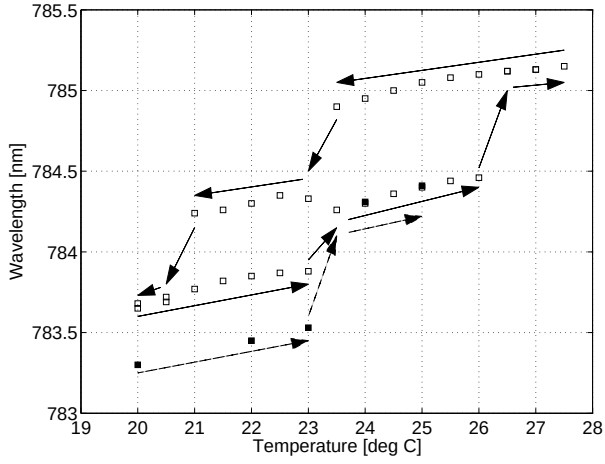

Figure A.2: Measured peak emission wavelength of a Mitsubishi ML64114R laser diode at 124.0 mA, as a function of the temperature.

A local linear temperature dependence of 0.06 nm/K is observed. However, the linear regions are separated by abrupt changes in the peak wavelength with a magnitude of 0.35-0.5 nm. This is due to mode hops, i.e. jumps from one longitudinal mode to a closely lying mode. Furthermore, a strong hysteresis effect is observed. At 25 °C, for example, the laser diode will have a peak wavelength of either 784.4 nm or 785.1 nm, dependent on the temperature history.

Similar curves have been measured for other samples of the same type of laser diode, with minor changes in the position of the modehops. The conclusion of this is that even if the laser diode is temperature stabilised, the wavelength will still be undefined within 1-3 logitudinal modes, i.e. approx. ± 0.5 nm. Therefore it is important to design the optical sensors to be independent of these wavelength changes.

Bibliographic Data Sheet **Risø-R-1381(EN)**

Title and author

Optical Sensors Based on Dedicated Diffractive Optical Elements
Steven Richard Kitchen

ISBN		ISSN
87-550-3154-4	87-550-3155-2 (Internet)	0106-2840

Department or group	Date
Optics and Fluid Dynamics Department	April 2003

Sponsorship

The work has been performed under the Industrial Research Education Ph.D. program (erhvervsforskeruddannelsen) and has been jointly financed by the Danish Academy of Technical Sciences (ATV), Kamstrup A/S and Bourdon-Haenni A/S.

Pages	Tables	Illustrations	References
132	4	79	93

Abstract (max. 2000 characters)

This thesis deals with the development of optical sensors based on laser diodes and dedicated diffractive optical elements. The thesis is divided into two parts. The first part of the thesis deals with development of interferometrically based displacement sensors intended for use in pressure transducers. For the purpose of probing the deflection of the diaphragm in a pressure transducer, a novel common-path interferometer has been developed. The central part of the common-path interferometer is a multi-functional holographic optical element (HOE) that handles function like beam splitting and focusing of the light. The HOE works as both transmitter and receiver in the common-path setup. This means that the stability is inherent in the HOE and the system is self-aligning, which makes the sensor very robust. There has also been devised a new technique to extend the unambiguous measurement range of differential displacements. This technique is based on probing three points on the object surface simultaneously and utilises the quadrature phase signals that are automatically provided by the specially designed HOE. During the project, there has also been developed a new tool for conceiving new types of common-path interferometers by placing a specially designed HOE in the Fourier plane of a 4-*f* setup. The surface structure for the Fourier filter can be calculated by Fourier transforming the desired impulse response function of the system. Thereby, the system can be designed to probe a specific type of surface displacement. The second part of the project deals with development of optical flow sensor systems. Firstly, a new beam splitter system based on two linear gratings has been devised. The beam splitter is intended for use in laser Doppler anemometry systems, where the fringe spacing in the measurement volume is directly proportional to the wavelength of the light source. This is compensated by the beam splitter system by letting the closing angle of the two probe beams be wavelength dependent. Secondly, a new laser time-of-flight sensor has been developed. The sensor is intended for in-situ calibration of other types of flow sensors, which are permanently installed in large flow installations. The system is designed so that the transmitter and receiver functions are implemented in a single HOE plane. This makes the LTV sensor self-aligning and robust. The multi-functional HOE is additionally designed so that the LTV sensor to a first degree is wavelength independent. All the diffractive structures are implemented as surface relief structures in photoresist. These structures have the advantage that they can be replicated using for instance injection moulding. Thereby one can mass-produce the structures at low cost, which makes it possible to manufacture a cheap optical sensor.

Descriptors

LASER DIODES; HOLOGRAPHY; GRATINGS; INTERFEROMETRY; ESPI; VELOCIMETRY; ANEMOMETRY; PRESSURE SENSING; FLOW SENSING